Earthquake Geology of the Large Left-lateral Strike-slip Fault System at the Pacific and Australian Plate Margin, Eastern Indonesia

Adi Patria

A Dissertation Submitted in Partial Fulfillment of the Requirements

for the Degree of Doctor of Science

Graduate School of Science and Engineering

Doshisha University

June 2022

Abstract

Eastern Indonesia is a seismically active and rapidly deforming region due to convergence between the Eurasian, Australian, Philippine Sea, and Pacific plates. The ~120 mm/yr westward motion of the Pacific plate relative to the Australian plate has resulted in a left-lateral slip of ~80 mm/yr in eastern Indonesia. This slip is accommodated by a large left-lateral strike-slip fault system, extending from Papua to Sulawesi. Several damaging earthquakes occurred on this fault system, such as the 2018 M_w 7.5 Palu earthquake (~2,200 fatalities) and the 1899 M_w 7.8 Seram earthquake (~3,800 casualties). However, the lack of geologic information on the fault system, such as precise fault traces, geologic slip rates, paleoseismic history, and recurrence intervals of large earthquakes, has been a significant barrier to understanding the active tectonics and seismic hazard of this fault system. Thus, this research aims to improve the active fault map, uncover the faulting and seismic behavior, and reveal the regional active tectonics by investigating the earthquake geology of active faults in this fault system, focusing on central Sulawesi and the northern Banda Arc.

The study of the Palu-Koro fault in the northwest Palu Valley, Sulawesi investigates the fault development based on tectonic geomorphic interpretations and field observations. The results show two normal faults and a strike-slip fault in the valley. A basin-bounding normal fault marks the topographic break between the mountain and valley. Another normal fault is observed east of the basin-bounding fault, cutting old alluvial fans. The strike-slip fault is located within the valley as an intra-basin fault, crossing the distal part of young alluvial fans, evidenced by intra-basin ridges in places. The surface rupture of the 2018 M_w 7.5 Palu earthquake in the valley shows a left-lateral displacement of up to 4 m. It is postulated that the development of the Palu-Koro fault in the Palu Valley is characterized by the migration of faulting activity from the basin-bounding fault to the intra-basin fault.

The Matano fault study on Sulawesi integrates tectonic geomorphic interpretations, electrical resistivity tomography (ERT) surveys, ground-penetrating radar (GPR) profiling, and

paleoseismic analysis to investigate the easternmost portion of the Matano fault. The easternmost Matano fault comprises five geometrical segments. Four segments predominantly show left-lateral motion, while one segment is a reverse fault related to a restraining fault bend. The easternmost Matano fault records three surface faulting events in the last millennium. The most-recent earthquake occurred between AD 1432–1819 with an estimated M_w of ~7.4 and a probable rupture length of 107 km. The average recurrence interval of the surface-rupturing earthquake is calculated at 190–270 years, and the slip rate is estimated at ~30 mm/yr. Since the last surface faulting event, at least 200 years have passed, exceeding the shortest average recurrence interval. Thus, the next large earthquake on this fault should be anticipated. The easternmost Matano fault likely continues offshore to the South Sula fault in addition to the Tolo thrust.

The study in the northern Banda Arc yields a detailed active fault map for the onshore region based on tectonic geomorphic interpretations. In north Seram, geomorphic features such as uplifted marine terraces, fault scarps, and wind gaps represent active thrust faulting. The Kawa and Bobot faults are left-lateral strike-slip faults in Seram, characterized by fault scarps, linear valleys, offset rivers, and shutter ridges. Numerous active faults cut uplifted marine terraces in Amahai, Ambon, and surrounding islands. Some active faults bound intramountain depressions in central Buru. Further investigation of the Ambon fault based on drone mapping and GPR surveys reveals that the 40-km-long Ambon fault is a normal fault and deforms fluvial terraces. The calculation of potential seismic hazards shows that the active faults in the region can produce $M_w \geq 6.4$ earthquakes. The Kawa fault could generate an M_w 7.6 earthquake. The Ambon fault poses a significant seismic hazard because it is located near populous areas such as Ambon City. The strike-slip faults in Seram and other offshore strike-slip faults accommodate 29–45 mm/yr left-lateral slip in eastern Indonesia, while the Ambon fault may absorb a portion of ~16 mm/yr extension in the Banda Sea.

Acknowledgments

I would like to express my sincere gratitude to my supervisor, Prof. Hiroyuki Tsutsumi, who gave me an opportunity to study at Doshisha University. I thank him for the support, supervision, and advice throughout my study which enabled me to finish my doctoral work. Under his supervision, I was able to broaden my knowledge and skills in active fault studies.

I would also like to thank Prof. Danny Hilman Natawidjaja for inviting me to join the '*Building Earthquake and Tsunami Resilience in East Indonesia'* project, funded by the Royal Society, UK. This research project allowed me to conduct fieldwork in eastern Indonesia. His supervision and advice about the active tectonics of eastern Indonesia are greatly appreciated.

I thank colleagues from Research Center for Geological Disaster, Indonesian Research and Innovation Agency (BRIN), Purna S. Putra, Mudrik R. Daryono, Muhammad Hanif, Anggraini R. Puji for field assistance, data and sample handling, and discussion. I also thank field technicians, Amar, Nyanjang, Nandang Supriatna, Sutarman, and Bambang W. Suwargadi, for their assistance during the Ambon and Matano fault surveys. I acknowledge PT. Aquila Solution and PT. Vale Indonesia for kindly providing the LiDAR data used for the Matano fault study. I also thank Erfin Elly, Rizwan, Axel (Pattimura University), and M. Zain Tuakia (Research Center for Deep Sea, BRIN) for support and field assistance during the Ambon fieldwork. I am grateful to Haruo Kimura for teaching me the GPR method.

I thank Doshisha University for providing facilities, literature access, and student support. I am funded by the MEXT Scholarship from the Japanese Government for my doctoral study at Doshisha University. I also thank BRIN for allowing me to undertake the doctoral course. I also thank the former laboratory secretary Yuki Doi for helping me solve daily life matters in Japan.

I am grateful for the support of my parents, sister, and extended relatives. Special thanks go to my wife and daughters for their support, love, and warmth during the last three years. My family has greatly motivated and supported me in finishing my doctoral study. Lastly, I thank friends who shared and contributed to my journey in Japan.

Table of contents

List of figures

List of tables

Chapter 1

Introduction

1.1 Background

Earthquakes are one of the most damaging hazards for human civilizations. Records have shown the impact of earthquakes on society in the world. The deadliest instrumentally recorded earthquake was the 2010 M_w 7 Haiti earthquake with more than 300,000 casualties (DesRoches et al., 2011). Earthquakes are a form of energy, released by the rapid movement along active faults (Scholz, 2019). A fault is a discontinuity separating two blocks in the earth's crust, and it is defined as active if it slips during the late Quaternary (e.g., Sieh and Natawidjaja, 2000; Tsutsumi and Perez, 2013; Yeats et al., 1997). Besides ground shaking and surface ruptures, earthquakes may also trigger other associated hazards such as tsunamis and landslides. Active fault motions are controlled by the dynamics of plate tectonics. Active faults are densely distributed in the tectonic plate margins. Some countries or regions are situated at the plate boundaries, such as Japan, Taiwan, Indonesia, the Philippines, New Zealand, the Himalayas, the Caribbean, and the western coast of the American continent.

Indonesia is one of the most seismically active regions in the world (Hutchings and Mooney, 2021; McCaffrey, 1988). It is located at the convergence zone between the Australian, Eurasian, Philippine Sea, and Pacific plates (Figure 1.1) (Hamilton, 1979). Tectonically, Indonesia can be divided into two areas: western and eastern Indonesia, separated by the Makassar Strait. Western Indonesia is characterized by normal and oblique convergences between the Eurasian and Australian plates at a rate of ~70 mm/yr (DeMets et al., 2010; Malod et al., 1995; Schlüter et al., 2002). The normal convergence is accommodated by the Java subduction zone and some active faults in Java (e.g., Daryono et al., 2019; Kopp et al., 2001; Marliyani et al., 2016; Shulgin et al., 2011). The oblique convergence is partitioned into the Sumatra subduction zone and the arc-parallel strike-slip Sumatran fault (e.g., Katili, 1970; McCaffrey, 2009; Sieh and Natawidjaja, 2000).

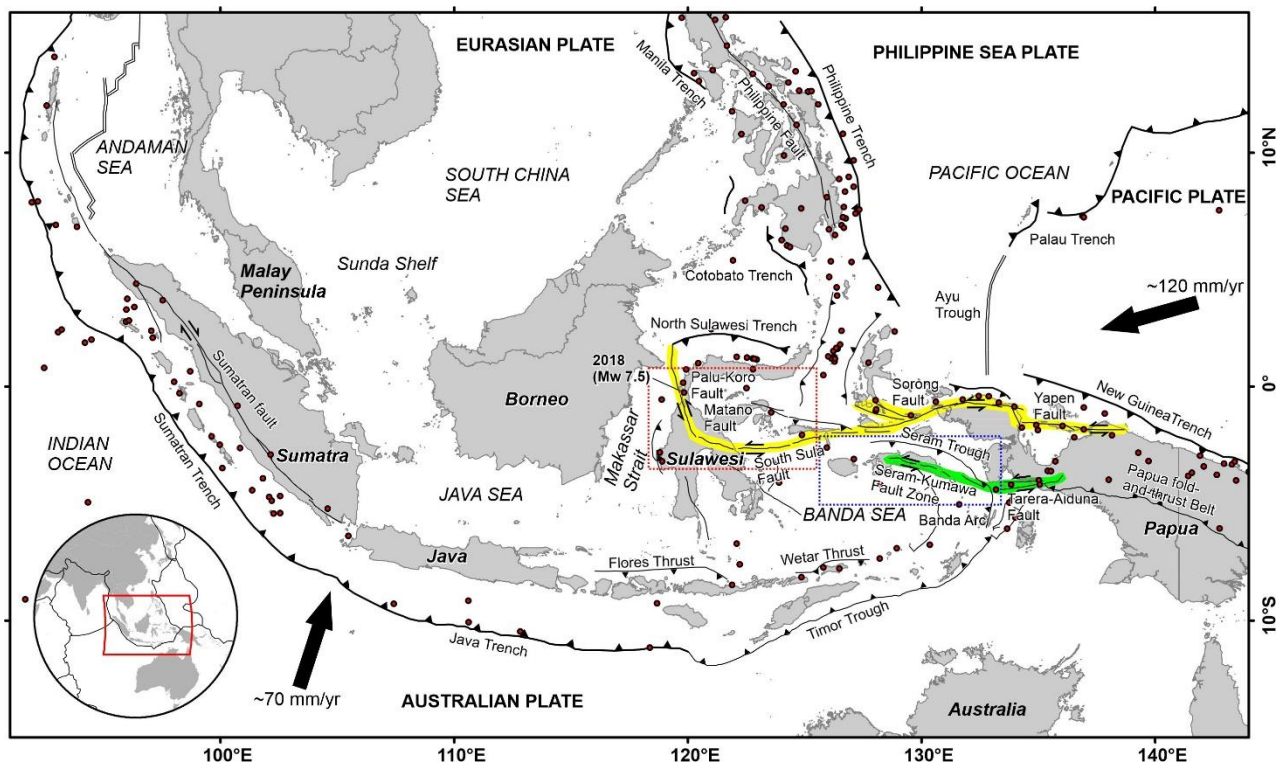

Figure 1.1 Tectonic setting and seismicity of Indonesia. Major structures are compiled from Hall (2012), Pownall et al. (2016), and Titu-Eki and Hall (2020). Plate motion vectors are from DeMets et al. (2010). $M_w \geq 7$ earthquake hypocenters with a depth ≤40 km during 1910–2022 are from the USGS earthquake catalog (dots). The left-lateral strike-slip fault system in eastern Indonesia can be divided into the northern (yellow highlighted) and southern parts (green highlighted). The dotted rectangles indicate the study areas: central Sulawesi (red) and the northern Banda Arc (blue).

Unlike western Indonesia, eastern Indonesia is located in a complex tectonic setting where the convergence involves the Australian, Eurasian, Philippine Sea, and Pacific plates as well as a number of microplates (e.g., Charlton, 2000; Hall, 2012; Hamilton, 1979; Hinschberger et al., 2005). In addition to the convergence between the Australian and Eurasian plates, the Pacific plate rapidly moves westward at a rate of ~120 mm/yr relative to the Australian plate (DeMets et al., 2010). This rapid motion has resulted in ~80 mm/yr left-lateral slip across the northern portion of eastern Indonesia (Stevens et al., 2002). This slip is accommodated by a large fast-slipping left-lateral strike-slip fault system (e.g., Bock et al., 2003; Silver et al., 1983; Socquet et al., 2006; Stevens et al., 1999; Watkinson and Hall, 2017). The fault system can be divided into two portions (Figure 1.1). The northern part includes the Yapen, Sorong, South Sula (also known as Sula-

Sorong), Matano, and Palu-Koro faults, while the southern part consists of the Tareira-Aiduna fault and the Seram-Kumawa fault zone (the Kawa, Bobot and several offshore faults).

There have been many large ($M_w \geq 7$) strike-slip earthquakes that occurred along this fault system (Figure 1.1). However, despite its fast motion and intense seismicity, only a few studies have been done to investigate the earthquake geology of this fault system (e.g., Bellier et al., 2001; Daryono and Natawidjaja, 2019; Natawidjaja et al., 2021). Early geodetic studies have resolved the short-term slip rate of the fault system (e.g., Bock et al., 2003; Socquet et al., 2006; Stevens et al., 2002). The published active fault map by National Center of Earthquake Study (PUSGEN) (2017) has provided basic information such as the general location of active faults and potential seismic magnitudes, but it lacks detailed geological information. Watkinson and Hall (2017) attempted to document Quaternary faults in eastern Indonesia, but evidence of active faulting is also lacking. So far, only two paleoseismic studies have been done in eastern Indonesia and only on the Palu-Koro fault (i.e., Bellier et al., 1998; Daryono and Natawidjaja, 2019).

Although information from several previous works is helpful to some extent, it is not sufficient to uncover the faulting and seismic behavior of the large left-lateral strike-slip fault system in eastern Indonesia. The lack of detailed geological information, such as precise fault traces, slip rates, paleoseismic history, and recurrence intervals of large earthquakes, has been a significant barrier to the seismic hazard evaluation in eastern Indonesia, where ~40 million people live. These data are required for understanding the seismic hazard posed by the fault system. Recently, the M_w 7.5 2018 Palu earthquake ruptured along the Palu-Koro fault in Sulawesi and caused a tsunami (e.g., Jaya et al., 2019; Natawidjaja et al., 2021; Putra et al., 2019). The National Disaster Management Agency of Indonesia (BNPB) reported ~2,200 fatalities, ~68,000 houses collapsed, and ~900 million USD economic loss. This event has reminded potential seismic hazards of the fault system and the necessity of detailed geological studies on the fault system. Thus, the research in this dissertation intends to uncover the earthquake geology of the active faults along the fault system. This research has important implications for seismic hazard assessment in

eastern Indonesia and improves quantitative understanding of the active tectonics of the Australian and Pacific plate margin.

1.2 Research aims and study areas

The overall purpose of this dissertation is to (1) provide precise active fault map, (2) uncover the faulting behavior, such as slip rate, large-earthquake recurrence interval, and potential moment magnitude (M_w), (3) evaluate the seismic hazard, and (4) clarify the active tectonics of the large left-lateral strike-slip fault system in eastern Indonesia. In this research, I selected central Sulawesi and the northern Banda Arc to study the northern and southern parts of the left-lateral strike-slip fault system, respectively (Figure 1.1). The northwest Palu valley was selected because it records multiple stages of faulting, including the 2018 M_w 7.5 earthquake's surface ruptures. The easternmost portion of the Matano fault (later called "the easternmost Matano fault") was chosen for a comprehensive investigation because it was suitable for paleoseismic excavation and has not ruptured at least in the last two centuries. The northern Banda Arc region was selected because active faults in the region are poorly studied. A further detailed investigation was done in Ambon for the Ambon fault because it possesses a significant risk to a populous area, Ambon City.

Since this research consists of multiple locations, three research outcomes are presented in this dissertation with the following objectives:

1. to map the tectonic geomorphic features of the Palu-Koro fault, Sulawesi including the surface rupture of the 2018 M_w 7.5 Palu earthquake in the northwest Palu Valley and interpret the Quaternary evolution of the Palu-Koro fault within the valley.
2. to precisely map the surface traces, examine the shallow subsurface structures, reveal the paleoseismic history, establish the probable magnitude and extent of the last surface faulting event, calculate slip rate and large earthquake recurrence interval, assess the seismic hazard, and clarify the active tectonics' significance of the eastern Matano fault.
3. to interpret tectonic geomorphology and map the active faults in the northern Banda Arc, document tectonic landforms and shallow-subsurface structures of the Ambon fault, estimate

the potential seismic hazards associated with each active fault, and explain the active tectonics' implication of the active faults in the northern Banda Arc.

1.3 Dissertation outline

This dissertation is divided into eight chapters that are briefly explained below.

- **Chapter 1** introduces the background, research aims, and study areas of my research in eastern Indonesia, and describes the dissertation outline.
- **Chapter 2** summarizes the current understanding of regional tectonics, which includes the plate tectonic development, plate tectonic motions, and seismicity of eastern Indonesia.
- **Chapter 3** describes the methodology of this research, including data collection, processing, and interpretations.
- **Chapter 4** presents the results of the tectonic geomorphic investigation and field observation including the surface rupture of the 2018 M_w 7.5 earthquake on the Palu-Koro fault, Sulawesi in Palu Valley, and provides an insight into the faulting migration of the Palu-Koro fault. Purna Sulastya Putra (BRIN) helped for the field data collection of this work. This chapter has been published as *Patria, A., Putra, P.S., 2020. Development of the Palu–Koro Fault in NW Palu Valley, Indonesia. Geoscience Letters, 7, 1,1-11.*
- **Chapter 5** shows the results of the tectonic geomorphology, shallow-subsurface geophysics, and paleoseismology analyses on the easternmost Matano fault, Sulawesi. This study provides detailed active fault traces, documents multiple surface-rupturing earthquakes for the past 1300 years, estimates an average recurrence interval of surface-rupturing earthquakes, and a slip rate, and clarifies the eastern continuation of the Matano fault. I collaborated with Prof. Danny H. Natawidjaja, Mudrik R. Daryono, Muhammad Hanif, Anggraini R. Puji (BRIN), and Prof. Hiroyuki Tsutsumi (Doshisha University).
- **Chapter 6** presents the results of the active fault mapping and seismicity analysis in the northern Banda Arc. This chapter also presents the results of the detailed tectonic geomorphic investigation and ground-penetration radar profiling on the Ambon fault. The results of this

study provide information on potential seismic hazards and the active tectonics significance of active faults in the northern Banda Arc. The work of this chapter was done in collaboration with Muhammad Hanif, Prof. Danny H. Natawidjaja (BRIN), and Prof. Hiroyuki Tsutsumi (Doshisha University). A portion of this study has been published as *Patria, A., Tsutsumi, H., Natawidjaja, D.H., 2021. Active fault mapping in the onshore northern Banda Arc, Indonesia: Implications for active tectonics and seismic potential. Journal of Asian Earth Sciences, 218, 104881.*

- **Chapter 7** discusses the broader implications of the results for the seismic hazard and active tectonics of the left-lateral strike-slip fault system in eastern Indonesia.
- **Chapter 8** concludes the main findings in this dissertation.

Chapter 2

Regional tectonics

2.1 Plate tectonic development

Eastern Indonesia records a complex history of subduction, obduction, collision, and extension (e.g., Charlton, 2000; Hall, 2012; Hamilton, 1979; Katili, 1991). Hall (2012) reconstructed the plate tectonic motion of Indonesia and the surrounding region (Figure 2.1). The development of eastern Indonesia began in the late Jurassic when the northern Gondwana was rifted. It was followed by an oceanic spreading, forming a new Jurassic oceanic crust at the Banda embayment north of Australia (Spakman and Hall, 2010). The subduction of the Australian plate beneath the Eurasian and Pacific plates started in the Paleocene as the Australian plate moved northward. Figure 2.1 summarizes the plate tectonic reconstruction of the eastern Indonesia region in the last 25 Ma (*mega annum*, million years ago). In the late Oligocene, the oceanic Australian plate subducted beneath the Philippine Sea plate, and the Sula Spur began to collide with the north Sulawesi volcanic arc, marking the initial collision between the Australian and Eurasian plates (Hall, 2012).

In the middle Miocene, the collision later caused the clockwise rotation of the Philippine Sea plate and led to the formation of a strike-slip fault along northern Papua (Hall, 2012; Hall et al., 1995). The double subduction of the Molucca Sea plate beneath the north Sulawesi volcanic arc and Halmahera had begun at this time. The transform fault along northern New Guinea was connected to both double subduction trenches. The Java subduction zone started to roll back into the Banda Embayment and began invading the old-and-cold Jurassic oceanic crust (Hall, 2012; Spakman and Hall, 2010).

In the late Miocene, the subduction rollback caused the eastward migration of the Java subduction trench and promoted the extensions in Sulawesi and the Sula Spur (Hall, 2012). The oceanic spreading of the north Banda basin occurred during 12–7 Ma (Hinschberger et al., 2005) and plausibly due to the subduction rollback.

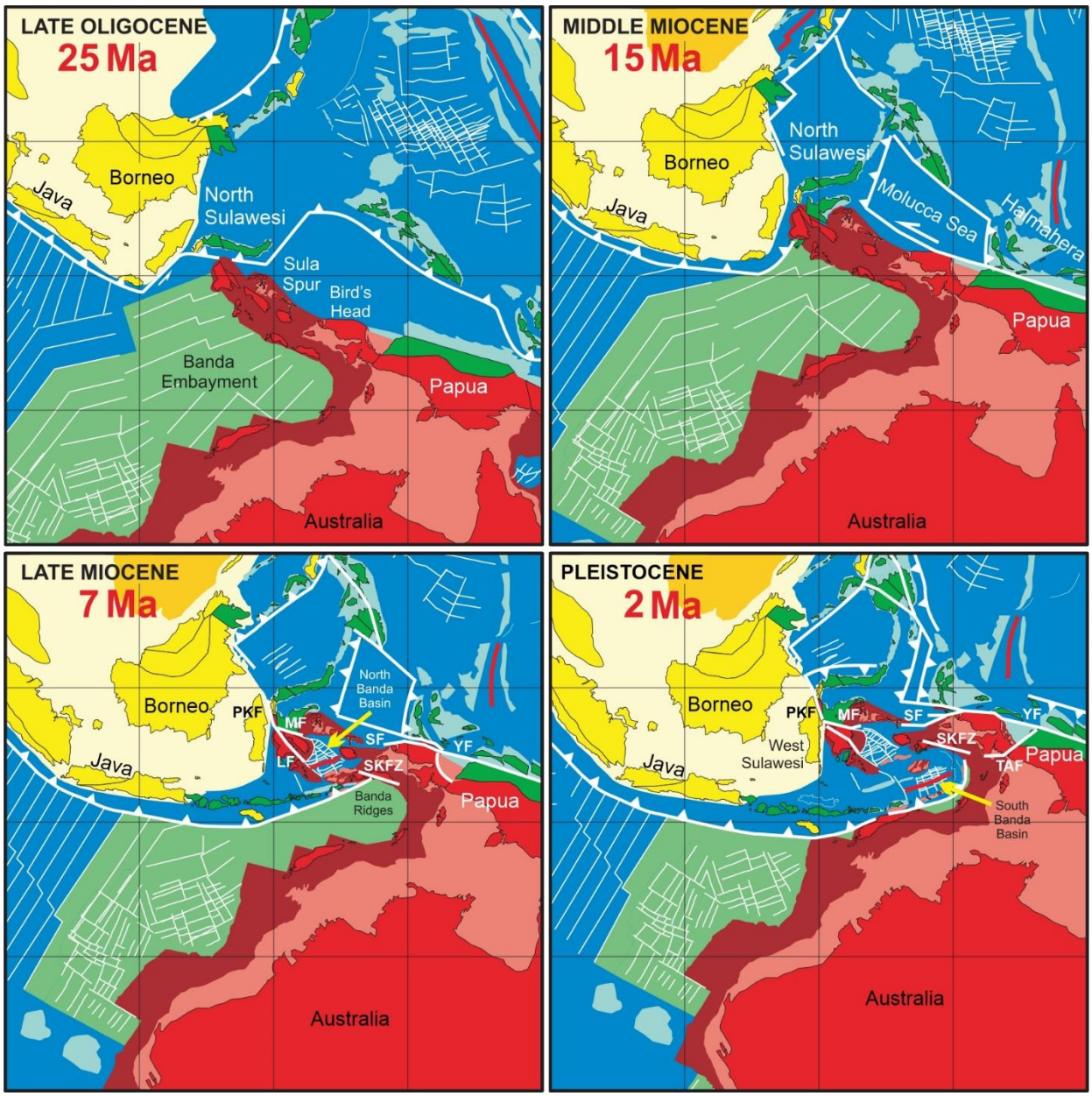

Figure 2.1 Plate tectonic evolution model of eastern Indonesia from the late Oligocene to late Pliocene (modified after Hall, 2012 with additional results from Hall et al., 2017 and Pownall et al., 2017). YF: Yapen fault, SF: Sorong fault, MF: Matano fault, LF: Lawanopo fault; TAF: Tarera-Aiduna fault, SKFZ: Seram-Kumawa fault zone. Green-colored regions are mainly arc, ophiolitic, and accreted material formed at plate margins. Areas with blue color are the submarine arc region, hotspot volcanic products, and oceanic crust. The Eurasian and Australian continents are colored in shades of yellow and red, respectively. The light green area in the Banda Embayment marks the Jurassic oceanic crust.

The South Sula fault developed after the opening of the Banda Basin (Titu-Eki and Hall, 2020). The transform fault in northern New Guinea splayed, forming the Sorong fault in Bird's Head of Papua (Charlton, 2000; Hall, 2012; Hamilton, 1979). The Sula Spur was separated from

the Australian continent and translated westward along the Sorong fault (Hall, 2012; Hinschberger et al., 2005). The collision between the Sula Spur and the east arm of Sulawesi had reactivated the Matano, Lawanopo, and Palu-Koro faults in Sulawesi (Bellier et al., 2006; Silver et al., 1983; Villeneuve et al., 2002). In Seram, the Seram-Kumawa fault zone had been reactivated and limited the migration of the Java subduction trench (Hall et al., 2017; Pownall et al., 2017).

The subduction rollback continued and caused the formation of oceanic crust in the south Banda basin in the Pliocene (Hall, 2012). The double subduction in the Molucca Sea was almost finished and both volcanic arcs were about to collide (Hall et al., 1995). The old-and-cold Jurassic oceanic crust in Banda Embayment had been almost totally invaded by the late Pliocene. The Tarera-Aiduna fault also developed in the Bird's Neck of Papua (Hamilton, 1979; Katili, 1989). The activity of the Lawanopo fault was terminated before the Pleistocene (Natawidjaja and Daryono, 2015), and other strike-slip faults remain active until the present.

2.2 Plate tectonic motions

Plate tectonic motions in eastern Indonesia are controlled by the convergence between four major plates: Eurasian, Australian, Philippine Sea, and Pacific plates. The northward movement of the Australian plate relative to the Eurasian at a rate of ~70 mm/yr is accommodated by convergence across the Timor Trough. In contrast, the Pacific plate rapidly slips westward at a rate of ~120 mm/yr relative to the Australian plate (Figure 2.2) (DeMets et al., 2010). This rapid westward motion of the Pacific plate has resulted in a left-lateral slip of ~80 mm/year across the northern portion of eastern Indonesia (Stevens et al., 2002). This slip is accommodated by the left-lateral strike-slip fault system in eastern Indonesia (Bock et al., 2003; Watkinson and Hall, 2017).

Based on geodetic measurements, the Yapen fault in Papua slips left-laterally at a high rate, 46 ± 12 mm/year (Bock et al., 2003; Stevens et al., 2002). In Bird's Head of Papua, the velocity fields do not show significant movement along the Sorong fault (Puntodewo et al., 1994; Stevens et al., 2002), only a slight residual left-lateral motion (Bock et al., 2003). The GPS stations along the Sorong fault in Bird's Head of Papua are located close to the fault line so the slip rate could

not be resolved using these stations. However, a recalculation in section 6.5 using the available velocity field data yields a rate of about 20–25 mm/yr across the Sorong fault. Further west, one or more strands of the Sorong fault between Obi and Halmahera accommodate 19 ± 8 mm/yr left-lateral slip (Bock et al., 2003). There is also a significant left-lateral motion between Obi and Ambon (Bock et al., 2003), likely accommodated by the Sorong fault just south of Obi. This left-lateral motion is transferred to the South Sula fault to the west (Socquet et al., 2006).

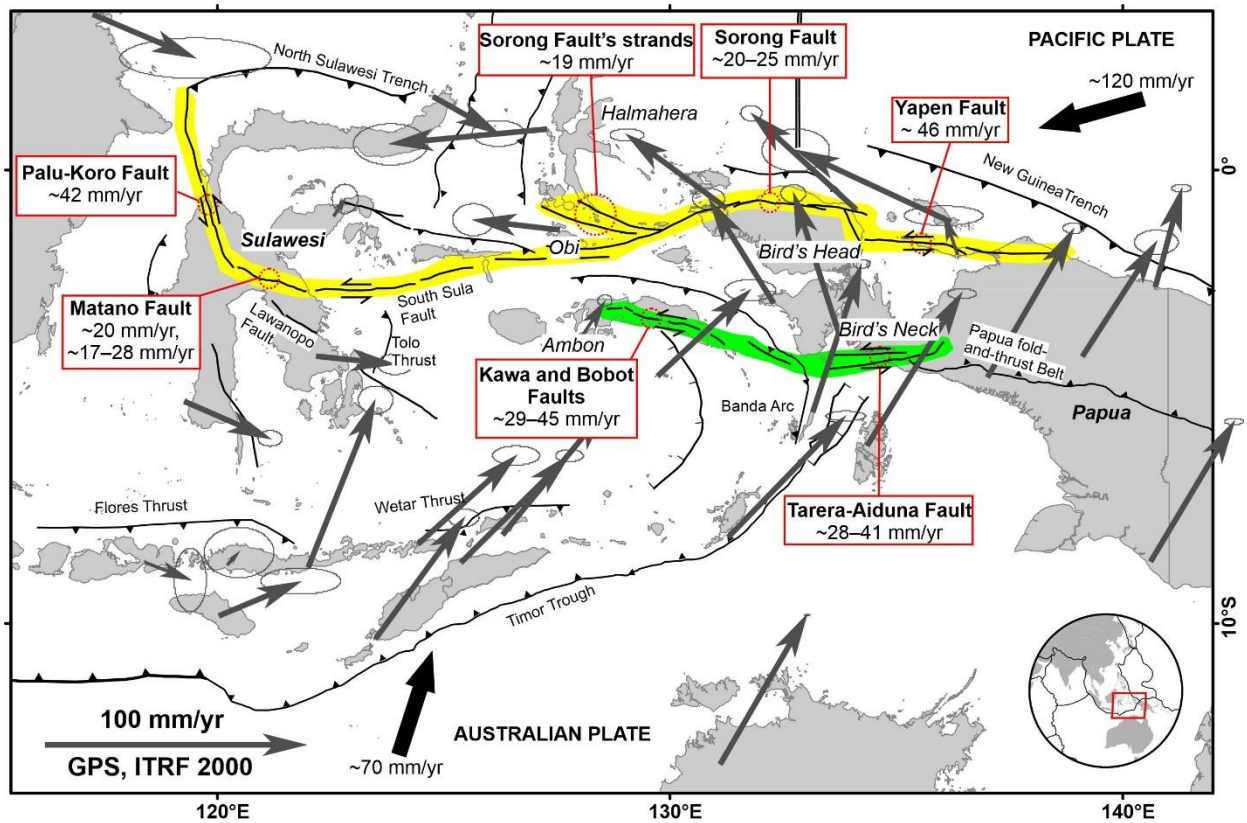

Figure 2.2 Geodetic velocity fields (thin arrows) derived from Global Positioning System (GPS) surveys from 1991 to 2001, with reference of International Terrestrial Reference Frame (ITRF) 2000 (Bock et al., 2003). Plate motion vectors (thick arrows) are from DeMets et al. (2010). Major tectonic features are compiled from various sources described in Figure 1.1.

In Sulawesi, most geodetic studies focused on the Palu-Koro fault. The Palu-Koro fault terminates at the western tip of the North Sulawesi subduction trench (Hall and Wilson, 2000; Hamilton, 1979; Rangin et al., 1999). The convergence rate at the subduction zone increases westward from 20 to 54 mm/year, causing a clockwise rotation of the north arm about a pole located at the northeastern Sulawesi (Beaudouin et al., 2003; Rangin et al., 1999; Stevens et al.,

1999). Walpersdorf et al. (1998b) concluded a left-lateral slip rate of 34 mm/yr. They also recorded an increase in the slip rate from 26 mm/yr to 63 mm/yr after two $M_w \geq 7$ subduction earthquakes in 1996 in north Sulawesi. Socquet et al. (2006) obtained a slip rate of 42 mm/yr for the Palu-Koro fault and suggested that the slip is partitioned into the Matano and Lawanopo fault. Bellier et al. (2001) estimated that the Holocene slip rate of the Palu-Koro fault is 35 ± 8 mm/yr based on cumulative stream offset and age of alluvial fan from ^{10}Be cosmogenic dating. However, since the Lawanopo fault is interpreted to be inactive (Natawidjaja and Daryono, 2015), the motion should be translated mainly to the Matano fault. Based on geodetic modeling, Walpersdorf et al. (1998a) argued that the Matano fault moves slower than the Palu-Koro fault, at ~20 mm/yr. A recent GPS study by Khairi et al. (2020) also suggested that the Matano fault slips at 17–28 mm/yr. The Palu-Koro and Matano faults act as transfer faults connecting the Tolo thrust and North Sulawesi Subduction (Silver et al., 1983).

Some portion of the left-lateral slip in eastern Indonesia is accommodated by the Papua fold-and-thrust Belt because there is ~21 mm/yr of left-lateral slip across the belt (Bock et al., 2003). This is in agreement with strike-slip fault earthquakes identified by Abers and McCaffrey (1988). In Bird's Neck of Papua, the Tarera-Aiduna fault also accommodate the Pacific plate's motion relative to the Australian plate. The fault slips left laterally at 28–41 mm/yr. Analysis in section 6.5 based on published geodetic data suggests that the left-lateral slip is translated further west to the Kawa and Bobot faults at 29–45 mm/yr.

2.3 Seismicity

Eastern Indonesia has experienced many large ($M_w \geq 7$) earthquakes (Figure 2.3). Based on the historical and significant earthquake catalog from National Geophysical Data Center (NGDC) (2022), the oldest recorded earthquake occurred in the 17th century in eastern Indonesia. This catalog also indicates that the earliest documented seismic event in Sulawesi was in the 19th century. Many instrumentally-recorded earthquakes are attributed to the left-lateral strike-slip fault system (Figure 2.3). In this section, several significant earthquakes on the fault system are described.

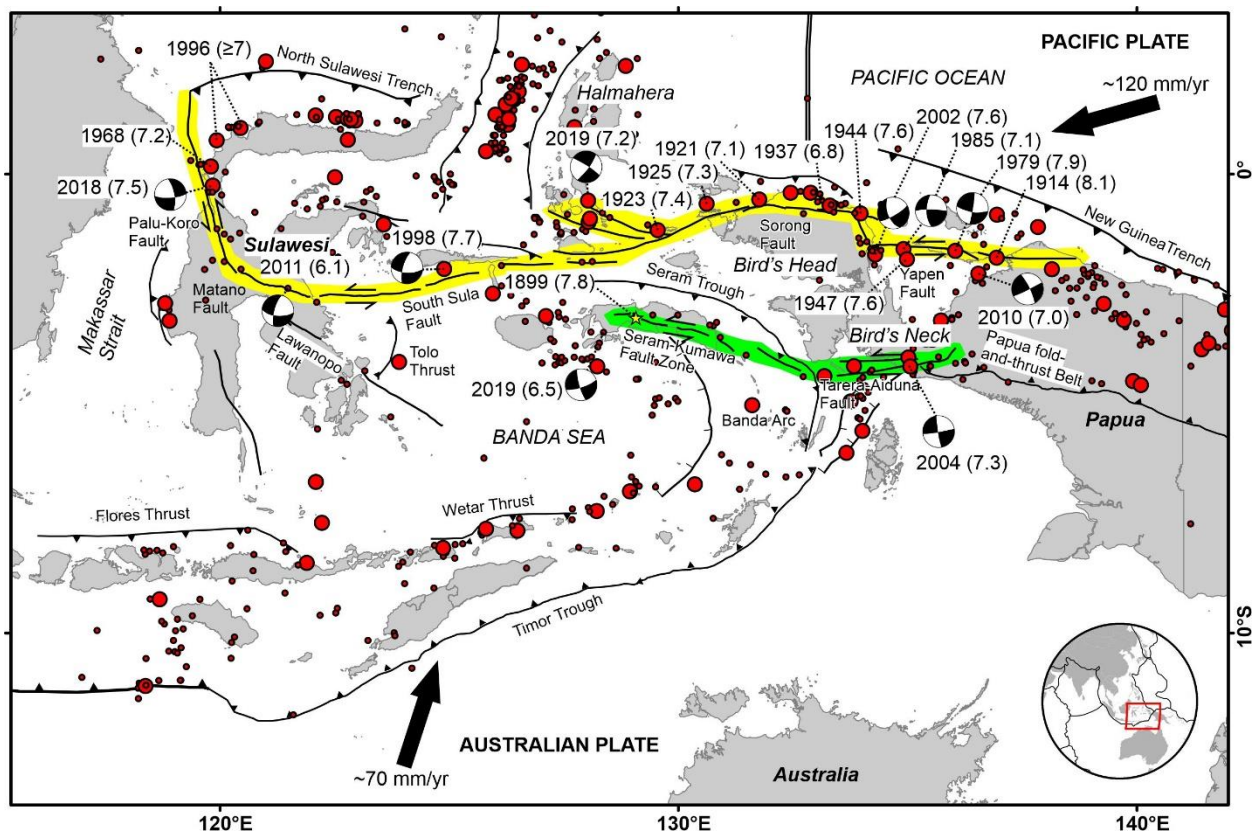

Figure 2.3 Modern significant (M_w ≥6) seismicity with a depth of ≤40 km during 1910–2022 in eastern Indonesia from the USGS earthquake catalog. Small dots mark earthquakes with M_w 6– 7, and large dots indicate M_w ≥7 earthquakes.

Several large earthquakes occurred between 1914 and 2010 along the Yapen fault (Figure 2.3). Most of the earthquakes show strike-slip motion on the east-trending nodal planes, concordant with the fault orientations. One of the notable earthquakes was the 1979 M_w 7.9 tsunamigenic earthquake which claimed more than 100 casualties (Okal, 1999). The earthquake might have ruptured offshore as there was no report about inland surface displacement. In contrast, the seismicity along the Sorong fault in Bird's Head of Papua is relatively low. Relocations of the 1937 and 1944 earthquakes suggested that those earthquakes were likely asserted to the Sorong fault in Bird's Head of Papua (Okal, 1999). West of Bird's Head of Papua, there were several large earthquakes along the Sorong fault in the 1920s which possibly ruptured the Sorong fault (Figure 2.3).

South of Sula, there was an M_w 7.7 earthquake in 1998 (Figure 2.3). The east-trending nodal plane of this earthquake indicates a left-lateral motion. This earthquake might have ruptured the

eastern portion of the South Sula fault (Vigny et al., 2002). Further west, the 2011 M_w 6.1 earthquake near Lake Matano was attributed to the Matano fault and caused considerable damage to the nearby area (Watkinson and Hall, 2017). The latest surface faulting event in eastern Indonesia was the 2018 M_w 7.5 Palu earthquake in Sulawesi, rupturing the Palu-Koro fault for 170 km (Natawidjaja et al., 2021). The surface rupture showed a left-lateral displacement concordant with the focal mechanism solution of this earthquake on the north-trending nodal plane. Daryono and Natawidjaja (2019) show that the 2018 earthquake re-ruptured at the location of the 1909 earthquake so the recurrence interval of the surface-rupturing earthquake for the Palu-Koro fault is roughly 110 years. In 1968, an M_w 7.2 earthquake occurred offshore near the hypocenter of the 2018 earthquake and might have ruptured the northern portion of the Palu-Koro fault (Prasetya et al., 2001).

Several large earthquakes were generated along the Tarera-Aiduna fault since 1928 (Figure 2.3). The most recent event was the 2004 M_w 7.3 earthquake which resulted in 32 fatalities and 213 injuries. The focal mechanism solution indicates a left-lateral motion along an east-trending plane, in agreement with the fault's strike. Further west, in the northern Banda Arc, large modern seismic event is absent. However, historical records show that several damaging earthquakes have impacted the region since the 17th century (National Geophysical Data Center (NGDC), 2022). The 1899 M_w 7.8 earthquake occurred in Seram and caused a submarine landslide tsunami along the southern coast of Seram (Brune et al., 2010) (Figure 2.3). The earthquake might have ruptured both the Kawa and Bobot faults in Seram (Watkinson and Hall, 2017). The recent 2019 M_w 6.5 Kairatu earthquake occurred offshore between Seram and Ambon. This earthquake was interpreted to have ruptured a north-trending fault offshore (Sahara et al., 2021).

Chapter 3

Methodology

Earthquake geology is a branch of geological study dealing with active faulting. It combines interdisciplinary fields, such as tectonic geomorphology, paleoseismology, and shallow-subsurface geophysics to uncover the nature of active faults, including surface trace locations, slip rates, paleoseismic history, and recurrence intervals of large earthquakes (McCalpin, 2009; Yeats et al., 1997). These methods were used in this research and are explained in the following sections.

3.1 Tectonic geomorphic interpretation

Active faults can be identified if they deform the late Quaternary geomorphic surfaces or strata (e.g., Burbank and Anderson, 2012; Tsutsumi and Perez, 2013; Yeats et al., 1997). Evidence of faulting activity on the surface can be expressed by tectonic geomorphic features such as fault scarps, offset rivers, beheaded rivers, pressure ridges, shutter ridges, linear valleys/depressions, and sag ponds (Figure 3.1) (Burbank and Anderson, 2012; Sieh and Natawidjaja, 2000; Yeats et al., 1997).

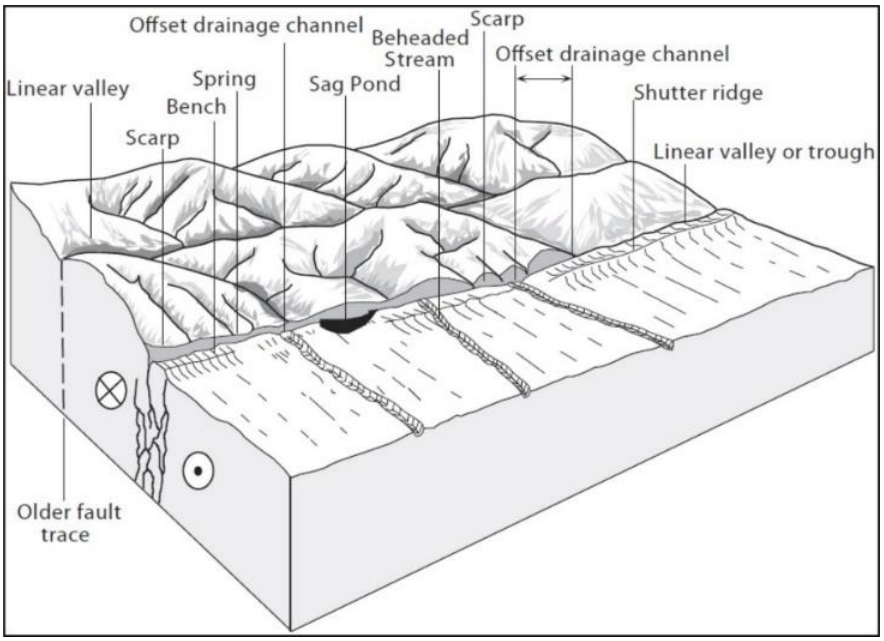

Figure 3.1 Tectonic geomorphic features associated with a strike-slip fault (Burbank and Anderson, 2012).

The geomorphic features may be preserved if the faulting rate overcomes the erosional or sedimentation rate. The study area is located in the tropical region where erosion and sedimentation

are intense, and the evidence of faulting activity may quickly be removed or covered. In addition, thick vegetation and artificial modifications may also obscure evidence of faulting activity.

Digital elevation models (DEM) of the earth's surface can be utilized for mapping the tectonic geomorphic features. The Indonesian DEM (DEMNAS) is available for the Indonesian region with a spatial resolution of 0.27 arc second or about 8.3 m (Figure 3.2a). DEMNAS is constructed from various sources, such as IFSAR 5 m, TERRASAR-X 5 m, and ALOS PALSAR 11.25 m, with additional mass point data based on stereo-plotting (https://tanahair.indonesia.go.id/demnas). In this research, the tectonic geomorphic interpretations primarily relied on the observation of DEMNAS. The Light Detection and Ranging (LiDAR) data with a resolution of 1.4–3 m also accompanied the DEMNAS for the study on the easternmost Matano fault (Figure 3.2b). In addition, photogrammetry-based surface mapping was utilized for the Ambon fault study using the DJI Mavic Pro Platinum drone. This technique produces digital surface model (DSM), not elevation model because topographic canopies such as vegetation and houses are included in the DSM. So, they should be considered for interpreting the results.

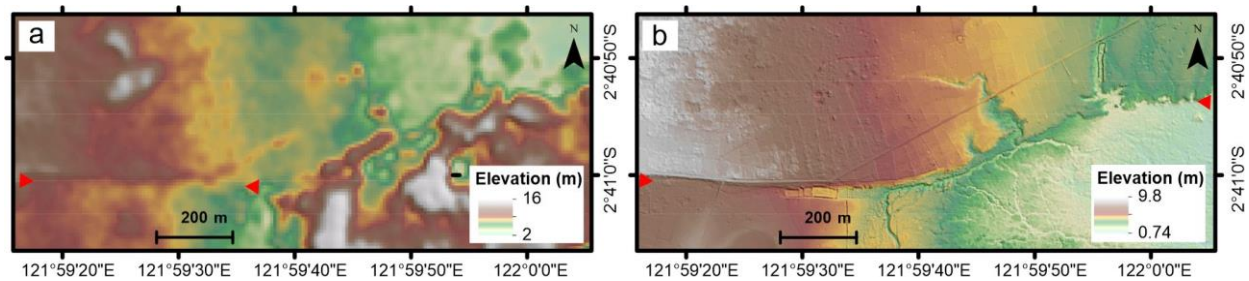

Figure 3.2 Comparison between DEMNAS (a) and LiDAR data (b).

DEMNAS and LiDAR data were processed to better visualize the geomorphology of the earth's surface. Several techniques were employed for the observation and interpretation such as slope calculation, hill-shading, and 3D anaglyph construction (Figure 3.3). The slope calculation translates the elevation variation as a function of the distance on the map, and it can be calculated in degree or percentage. The slope map highlights the changes in topography which are indicative of active faults. The hill-shade map shows the effect of light illumination on the surface topography. The illumination can be set in any azimuth and altitude, mimicking the sun's effect on hills and

valleys. This technique provides a clearer picture of the topography and a 3-dimensional appearance on the map. The hill-shade map usually serves as an underlay on a map, overlain by the DEM (Figure 3.3d). The color range of the overlying DEM can be manipulated so that the observation can be focused on a specific elevation. Additionally, the tectonic geomorphic analysis was done using 3D anaglyph images constructed from the DEM. This technique provides direct 3-dimensional visualization using red-and-cyan glasses and has been used for active fault identification (e.g., Goto et al., 2018; Shnizai, 2020). The investigation was then done by mapping the tectonic geomorphic features and interpreting the geological process that forms the features.

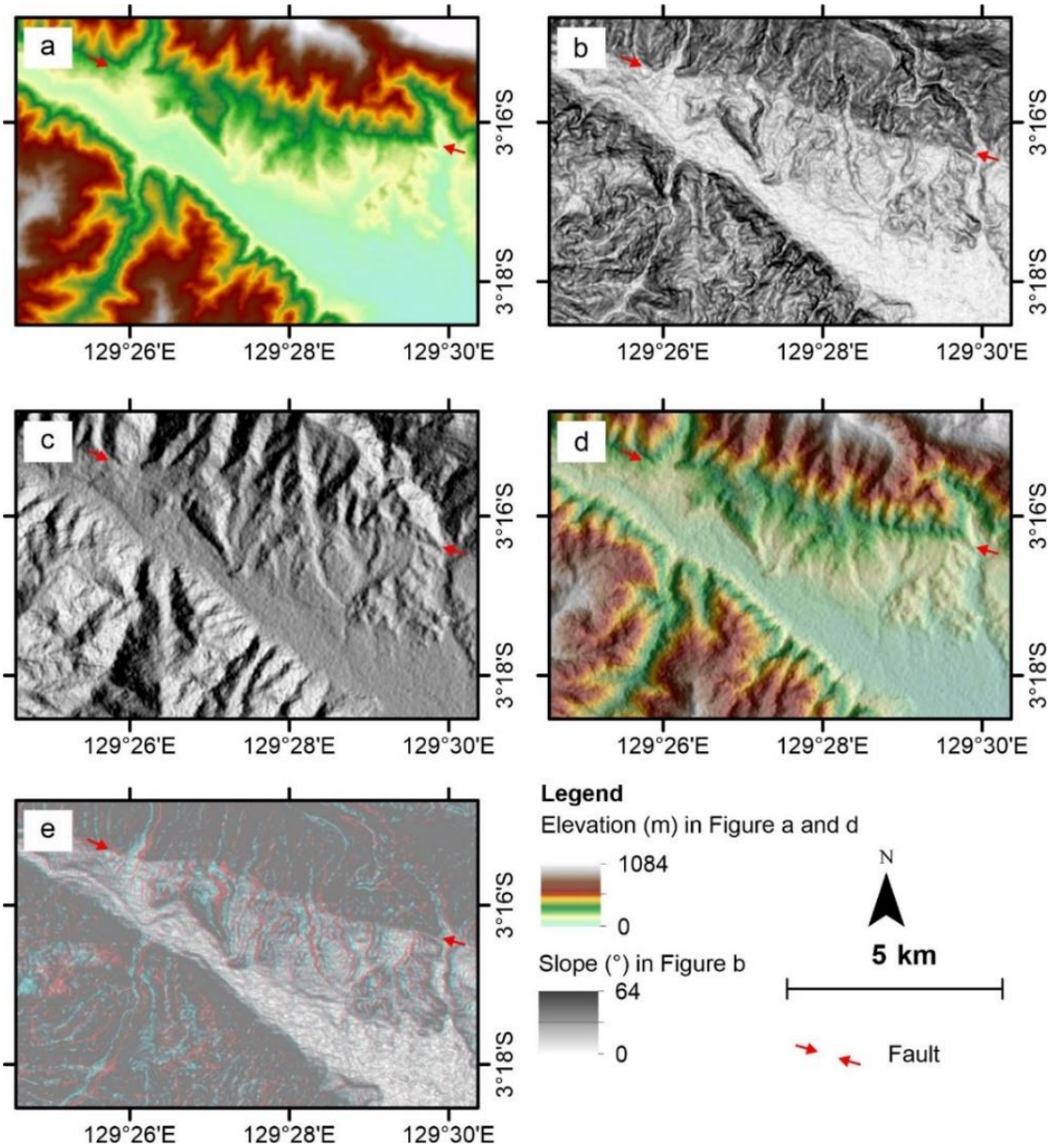

Figure 3.3 Example of maps used in this research: elevation model (a), slope (b), hill-shade (c), combined hill-shade as underlay and 50%-transparent digital elevation model (d), and 3D anaglyph maps (e).

3.2 Paleoseismic investigation

Paleoseismology examines the relationship between the stratigraphy, geomorphology, and active fault structures to reveal the timing, location, and magnitude of paleoearthquakes (McCalpin, 2009). Paleoseismic investigation can be conducted by exposing geological units and faults at the subsurface. This method has been widely used for investigating paleoseismic events along active faults in the world (e.g., Daryono et al., 2019; Dikbaş et al., 2018; Griffin et al., 2021; Perez and Tsutsumi, 2017). Evidence of surface-rupturing earthquakes can be identified as offset strata or geomorphic surfaces, fault terminations, and fissure fills (Figure 3.4). In this research, a paleoseismic trench excavation was performed on the Matano faults. Shallow borings on the deformed fluvial terrace were done for the Ambon fault study to collect representative samples for dating.

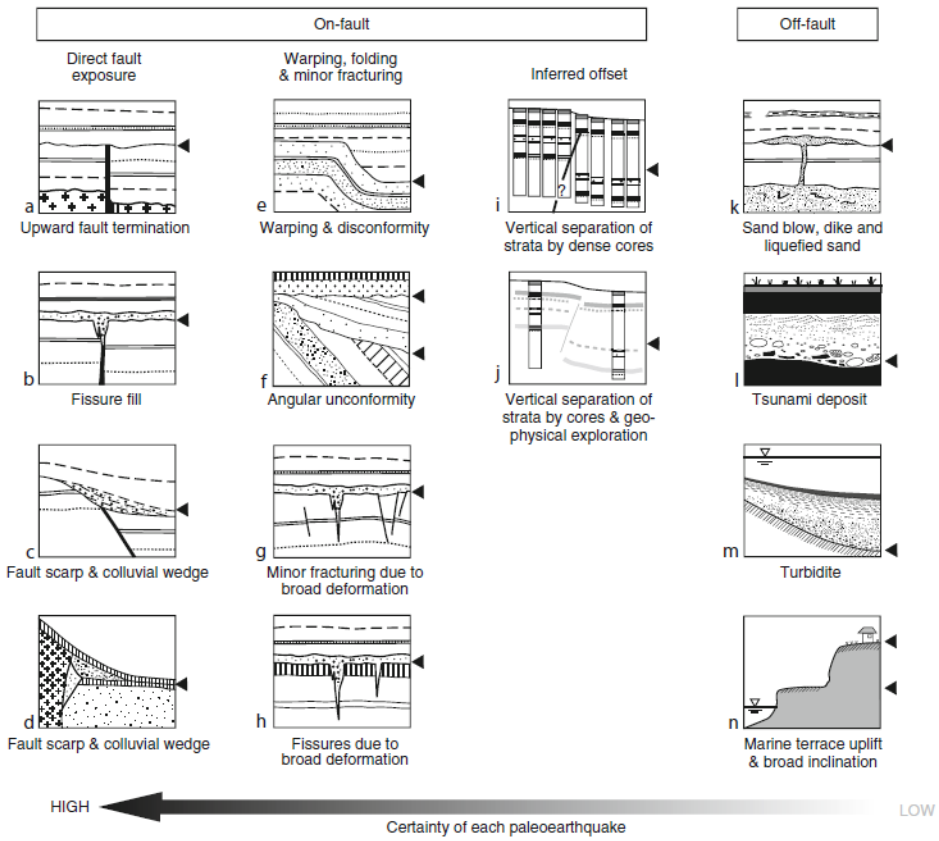

Figure 3.4 Typical indicators of paleoseismic events (Toda, 2011). The certainty of paleoseismic events increases from off-fault regions to on-fault ones.

Before excavating the paleoseismic trench, the site was located based on the interpretation of tectonic geomorphology, shallow-subsurface geophysics, and field inspections. The favorable site was young tectonic geomorphic features where the most-recent surface-rupturing earthquake might be recorded in stratigraphy. After the site selection, the trench layout was set on the surface, and then the trench was excavated (Figure 3.5a, b). The trench was oriented perpendicular to the active fault trace.

Figure 3.5 Steps of paleoseismic investigation: excavation by backhoe (a) and manpower (b), gridding the trench wall (c), and samples collection from sedimentary layers (d).

Once the digging was completed, the trench walls were cleaned to observe the sedimentary units and faults. The walls were gridded using nails and strings for spatial references (Figure 3.5c). Then, the walls were logged by drawing geological features on the graphic or tracing papers with the reference grid. The walls were also documented using the photomosaic technique which combines multiple overlapping pictures as a single image. Representative samples, such as charcoal and organic sediment from the sedimentary units were collected for absolute radiocarbon (^{14}C) dating (Figure 3.5d). The locations of the samples were also recorded on the logging paper.

After finishing these works, the trench had to be filled back using the previously excavated materials.

Samples were then sent to Beta Analytics, an accredited testing laboratory, for accelerator mass spectrometry (AMS) radiocarbon dating. Radiocarbon dating is a method that determines the absolute ages of organic carbon-based materials. AMS is an advanced radiocarbon dating technique that quantifies the ^{14}C content more efficiently than conventional radiocarbon dating (Linick et al., 1989). An age could be estimated by comparing the ^{14}C content against an international reference standard such as IntCal20 (Reimer et al., 2020) and SHCal20 (Hogg et al., 2020). Results of dating came as conventional radiocarbon age (years Before Present, yBP) which could be calibrated as the probability of calendar date (Figure 3.6) (Bronk Ramsey, 2009). The paleoseismic history was modeled using OxCal 4.3 program (Bronk Ramsey, 2009) based on the stratigraphic information and ages, following the technique by Lienkaemper and Ramsey (2009).

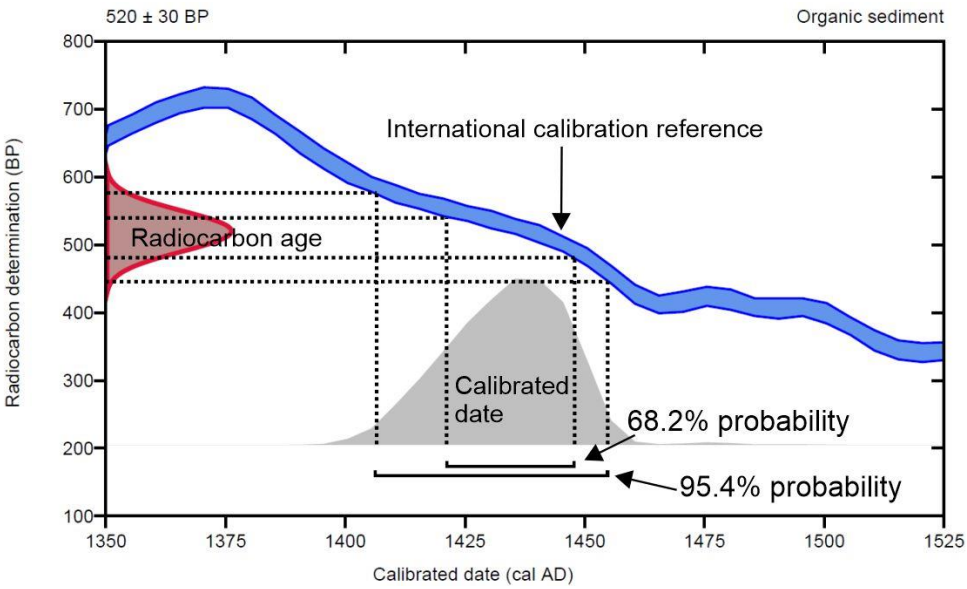

Figure 3.6 Example of age calibration of radiocarbon age.

3.3 Electrical resistivity tomography measurement

The electrical resistivity tomography (ERT) method is a near-surface geophysical technique that measures the resistivity of subsurface rocks and strata (Telford et al., 1990). It has been used to investigate subsurface geological structures, including active faults (e.g., Daryono et al., 2019; Fazzito et al., 2013; Peri et al., 2020; Suzuki et al., 2000). It injects electrical current through two

electrodes to the subsurface and measures potential difference at two other electrodes (Figure 3.7a). The apparent resistivity can be calculated based on the injected current and potential difference. The resolution and penetration depth depend on electrode spacing (Loke and Dahlin, 2002; Storz et al., 2000). Wider electrode spacing yields deeper penetration but lower resolution.

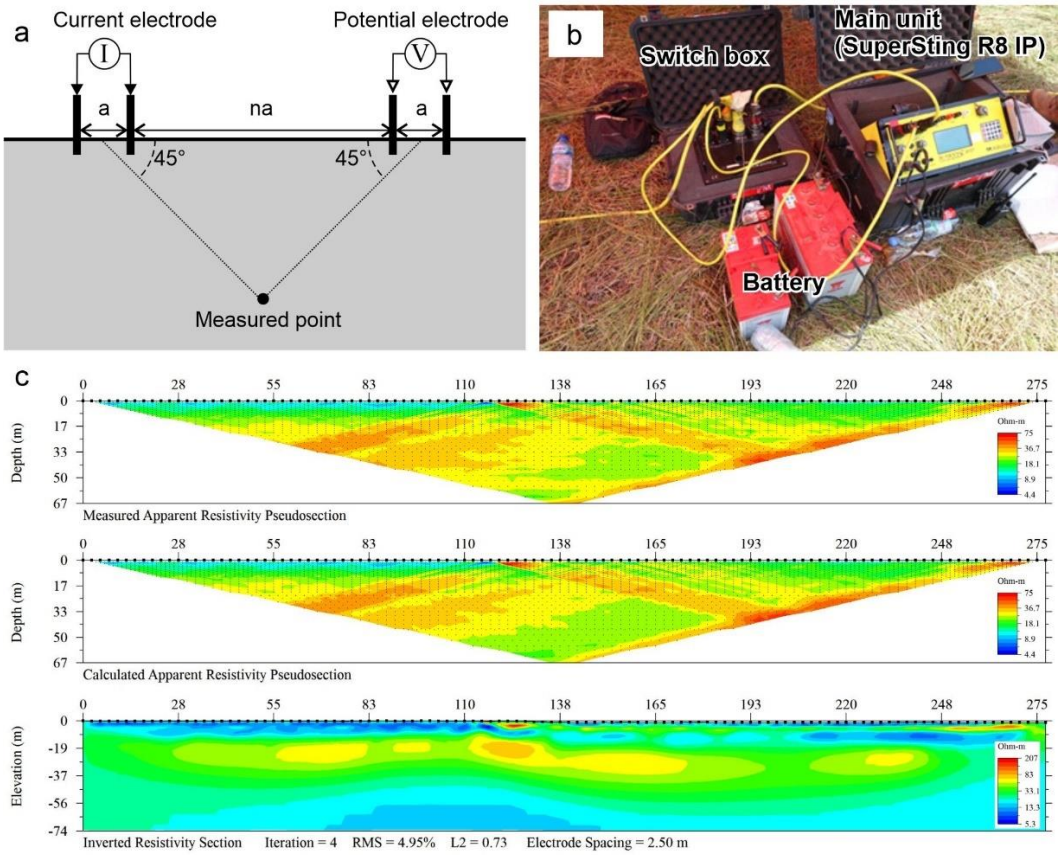

Figure 3.7 (a) A schematic diagram of the ERT measurement. *a* is electrode spacing, and *na* is the total distance of *n* electrodes. (b). The ERT instrument used for acquisition. (c) An example of the inversion of the ERT data.

The multi-channel resistivity instrument Supersting IP R8 from the AGI, USA (Figure 3.7b) was used in this research using 112 electrodes with a separation of 1.5–5 m, depending on the accessibility and targeted fault trace. The dipole-dipole configuration was set for measurement because it provides high-resolution, fast, and reliable measurements (Fazzito et al., 2013). The roll-along technique was also performed in a specific location to obtain an extended continuous profile. Table 3.1 show parameters for the acquisition of ERT sections.

Table 3.1 ERT measurement parameters

Instrument / Manufacturer	Supersting IP R8 / Advanced Geosciences Inc. (AGI), USA
Power supply	12V or 2x12V DC
Output current	1–2000 mA
Measuring resolution	Max 30 nV
Input channel	8 channels
No. electrode	112
Electrode spacing	1.5–5 m

The data processing was done using the EarthImager 2D software from the AGI USA to calculate the subsurface resistivity and produce final inverted resistivity sections (Figure 3.7c). The processing steps include topographic correction, forward modeling, and model inversion (Figure 3.8). The calculation employed the finite element method for the forward modeling and applied a maximum of 8 iterations to obtain the least error reduction. Then, the final inverted resistivity sections were interpreted by defining rock layers and faults.

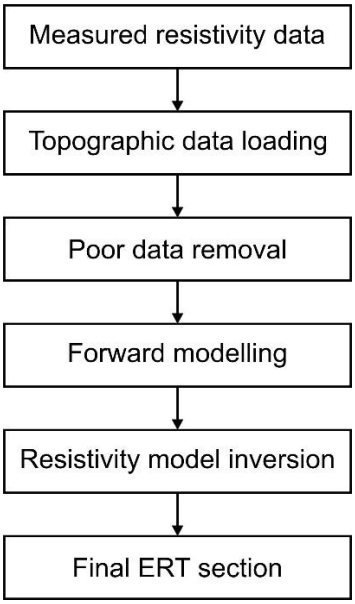

Figure 3.8 Flowchart of ERT data processing.

3.4 Ground-penetrating radar profiling

The ground-penetrating radar (GPR) profiling that uses electromagnetic waves is a typical shallow geophysical technique for imaging the shallow subsurface structures (Figure 3.9a) (Davis and Annan, 1989; Jol, 2008). The penetration depth is a function of the antennas' frequency, and the deeper penetration depth requires a lower frequency (Smith and Jol, 1995). The GPR survey

has been widely used to investigate active faults (Beauprêtre et al., 2012; Dujardin et al., 2014; McClymont et al., 2010). In this research, the GPR instrument manufactured by the GSSI was employed, and it includes the SIR-3000 main control module, antennas, a transmitter, and a receiver (Figure 3.9b). The acquisition was conducted using the common offset mode with a 40 MHz frequency antenna and 2 m antenna separation. The step increment was set at 1–2 m. The acquisition parameters are summarized in Table 3.2.

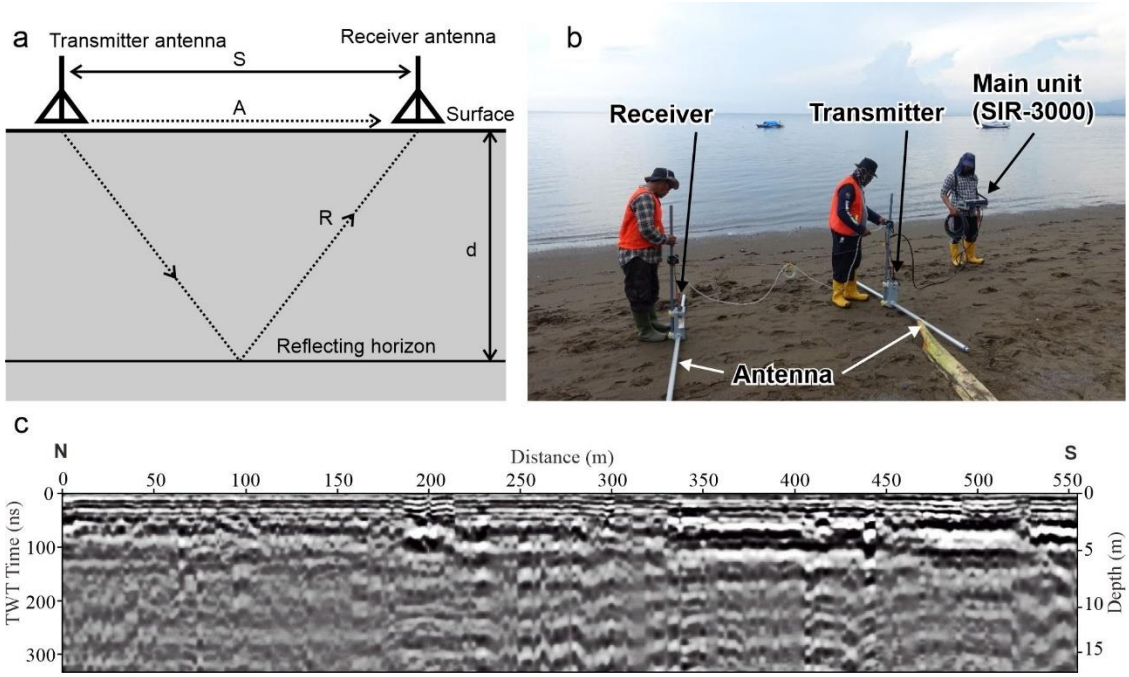

Figure 3.9 (a) A schematic diagram of the GPR profiling. *S* is antenna separation. *d* is depth between the surface and reflecting horizon. *R* is the path of electromagnetic wave at the subsurface. *A* is the direct airwave. (b) The acquisition of GPR profile in the field. (c) An example of the GPR profile.

The RADAN software of the GSSI was used to process the GPR data and produce the final GPR profiles (Figure 3.9c). The processing techniques includes time-zero shift, background removal, migration, deconvolution, frequency filtering, depth conversion, and topographic correction (Figure 3. 10). The interpretation of the final GPR sections was done by picking several distinctive reflectors and discontinuities including faults.

Table 3.2 GPR acquisition parameters

Instrument / Manufacturer	SIR-3000 / Geophysical Survey Systems, Inc. (GSSI), USA
Frequency	40 MHz
Transmitter-receiver spacing	2 m
Scan point interval	1–2 m
Number of channels	1
Sampling interval	16 ns
Number of samples per scan	512

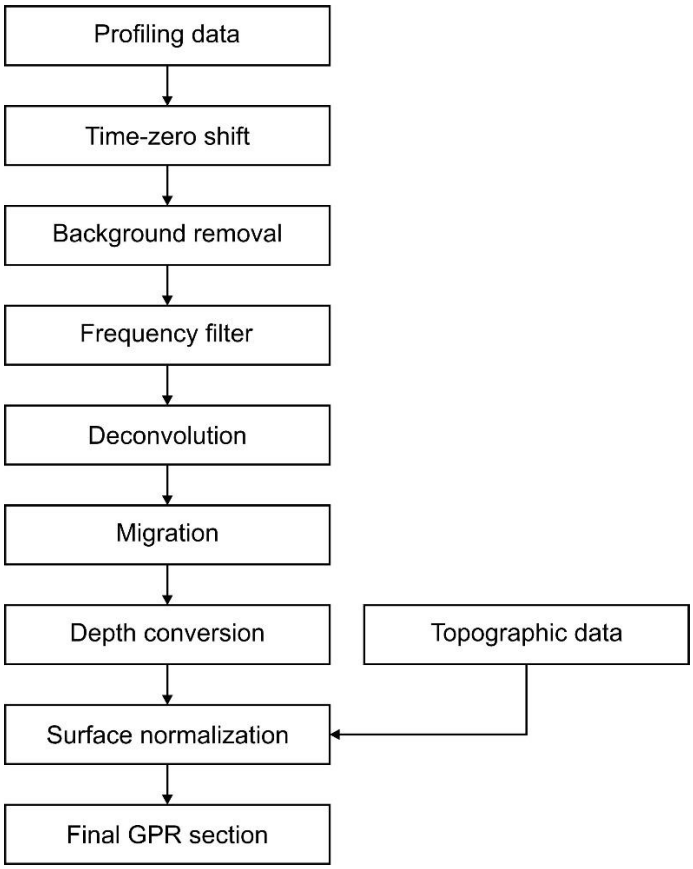

Figure 3.10 Flowchart of GPR data processing.

Chapter 4

Development of the Palu-Koro fault in the northwest Palu Valley, Sulawesi

4.1 Overview

The Palu-Koro fault is the major active left-lateral strike-slip fault in central Sulawesi with an almost north-south trend (Bellier et al., 2001; Daryono, 2016; Hamilton, 1979; Katili, 1970; Tjia, 1978; Watkinson and Hall, 2017). The fault extends for 220 km in central Sulawesi (Figure 4.1a). The fault connects to the Matano Fault at its southern end (Bellier et al., 2001; Hamilton, 1979; Socquet et al., 2006). To the north, the Palu-Koro fault continues offshore and terminates at the western end of the north Sulawesi trench (Hall and Wilson, 2000; Hamilton, 1979; Rangin et al., 1999). The convergence rate of the subduction trench increases westward from 20 to 54 mm/yr, resulting from a clockwise rotation about a pole located at the northeastern Sulawesi (e.g., Bock et al., 2003; Rangin et al., 1999; Stevens et al., 1999; Walpersdorf et al., 1998b).

Palu Valley was formed due to transtensional tectonics associated with the Palu-Koro fault (Bellier et al., 2006, 2001). The valley is bounded by high mountains trending north-south in the east and the west, reaching an elevation of 2.3 km (Figure 4.1b). The high mountains dominantly consist of metamorphic complexes and granitic rocks (Sukamto et al., 1973). Bellier et al. (1999) noted two distinct alluvial fan units within the western Palu Valley with abandonment ages of ~11 kya (kilo years ago) and ~120 kya, respectively, for young and old alluvial fan units. The western mountain comprises highly linear scarps, while the eastern mountain is relatively more eroded and segmented (Figure 4.1b) (Watkinson and Hall 2017). To the south, the Palu-Koro fault traverses a narrow valley, and the fault segments are linked by a northwest-trending releasing bend. The movement of the fault is indicated mainly by left-lateral stream offsets observed in the northern and southern parts of the fault (Bellier et al., 2001, 1998; Watkinson and Hall, 2017).

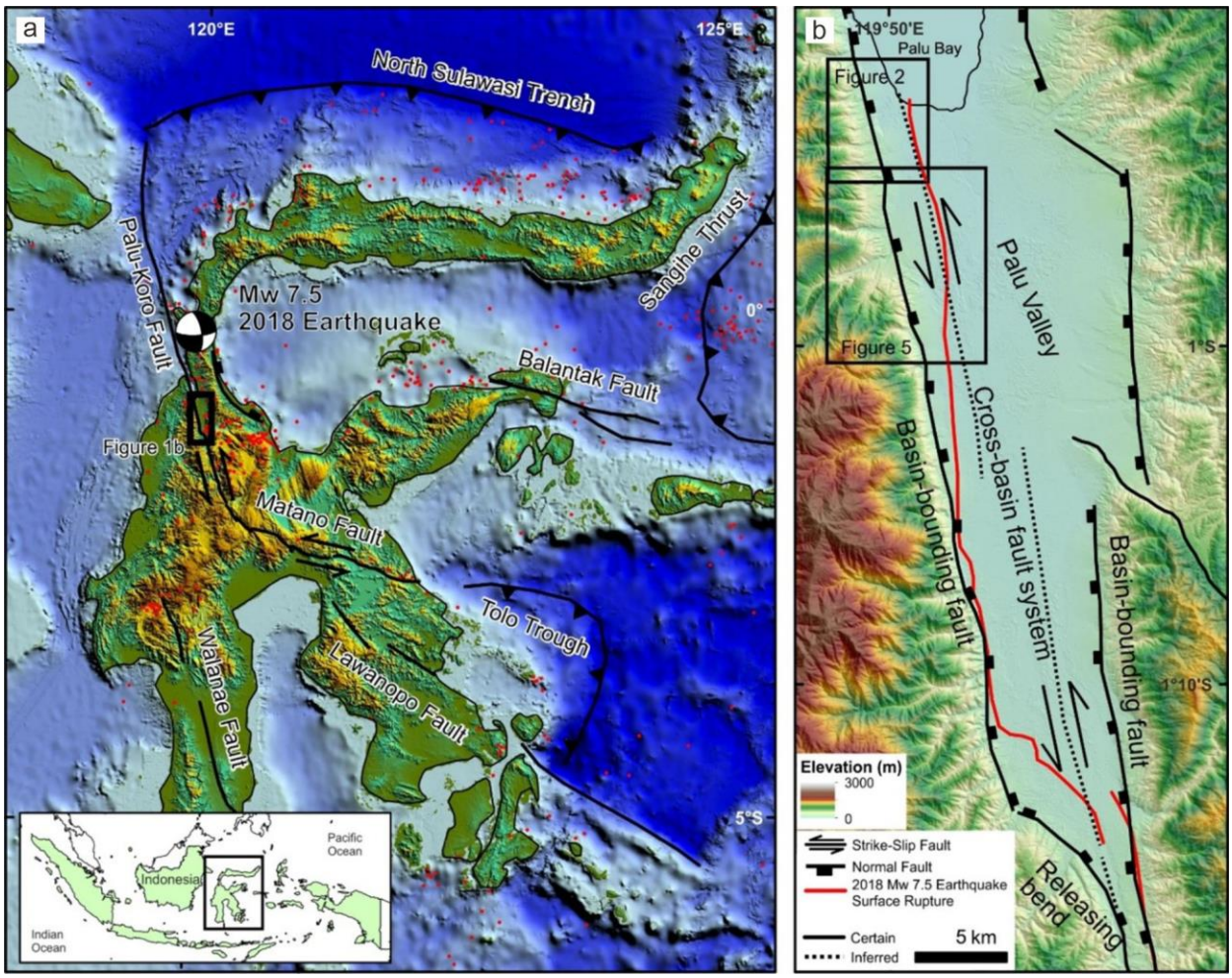

Figure 4.1 (a) Tectonic map of Sulawesi (compiled from Hall (2012), Hall and Wilson (2000), Hamilton, (1979), and Hinschberger et al. (2005)). Red dots indicate earthquake hypocenters with an $M_w \geq 4.5$ during 1980–2016 and moment tensor of M_w 7.5 2018 Palu earthquake from USGS Earthquake Catalogue. (b) Map showing morpho-structural elements of Palu basin. Palu depression including Palu Bay and Palu Valley is bounded by two mountains. Structural Elements in Palu Valley are compiled from previous authors (e.g., Bellier et al., 2001; Socquet et al., 2019; Watkinson and Hall, 2017). Note that the figure number for references in this figure refers the next figures in this chapter. (i.e., Figure 2 means Figure 4.2). This applies for figures in Chapter 4–6.

A paleoseismology work by Bellier et al. (1998) revealed that there were three M_w 6.8–8 earthquakes during the last 2000 years on the Palu-Koro fault with a recurrence interval of ~700 yr. If each earthquake had 10 m lateral displacement, the total slip should be 30 m for 2000 years. This total displacement is less than the predicted cumulative slip of 54–86 m for 2000 years if the slip rate is 35 ± 8 mm/yr. Thus, Bellier et al. (2001) argued a creeping mechanism for the Palu-Koro fault. Alternatively, Watkinson and Hall (2017) proposed that a cross-basin strike-slip fault

system, which may be covered by fluvial deposits and lacks clear geomorphic expression, accommodates the lateral slip deficit. Daryono (2016) also observed that the recent activity of the fault in the northern Palu Valley is expressed by fresh geomorphic features in the middle of the valley, and the western sidewall fault in the northwestern Palu Valley is inactive.

Seismicity analysis indicates that the Palu-Koro fault remains active with clustered source locations, and the faulting activity is dominated by a combination of strike-slip, normal, and thrust fault earthquakes (Pakpahan et al., 2015). The fault poses a significant seismic risk in eastern Indonesia because it is capable of generating large earthquakes (e.g., Bellier et al., 1998; Cipta et al., 2017; Daryono, 2016; Stevens et al., 1999; Walpersdorf et al., 1998b; Watkinson and Hall, 2017). Indeed, on the 28th of September 2018, an M_w 7.5 earthquake occurred and ruptured the fault with up to 7 m left-lateral offset, extending 180 km and traversing Palu City (e.g., Bao et al., 2019; Jaya et al., 2019; Natawidjaja et al., 2021; Socquet et al., 2019). It was shortly followed by a 4–7 m high tsunami, possibly associated with submarine landslides (Putra et al., 2019; Sassa and Takagawa, 2019; Takagi et al., 2019). The hypocenter was located about 80 km to the north of Palu City and at a depth of 10–15 km.

Although many studies have been undertaken concerning the Palu-Koro fault, its development remains enigmatic. The strike-slip fault development is essential for understanding the seismic behavior and evaluating the seismic hazard in a strike-slip basin. This study aims to interpret the tectonic geomorphology and map the surface rupture of the most recent earthquake based on field investigations and DEMNAS interpretations on the northwest Palu Valley. The results were combined to produce an evolutionary model of the Palu-Koro fault.

4.2 Tectonic landforms and surface ruptures

4.2.1 North area

Topographically, the northern part of the study area is characterized by a mountain in the west and low-lying plains in the east (Figure 4.2a). Two distinct alluvial fan units are observed in this area (Figure 4.2b). The old alluvial fan unit elongates in a north-northwest direction, bounding

the mountain to the west. It is dissected by the feeder channels of the young alluvial fan unit which is located east of the old alluvial fan unit. East of Kalora Village, the axis of a young alluvial fan is slightly deflected to the north from its feeder channel (Figure 4.2b). In the field, at the bend of the feeder channel (STD3-11), a lithological change from granite in the mountain to conglomerate in a hill indicates a basin-bounding fault contact in between (Figure 4.3a). The relationship between both alluvial fan units is also clearly shown in the south of Kabobena where the young alluvial fan truncates the old alluvial fan (Figure 4.3b). Both alluvial fans are separated by a 68 m linear topographic break, which may represent a normal fault scarp (Figure 4.3b and Figure 4.4a). North of Balaroa, a north-south oriented ridge on the young alluvial fan is elevated about 7 m above adjacent ground (Figure 4.2b and Figure 4.4b). Several ridges with a similar trend are also identified further north till reaching the coastline. The transpressional deformation related to the Palu-Koro fault might have formed these ridges.

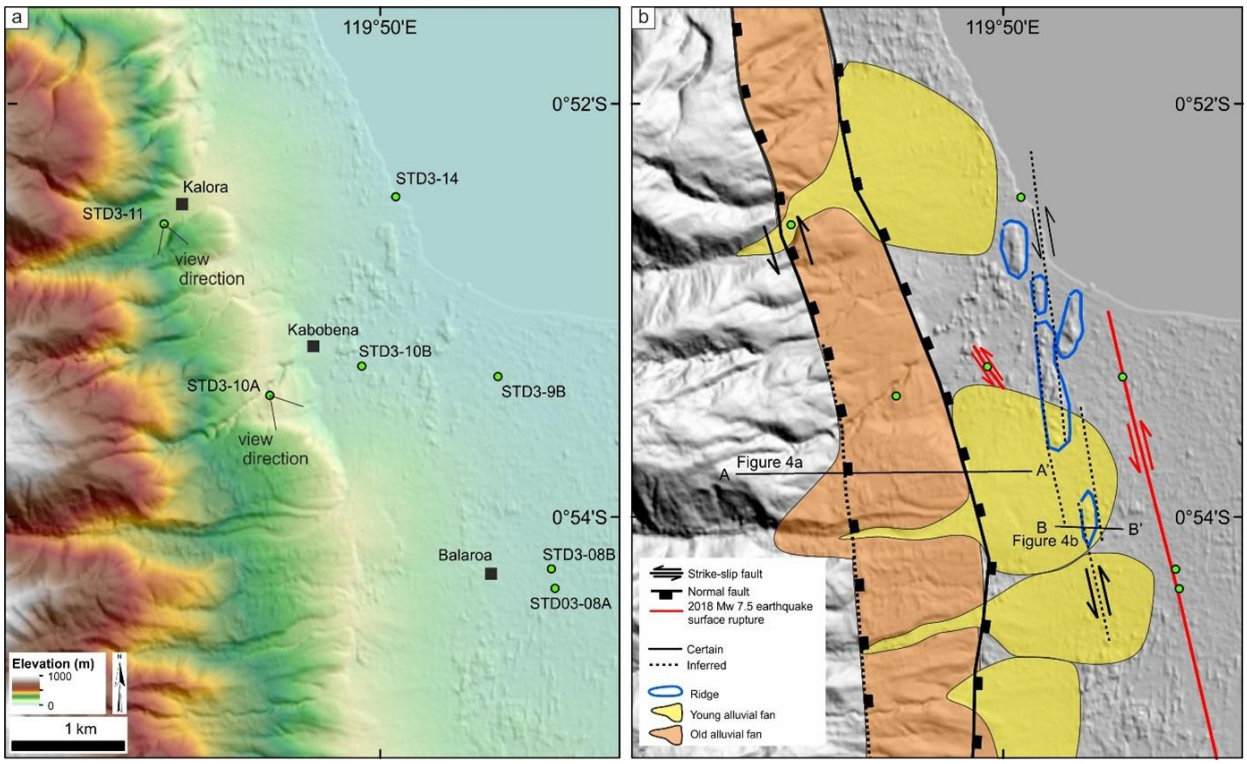

Figure 4.2 (a) DEM map showing the geomorphology of the north area and observation sites. (b) Interpretation of DEMNAS combined with field observation on a hill-shade image showing geomorphic features of the area.

Figure 4.3 (a) A view from STD3-11 showing contact between granite in mountain and conglomerate further east. A depression in between is interpreted as a basin-bounding fault. (b) A view from STD3-10A showing the relationship between old and young alluvial fan units. A topographic break may indicate a normal fault. (c and d) Major surface rupture with left-lateral displacement close to Balaroa at STD3-08B and STD3-9B, respectively. (e) Minor surface rupture at STD3-10B showing left-lateral displacement. (f) Subsided surface on the beach at STD3-14

The surface rupture of the 2018 Palu earthquake was also investigated. Evidence of the major surface rupture is shown in several locations in the western part of Palu City (STD3-8A, STD3-8B, and STD3-9B) showing a left-lateral offset up to 4 m along an N350°E direction (Figure 4.3c, d). Further west from the major surface rupture, on STD3-10B, a road is left-laterally displaced 60

cm with several minor strike-slip faults trending N320°E, which are interpreted as a minor surface rupture (Figure 4.3e). On STD3-14, there is a subsided beach with a vertical displacement of 1.5 m (Figure 4.3f).

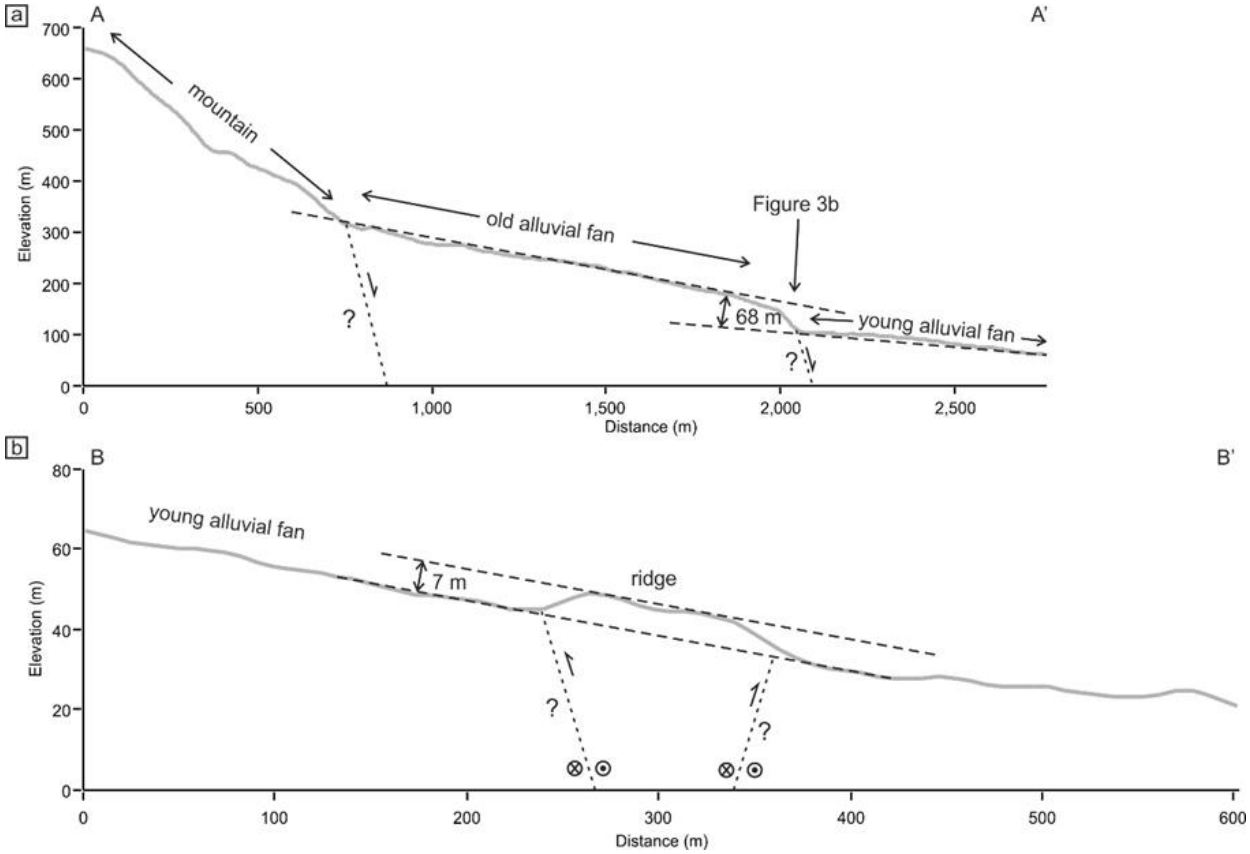

Figure 4.4 (a) Profile A−A' showing the topography from the mountain to the young alluvial fan. A topographic break between the mountain and the old alluvial fan may mark the basin-bounding fault. A scarp separating old and young alluvial fans is interpreted as a normal fault. (b) Profile B−B' of an intra-basin ridge, which emerges from adjacent topography on a young alluvial fan. See Figure 4.2 for the location of profiles

4.2.2 South area

The old and young alluvial fan units are identified east of the mountain, but the old alluvial fan unit disappears further to the south (Figure 4.5). East of Porame Village, there are two young alluvial fans. The younger alluvial fan deposition seems to be deflected to the north and partly overlies the other alluvial fan (Figure 4.5b). At STD3-03, a lithological change from phyllite to alluvial fan deposits is identified on the river (Figure 4.6a). To the south of the river, the alluvial fan deposit shows a horizontal stratification (Figure 4.6b). The intensively sheared basement rock

of phyllite is in contact with the alluvial fan deposit. (Figure 4.6c). The sheared phyllite appears as a damage zone of the fault, thus it is interpreted as a basin-bounding fault.

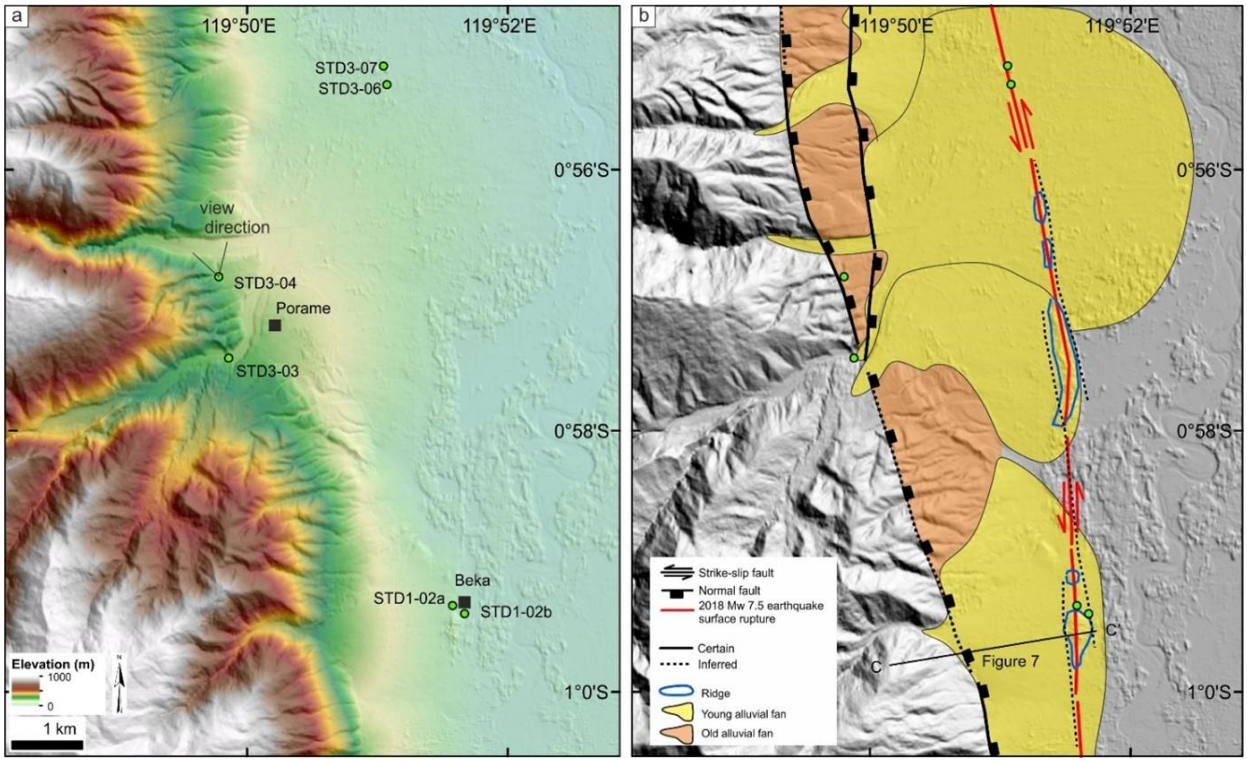

Figure 4.5 (a) DEM map showing the geomorphology of the south area and observation sites. (b) Interpretation of DEMNAS combined with field observation on hill-shade image showing two alluvial fan units and major geological structures.

Further north, at STD3-04, the evidence of normal faulting is reflected by the geometry of the old alluvial fan deposit which shows thickening-toward-fault geometry (Figure 4.6d). The topographic break between the mountain and the old alluvial fan unit marks the basin-bounding fault. West of Porame, north-trending ridges that emerge above the young alluvial fan suggest a transpressional deformation after the deposition of fans (Figure 4.5b). The 2018 earthquake surface ruptures cut these ridges.

Beka Village lies on the distal part of a young alluvial fan. The alluvial fan is sized about 2.5 km north-south and 2.2 km east-west. East of the village, a topographic break between the mountain and the alluvial fan is interpreted as a normal fault that controls the deposition of the alluvial fan (Figure 4.5b and Figure 4.7). At the distal part of the alluvial fan, the topography is slightly uplifted, forming a north-trending ridge. The 22 m rise of the ground is interpreted as due

to a transpressional deformation (Figure 4.7). The surface rupture of the 2018 Palu earthquake crosses this ridge in a parallel direction to the ridge orientation.

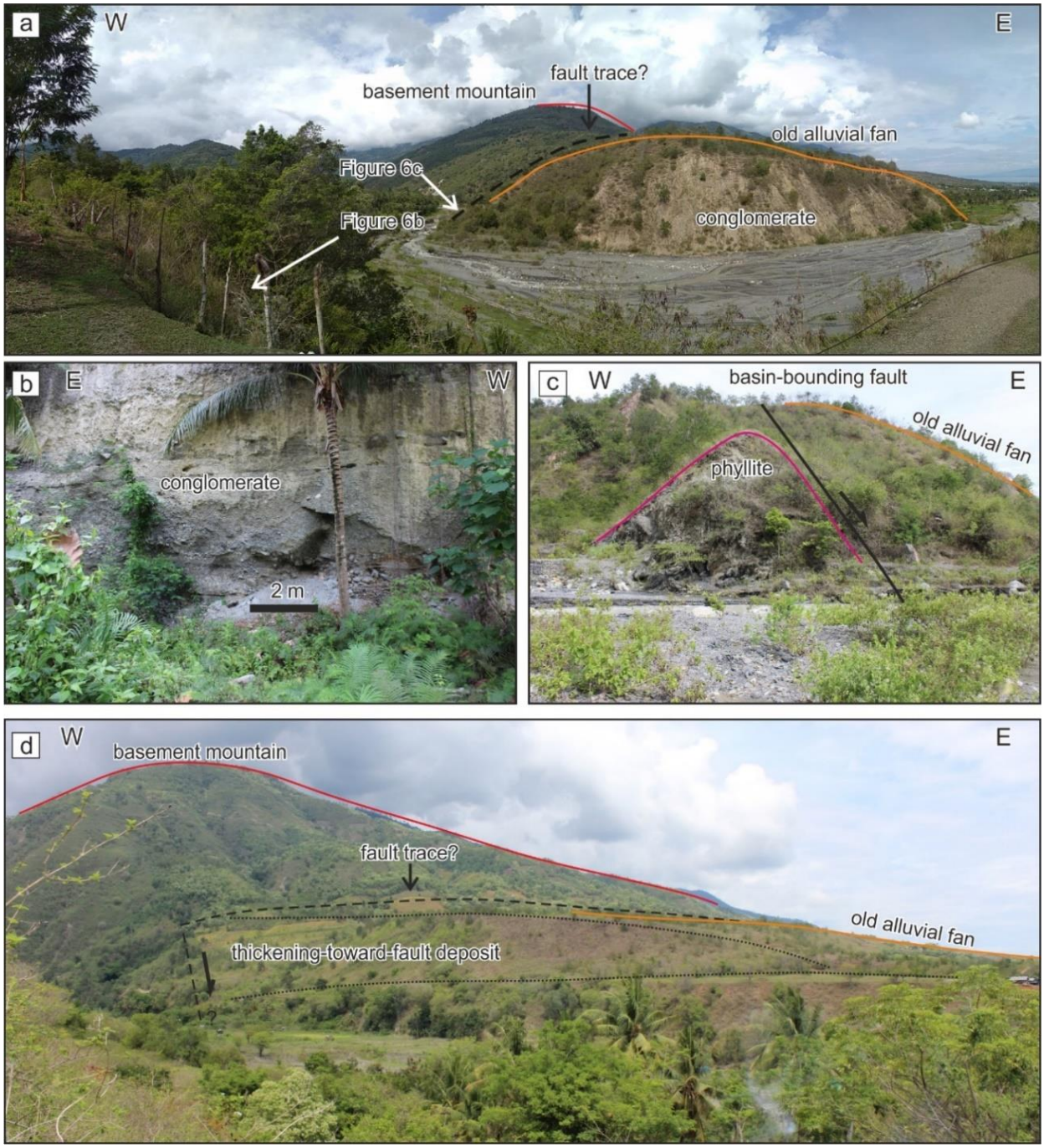

Figure 4.6 (a) Geomorphology of the western mountain, which consists of phyllite and the old alluvial fan in the west of Porame, STD3-03. (b) Horizontal strata of the old alluvial fan deposit. (c) Exposure of contact between phyllite and old alluvial fan deposit. Phyllite is situated at the footwall and highly sheared. (d) A view from STD3-04, showing the morphology of the mountain and the old alluvial fan. The appearance of the old alluvial fan indicates a thickening-towards-fault deposit.

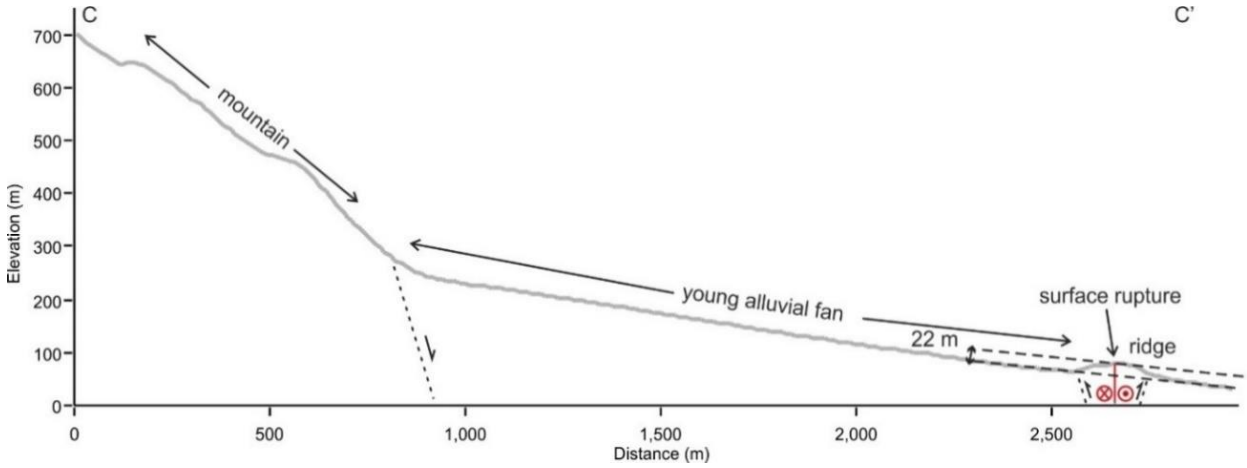

Figure 4.7. Profile C-C' showing the topography from the mountain to the young alluvial fan. Topographic break marks the basin-bounding fault, and a ridge is elevated 22 m from the adjacent surface. The ridge coincides with the major surface rupture of the 2018 Palu earthquake. See Figure 4.5 for the location of the profile.

Two distinct surface ruptures of the 2018 Palu earthquake are observed in Beka Village, summarized in Figure 4.8. The first is the major surface rupture which is located in the west of Beka Village. Evidence of left-lateral strike-slip faulting is indicated by the 2 m offset road (Figure 4.8b). The surface rupture is oriented north-south. Just north of the offset road, the ground is uplifted 50–70 cm (Figure 4.8c), and in contrast, south of the offset road a subsided land indicates 70–100 cm vertical displacement (Figure 4.8d). Although Beka Village is situated about 150 m east of the major surface rupture, the village also experienced minor surface deformation. The surface deformation indicates normal faulting with 1 m vertical displacement and 20 cm left-lateral offset (Figure 3.8e, f). The normal faults, which are connected by a relay ramp, have a relatively parallel trend to the major rupture. The normal faults elongate about 200 m and cannot be traced further north and south.

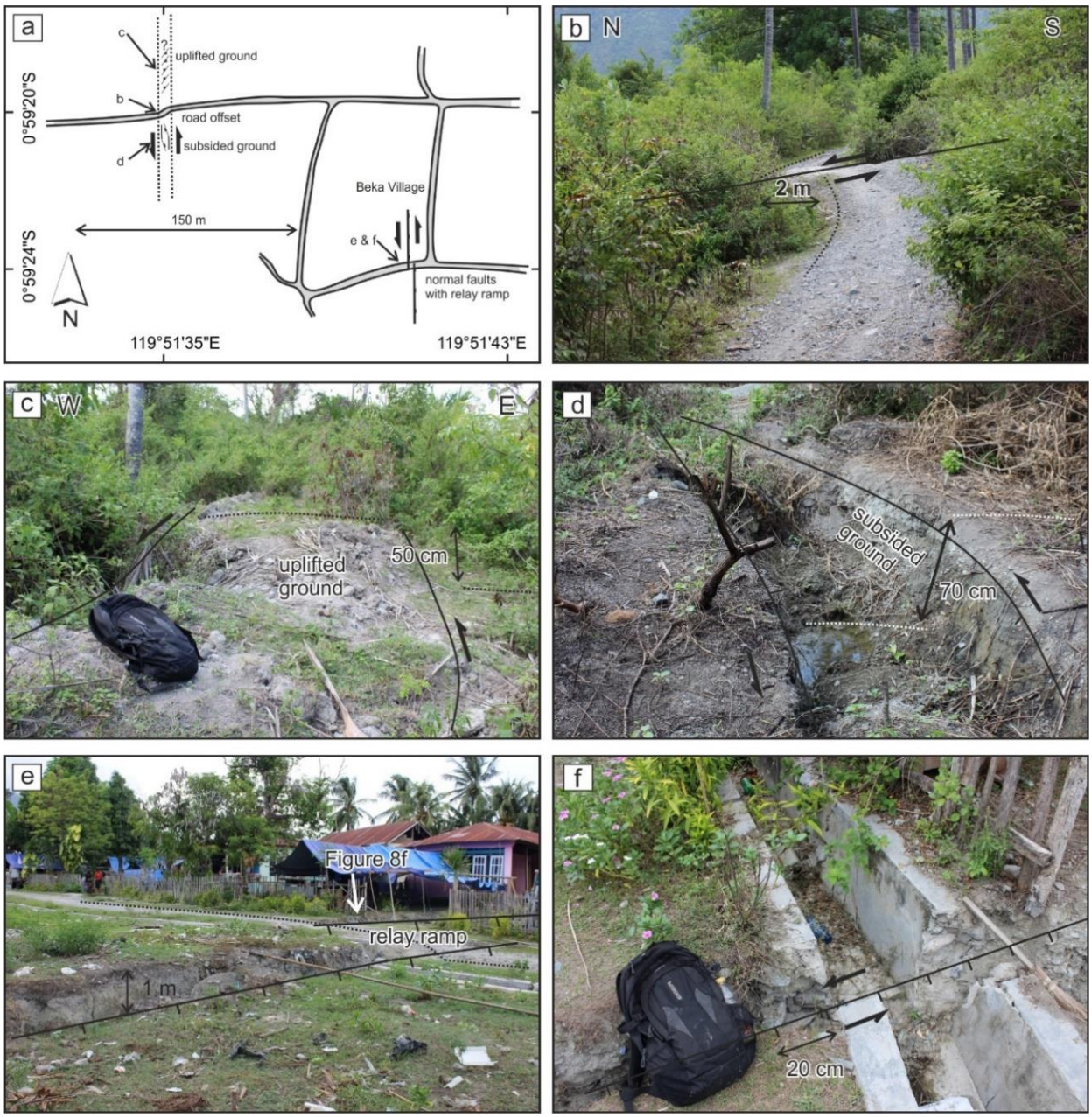

Figure 4.8 (a) Surface rupture of the 2018 Palu earthquake in Beka Village. (b) A 2-m left-lateral offset village road. (c) The ground was uplifted 50 cm above the adjacent surface. (d) Subsided ground with rhombic shape. (e) Normal faults with a maximum throw of 1 m, connected with relay ramp. (f) Close view of a normal fault, the fault has a minor strike-slip component of 20 cm.

4.3 Evolution of the Palu-Koro fault

The dynamics of the Palu-Koro fault are preserved in the field and expressed by geomorphic features. Three major faults are identified in the northwest Palu Valley. A basin-bounding fault is indicated by a prominent topographic break as the mountain front. The topographic break also marks the truncation of the old alluvial fan unit to the fault. The deposition of the old alluvial fan

unit was controlled by the basin-bounding fault, indicated by a thickening-toward-fault deposit. The basin-bounding faulting activity terminated at 120 kya (Figure 4.9a), suggested by the old alluvial fan unit's age (Bellier et al. 1999). Then, the faulting activity migrated to the east along the distal part of the old alluvial fan unit. The migration had initiated the deposition of the young alluvial fans further east, which dissect the old alluvial fans (Figure 4.9b). Bellier et al. (1999) measured that the young alluvial fans were dated at 11 kya.

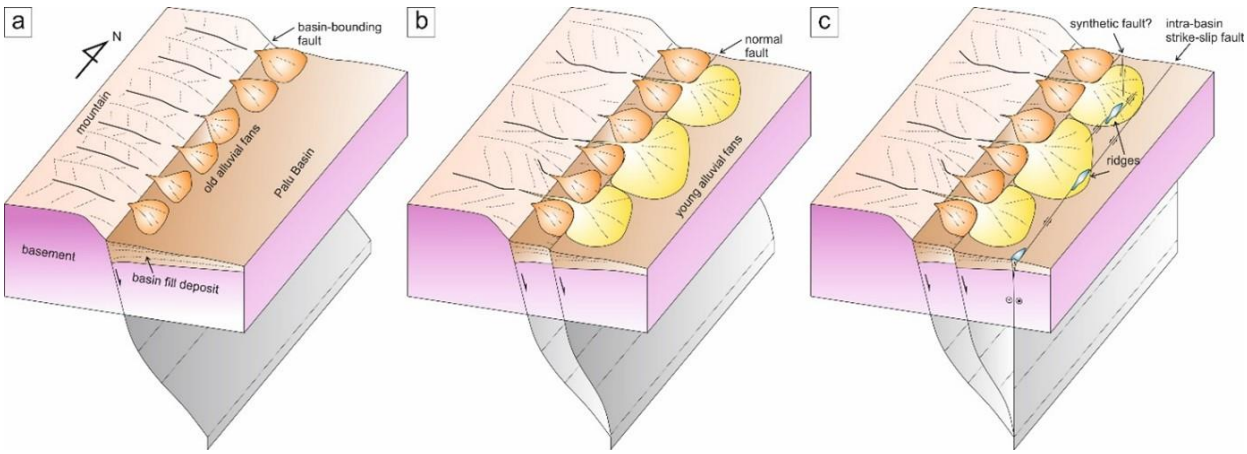

Figure 4.9. A schematic evolutionary model of the Palu–Koro fault in the northwest Palu Valley with the age of abandonments for two alluvial fan units from Bellier et al. (1999). (a) Deposition of old alluvial fans, controlled by a basin-bounding fault, which has a major normal slip component. This phase may end at 120 kya. (b) The episode of later normal faulting in the east, triggered the deposition of young alluvial fans, which truncated against the old alluvial fans. These alluvial fans were displaced after 11 kya. (c) Later deformation is dominated by strike-slip faulting. A series of north-south trending ridges uplifted distal parts of some young alluvial fans and may be associated with transpressional deformation. This strike-slip fault was ruptured during the 2018 Palu earthquake.

The recent faulting activity is mainly indicated by the deformation at the distal parts of young alluvial fans in which has formed north-south oriented ridges (Figure 4.9c). The ridges are uplifted from adjacent topography, indicating localized uplift due to the transpressional deformation. The ridges evidence that the recent activity of the Palu-Koro fault is accommodated by an intra-basin fault. This observation agrees with the interpretation by Daryono (2016), which suggested that faulting activity is expressed by fresh morphology within the northwest Palu Valley.

The migration of faulting activity was previously proposed by Watkinson and Hall (2017), and they inferred that the cross-basin fault diagonally elongates from the narrow valley, close to the releasing bend, till Palu Bay. However, the progressive migration of faulting activity from the basin-bounding fault toward the cross-basin fault has only been observed in northwest Palu Valley. The migration of faulting activity toward the basin center was also observed in other strike-slip fault systems in the world, such as Haiyuan Fault Zone (Zhang et al., 1989), Enriquillo-Plantain Garden-Walton Fault (Mann et al., 1995), and Kyaukkyan Fault (Crosetto et al., 2018). The migration might be caused by the tendency of strike-slip faults to straighten (Wu et al., 2009; Zhang et al., 1989).

The field inspection on the northwest Palu Valley has identified the 2018 earthquake surface ruptures with up to 4 m left-lateral offset. This observation agrees with the result from satellite imagery-based studies that show 4–7 m displacement (e.g., Bao et al., 2019; Socquet et al., 2019). The major surface rupture is evidence of the recent activity of intra-basin strike-slip faulting. In addition, there are also minor surface ruptures associated with the 2018 earthquake. The minor strike-slip surface rupture, close to Kabobena Village, could be an upward splay of the major rupture, or there might be a buried synthetic fault that was also ruptured during the 2018 earthquake. Another minor surface rupture with a significant normal slip component in Beka Village is interpreted due to gravitational collapse since it is parallel to the major surface rupture and has a limited extent.

Chapter 5

Earthquake geology of the easternmost Matano fault, Sulawesi

5.1 Overview

The 2018 M_w 7.5 Palu-Koro earthquake has been a reminder of earthquake hazards in Sulawesi. Much of the active fault research in Sulawesi has been concentrated on the Palu-Koro fault (Figure 5.1) (e.g., Bao et al., 2019; Bellier et al., 2001; Cipta et al., 2017; Natawidjaja et al., 2021; Patria and Putra, 2020; Socquet et al., 2019, 2006). The Matano fault is the southeastern continuation of the Palu-Koro fault (Silver et al., 1983). It is a prominent tectonic feature that can be recognized based on the distinctive geomorphic expression in central Sulawesi (Figure 5.1). Along the Matano fault, there were several small earthquakes (Figure 5.1b). Most earthquakes recorded left-lateral motion on the southeast-trending nodal plane agreeing with the Matano fault's motion. Another large earthquake was the 1998 M_w 7.7 South Sula earthquake east of Sulawesi (Vigny et al., 2002). The Matano fault is capable of generating $M_w \geq 7$ earthquakes (Cipta et al., 2017; National Center of Earthquake Study (PUSGEN), 2017; Watkinson and Hall, 2017),

However, the Matano fault remains less studied in terms of earthquake geology. Along the fault, its eastern portion is one of the vulnerable areas because modern seismicity is concentrated, possibly indicating a stress build-up in this portion (Figure 5.1b). The study of the easternmost Matano fault aims to interpret the tectonic geomorphology, assess the subsurface continuation, and reveal the paleoseismic history of the Matano fault, which aid in understanding active tectonics and seismic potential of the fault. This study provides comprehensive results of the tectonic geomorphic observations on the LiDAR (light detection and ranging) and the DEMNAS (Indonesian digital elevation model), electrical resistivity tomography (ERT) and ground-penetrating radar (GPR) surveys, and paleoseismic investigation on the 30 km easternmost portion of the Matano fault

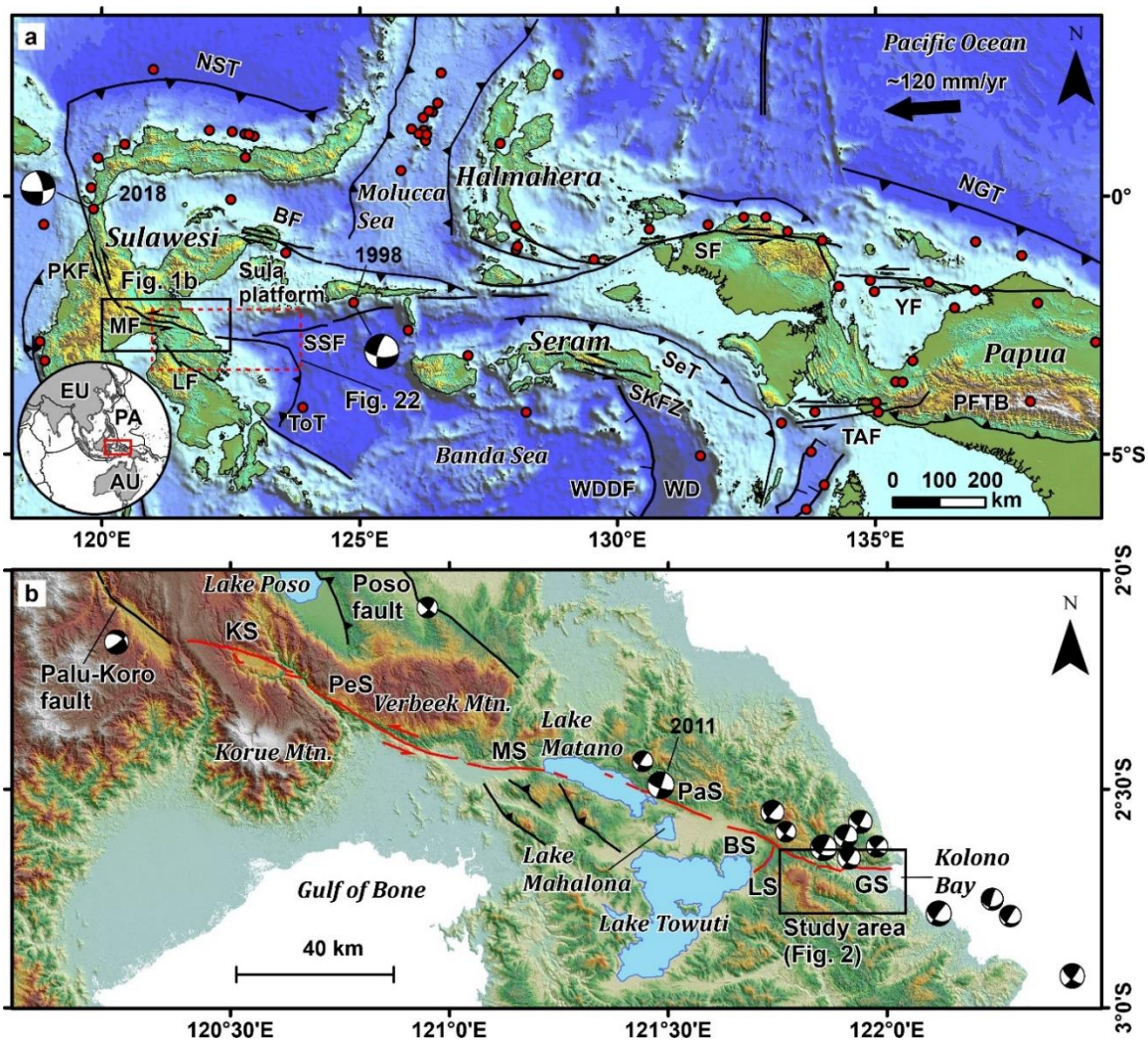

Figure 5.1 (a) Tectonic map of eastern Indonesia showing major structures around the region (Hall, 2012; National Center of Earthquake Study (PUSGEN), 2017; Pownall et al., 2016; Titu-Eki and Hall, 2020; Watkinson and Hall, 2017; Yang et al., 2021). BF: Balantak fault, LF: Lawanopo fault, MF: Matano fault, NGT: New Guinea trench, NST: North Sulawesi trench, PFTB: Papuan fold-and-thrust belt, PKF: Palu-Koro fault, SeT: Seram trough, SF: Sorong fault, SKFZ: Seram-Kumawa fault zone, SSF: South Sula fault, TAF: Tarera-Aiduna fault, ToT: Tolo thrust, WD: Weber Deep, WDDF: Weber Deep detachment fault, YF: Yapen fault. Red circles indicate the $M_w \geq 7$ earthquakes from the United States Geological Survey (USGS) earthquake catalog. (b) Segmentation model of the Matano fault (modified after Daryono, 2016; National Center of Earthquake Study (PUSGEN), 2017). Focal mechanism solutions of earthquakes are from the Global Centroid-Moment-Tensor (CMT) earthquake catalog. KS: Kuleana segment, PeS: Pewusai segment, MS: Matano segment, PaS: Pamsoa segment, BS: Balawai segment, LS: Lontoa segment, GS: Geresa segment.

Two LiDAR datasets, LiDAR-1 and LiDAR-2 were used to precisely map the active fault trace (Figure 5.2). These LiDAR data have a spatial resolution of 1.4–3 m and cover the central portion of the study area. The 8.3 m DEMNAS was also utilized for the area outside the LiDAR

coverage (Figure 5.2). The field inspection was also done to verify the tectonic geomorphology interpretation.

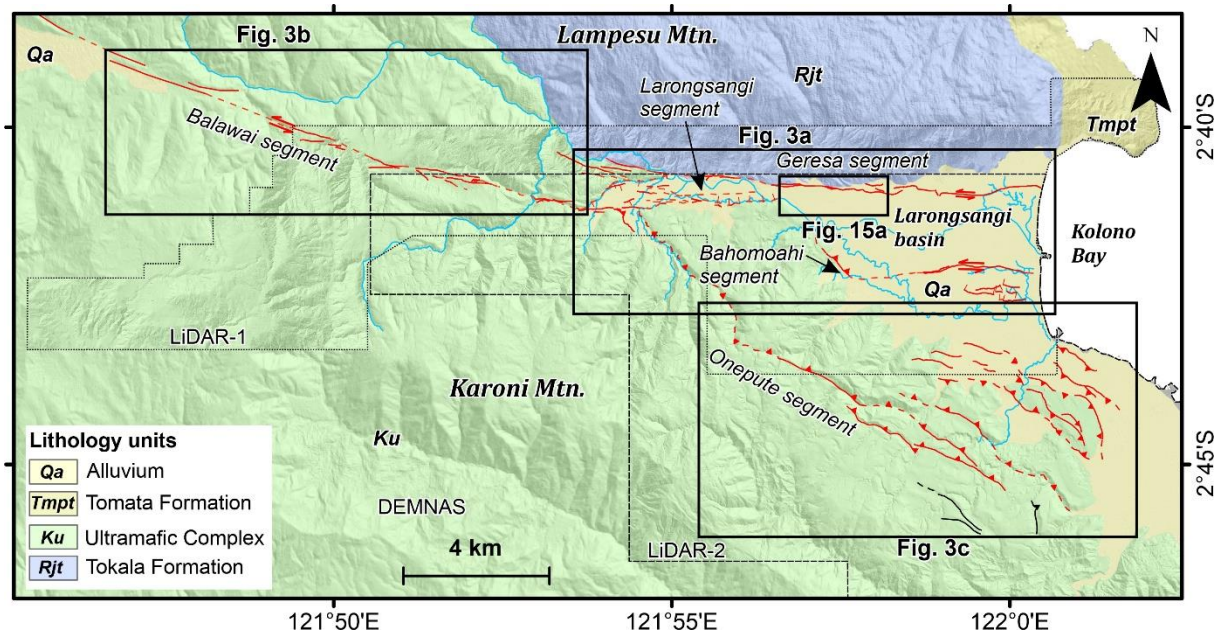

Figure 5.2 Geological map of the study area (modified after Simandjuntak et al., 1993), combined with active faults mapped in this study. The solid rectangles denote areas of Figure 5.3a–c. The dotted and dashed rectangles mark the LiDAR data's extent.

For the ERT measurement, twelve lines were oriented north-south crossing the active fault traces. The electrode spacing was set at 1.5–5 m depending on the accessibility and the active fault trace. The acquisition of the Line-7 section was performed using the roll-along technique to obtain an extended continuous profile. The GPR profiles were acquired along eight lines, aligned with some ERT lines. During the paleoseismic excavation, sand and gravel are dominant near the ground surface, and hence the electromagnetic velocity of 0.14 m/ns for these sediments (e.g., Davis and Annan, 1989; Iqbal et al., 2021) was used for the depth conversion. The names for each selected reflector were assigned and do not represent any correlation of reflectors among the GPR sections. The naming was intended to facilitate the description of the GPR sections.

5.2 Geology of the Larongsangi basin

The easternmost Matano fault traverses mountainous terrain and a basin near the Kolono Bay (Figure 5.2). There is no specific name for the basin, and it is termed "Larongsangi basin" after the main river that flows through the basin. The study area comprises pre-Quaternary and

Quaternary rock formations overlain by Quaternary alluvium (Simandjuntak et al., 1993). The ophiolite complex crops out in mountainous regions west and south of the Larongsangi basin. It contains a series of ultramafic igneous and metamorphic rocks. The Jurassic-Triassic clastic limestones occupy the Lampesu Mountain north of the basin. The Plio-Pleistocene clastic sedimentary rocks of the Tomata Formation are exposed north of Kolono Bay. The Quaternary alluvium unconformably overlies the older formations in the Larongsangi Basin.

5.3 Tectonic landforms and shallow-subsurface structures

The easternmost Matano fault is divided into five geometric segments based on major discontinuities, such as step-overs, bends, and changes in direction (Figure 5.2 and 5.3). The tectonic geomorphic features are described for each segment based on the LiDAR and DEMNAS data interpretation. A detailed active fault map for the Larongsngi basin is provided in Appendix A1. The subsurface evidence of faulting is shown based on the ERT and GPR measurements. In the following description, the term “distance marker (DM)” refers to the horizontal marker on the active fault map, and the “horizontal distance (HD)” indicates the horizontal marker on the ERT and GPR sections.

5.3.1 Geresa segment

The 14-km-long Geresa segment extends from the Kolono Bay, traversing the northern part of the Larongsangi basin (Figure 5.2). It may extend offshore further east. The segment trends almost east-west, although some of its strands trend northwest. At the eastern end of the segment, the segment is identified as south-facing fault scarps cutting the raised and modern beach ridges (Figure 5.3a). The fault scarps form a boundary between the raised beach ridges and swamps to the south (Figure 5.4a). The fault scarp on the modern beach ridges accompanies a sag pond. At location 1, ~ 7 m left-lateral ridge offset and ~1 m high fault scarp (Figure 5.4c, d) possibly represent the displacement of the most recent earthquake because they cut the youngest geomorphic surface, modern beach ridge. These displacements indicate that the ratio of vertical to horizontal offsets is about 12%.

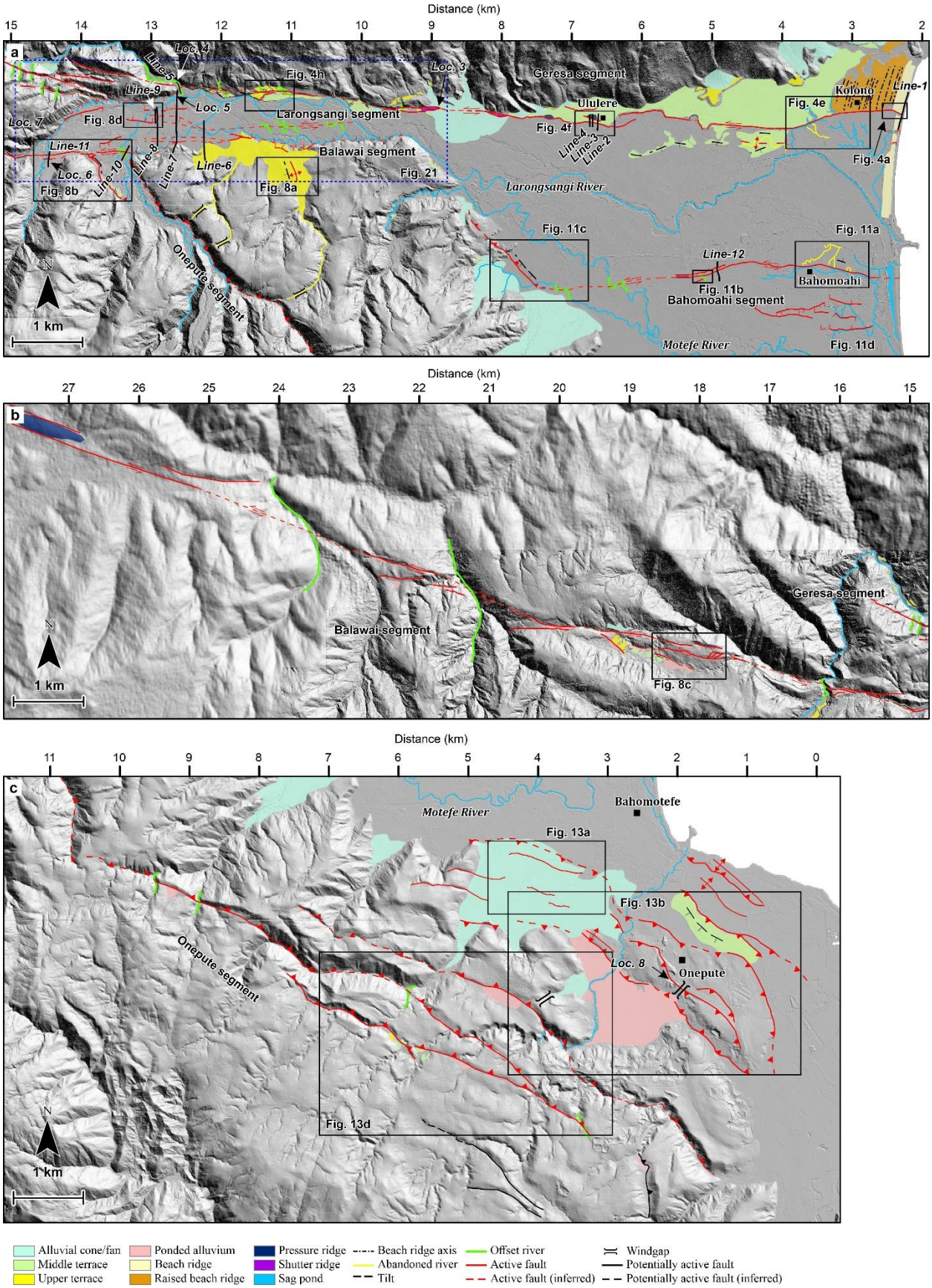

Figure 5.3 Active fault maps of the study area. The location of each map is shown in Figure 5.2.

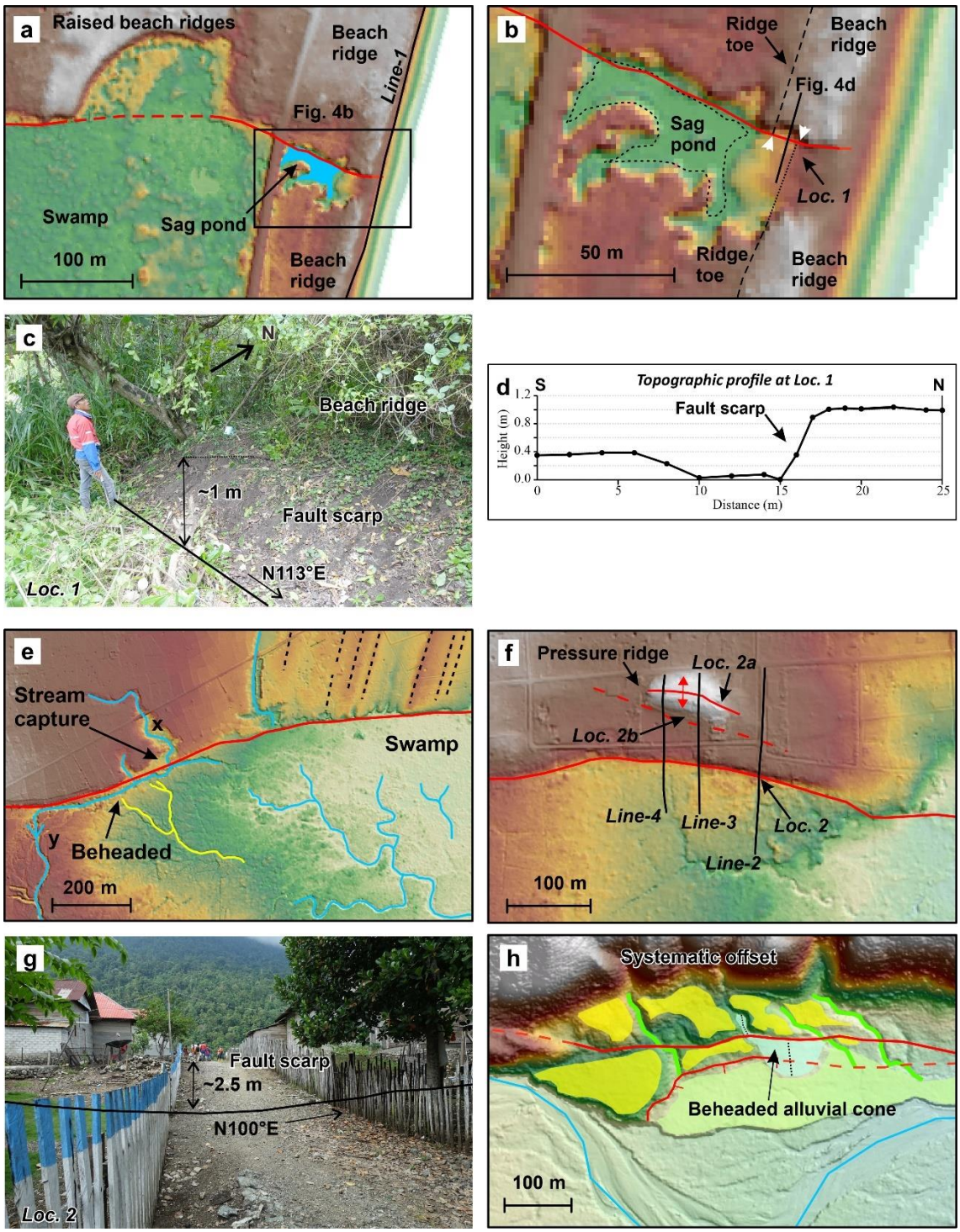

Figure 5.4 Typical geomorphic features of the Geresa segment. (a) Fault scarps and a sag pond at Kolono Beach. (b) Left-lateral offset of the beach ridge, 7 ± 1.4 m. (c, d) 1 m high fault scarp at location 1. (e) Stream capture and beheaded abandoned rivers south of Kolono. (f) Fault scarp and pressure ridge at Ululere. (g) 2.5 m-high fault scarp at location 2. (h) Faulted upper terraces with left-lateral river offsets.

The Line-1 was acquired in the eastern end of the Geresa segment (Figure 5.3a). The Line-1-ERT section illustrates deformed resistivity layers below 16 m depth, overlain by flat resistivity layers (Figure 5.5a). The high resistivity unit is interpreted as alluvium gravel, and the lowermost

moderate resistivity is a pre-Quaternary basement. Fault traces are recognized on the Line-1-ERT section. The main fault at the HD 310 m coincides with the fault scarp at the surface. The fault is marked by a resistivity contrast and a displaced high resistivity layer down to the south. It constitutes the Geresa segment at the subsurface. Besides the main fault, several faults deform the high resistivity layer. On the Line-1-GPR section, several faults are closely related to the faults on the Line-1-ERT section (Figure 5.5b). The fault between the HD 300 and 350 m displaces the reflectors B–D, and it agrees with the main fault on the ERT section. The main fault truncates the reflector A at a depth of 2 m, suggesting subsidence on the beach due to faulting activity.

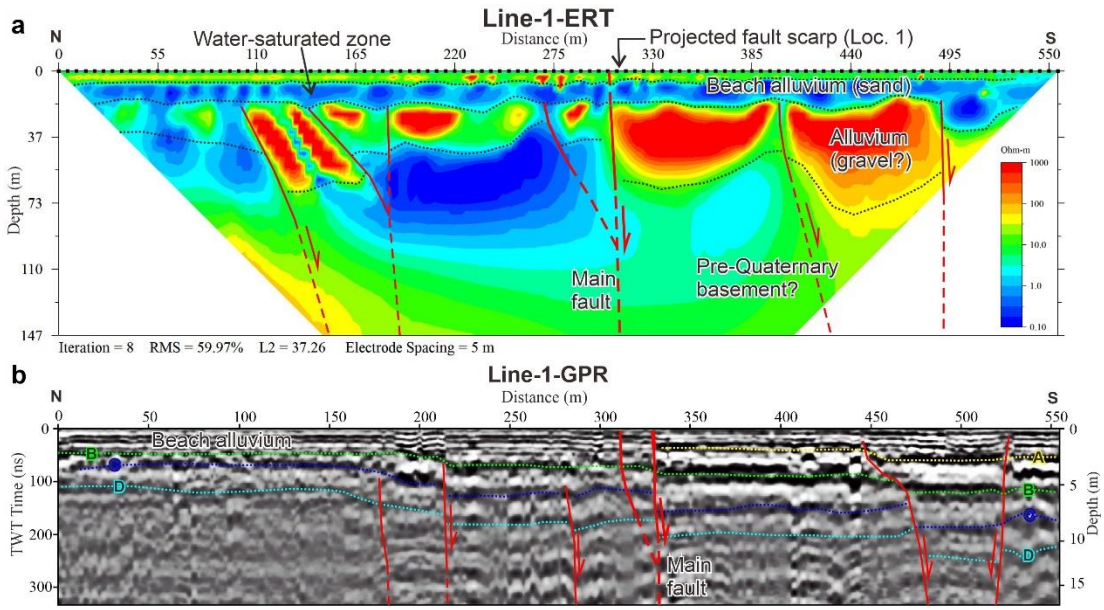

Figure 5.5 Interpretation of the Line-1-ERT (a) and Line-1-GPR sections (b).

The fault extends further to the west and steps left at the DM 6 km immediately before reaching Ululere. South of the fault, an anticline was identified at the DM 4–5 km, indicated by oppositely tilted terraces (Figure 5.3a). This anticline is associated with an abandoned river that was elevated higher than the adjacent surface. This feature represents the uplift due to folding. At Ululere, there is a prominent fault scarp, together with the east-trending ridge on the upthrown side (Figure 5.4f). The fault scarp's height is about 2.5 m (Figure 5.4g), more than twice the fault scarp on the beach ridge at location 1. Multiple earthquakes might have formed the fault scarp at Ululere. Between the DM 7 km and 8 km, three pressure ridges are aligned along the fault trace.

The ERT and GPR measurements were conducted along three lines crossing the fault scarp in Ululure (Figure 5.3a and Figure 5.4f). The ERT sections reveal that the main fault dips steeply northward and coincides with the fault scarp (Figure 5.6a–c). The high resistivity layer, interpreted as gravel, is consistently faulted on the sections. On the Line-2-ERT profile, the fault at the HD 88 m shows significant vertical displacement, but it does not extend to the surface. On the Line-3-ERT and Line-4-ERT sections, the northern fault appears responsible for the uplift of the Ululere Ridge. It is recognized as resistivity contrast and can be correlated to the fault on the Line-2-ERT at the HD 60 m. Sand at location 2a (Figure 5.4f) can be projected to the moderate resistivity layer beneath the Ululere Ridge on the Line-3-ERT section (Figure 5.6b). Black clay at location 2b (Figure 5.4f) represents the uppermost low resistivity layer on the Line-3-ERT profile (Figure 5.6b). The irregularity of the moderate resistivity layer (sand) on the Line-3-ERT and Line-4-ERT sections may indicate the existence of liquefied sand as sand boil below the ridge (Figure 5.6b–c).

The main fault displaces several prominent reflectors on the GPR sections (Figure 5.6d–f). On the Line-2-GPR section, the main fault offsets the reflectors A–D. The reflectors A1 and D1 onlap the reflectors A and D, respectively, at the main fault (Figure 5.6d). A similar feature exists on the Line-3-GPR profile where the reflector B1 onlaps the reflector B (Figure 5.6e). These features suggest that fault movements created accommodation space, and the main fault limited the sediments' extent. On the Line-2-GPR section, the reflectors C and D north of the main fault form an antiformal geometry overlain by flat reflectors. Antiformal reflections are also shown beneath the Ululere Ridge on the Line-3-GPR and Line-4-GPR profiles (Figure 5.6e–f).

There is no fault scarp observed on an alluvial fan surface at the DM 8–9 km. At location 3, a fault scarp is present near a shutter ridge at the DM 9 km (Appendix A2). The fault continues further west, traversing the mountain slope break (Figure 5.3a) before it cuts the upper terrace and beheads an alluvial cone at about the DM 11 km (Figure 5.4h). The fault scarp on the upper terraces is about 6–8 m high, and the left-lateral river offset is 40 m, suggesting that the vertical displacement is about 15% of horizontal offset, comparable to the ratio at location 1.

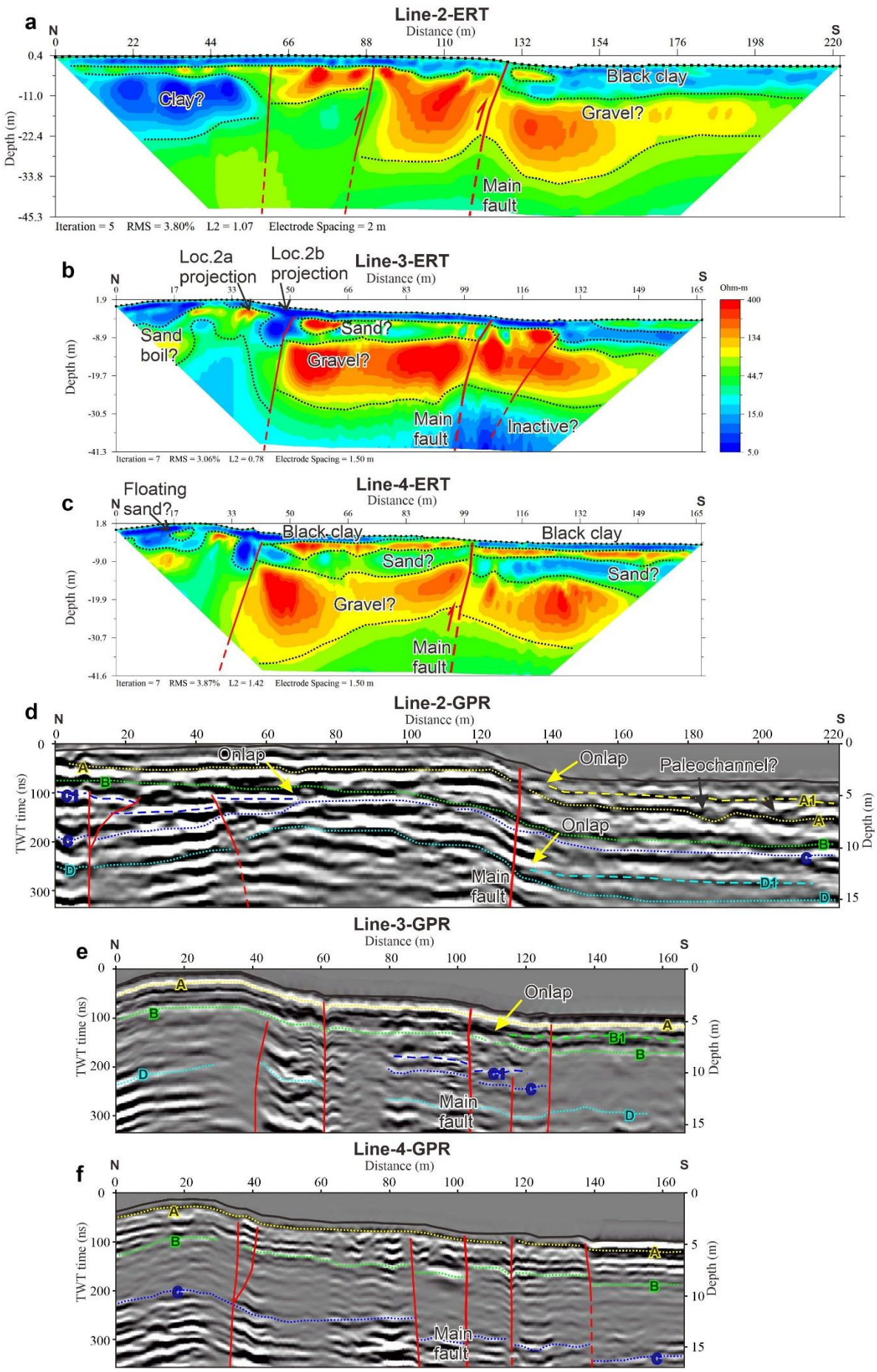

Figure 5.6 Interpretation of the Line-2–4-ERT (a–c) and Line-2–4-GPR sections (d–f).

At about the DM 13 km, the fault branches westward into several strands (Figure 5.3a). Several strands that traverse mountainous terrain forming uphill facing scarps slightly deviate northwestward. Systematic left-lateral river offsets are observed between the DM 14 km and 15 km. Exposure of the sheared basement rock at location 4 marks the fault zone (Appendix A2). The deformed serpentinite outcrop at location 5 (Appendix A2) indicates another fault at the boundary between mountain and basin. The slicken lines on a fault plane show predominantly left-lateral motion.

The Line-5-ERT profile shows that there are three fault traces at the subsurface (Figure 5.7). The fault at the DM 50 km represents the fault strand that extends to the mountainous terrain. This fault strand is marked by resistivity contrast and a tilted high resistivity layer near the surface. The southern fault trace is evident by truncation of the high resistivity layer at a depth of about 15 m, and it marks another strand that runs between mountain and basin.

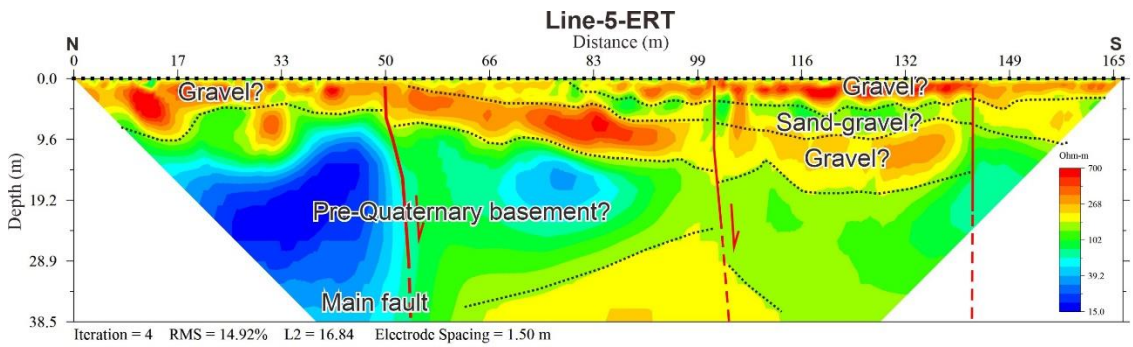

Figure 5.7 Interpretation of the Line-5-ERT section.

5.3.2 Balawai segment

There is a gap between the western and eastern parts of the Balawai segment. In this section, only the eastern portion of the Balawai segment is described. The Geresa segment steps left to the Balawai segment (Figure 5.2 and Figure 5.3a). The eastern Balawai segment is about 19 km long, and more than half of it traverses the mountainous terrain. It trends east-west at the DM 9–15 km and northwest from the DM 15 westward. This segment overlaps the western portion of the Geresa segment, forming a <1 km wide basin (Figure 5.3a). The fault trace follows topographic slope breaks from the DM 9 km to the DM 11 km and cuts the upper fluvial terrace to the west until

about the DM 12 km. At the DM 11 km, south of the fault, a north-south trending ridge on the upper terrace appears to be anticlinal uplift (Figure 5.8a).

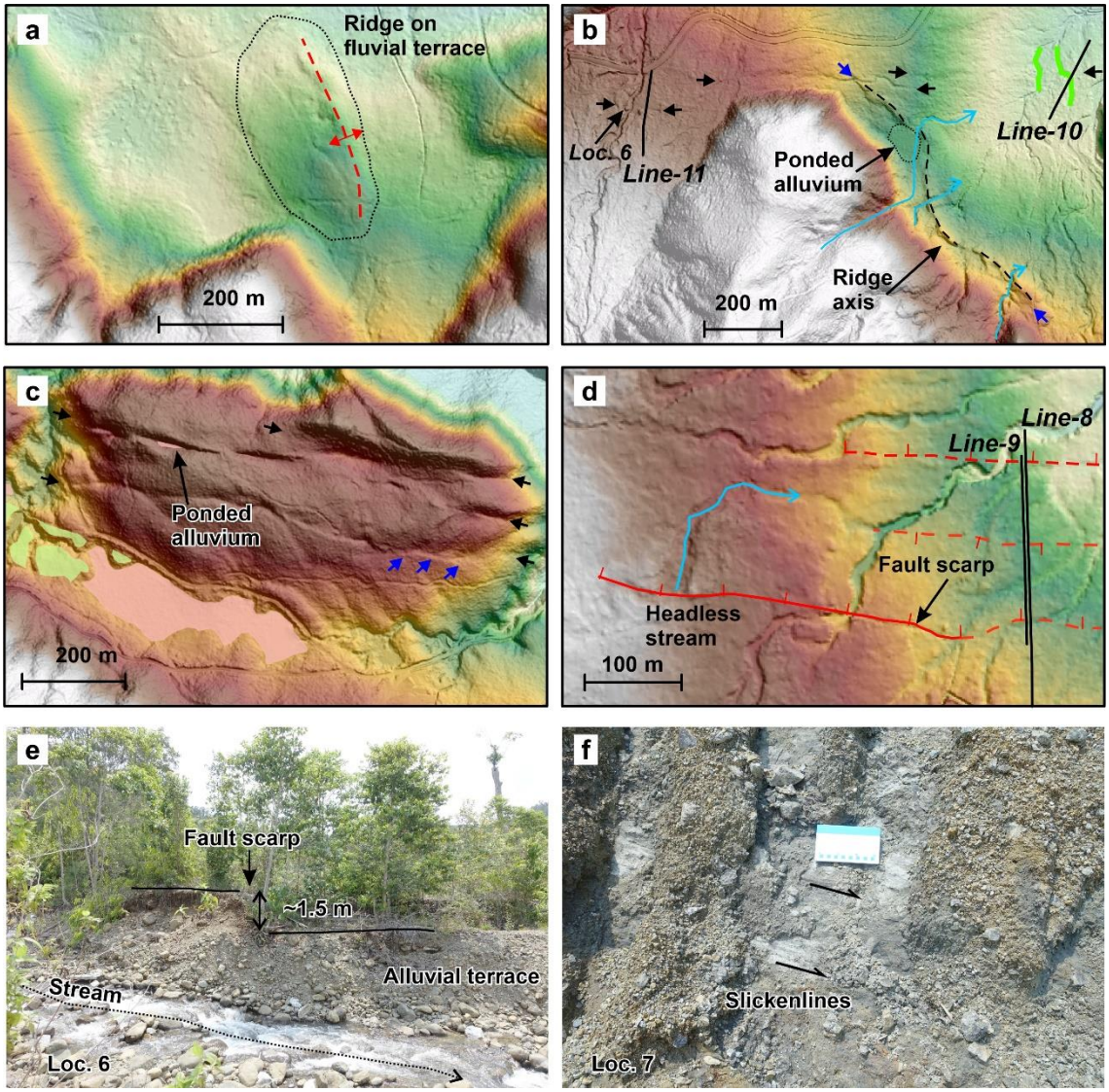

Figure 5.8 Typical geomorphic and geological features of the Balawai, Onepute, and Larongsangi segments. (a) Anticlinal ridge on the upper terrace. (b) East-west trending subtle lineaments (black arrows) represent the Balawai segment. Southeast striking ridges (blue arrows) on the alluvial terrace mark the Onepute segment. (c) Prominent lineaments (black arrows) associated with the depression in the mountainous terrain. *En-echelon* fractures (blue arrows) develop between the prominent lineaments. (d) Fault scarp associated with a headless stream. (e) 1.5-m high fault scarp on the alluvial terrace at location 6. (f) Slickenside on serpentinite at location 7.

Geomorphic expressions of the fault segment are less prominent at the DM 12–13 km, but the fault is evident at the subsurface. The ERT sections show that the Balawai segments consist of two fault traces, dipping steeply in opposite directions (Figure 5.9a–c). On the Line-6-ERT section,

the north-dipping fault trace is characterized by a displaced low resistivity layer at the HD 300 m, and the south-dipping fault at the HD 250 km is indicated by dip changes of shallow low resistivity layers (Figure 5.9a). Both fault traces extend to the surface. South of these faults, two other faults cutting high resistivity layer are interpreted as inactive since the flat low resistivity layer overlies them. The Line-7-ERT profile displays the conjugate faults of the Balawai segment (Figure 5.9b). The faults at the HD 670 and the HD 740 m displace all resistivity layers to the surface. The Line-8-ERT section shows similar features, suggesting that the Balawai segment continues westward. A deformed high resistivity layer marks the fault traces at the HD 440–495 m (Figure 5.9c). These two conjugate faults of the Balawai segment also appear on the Line-6-GPR at the HD 200–300 m and deform the uppermost 8 m reflectors (Figure 5.9e).

Between the DM 13 km and 15 km, the fault is indicated by east-trending subtle lineament on the alluvial terrace, in places associated with left-lateral river offset (Figure 5.8b). A 1.5 m high fault scarp cutting alluvial terrace at location 6 indicates the recent faulting activity (Figure 5.8e). To confirm the fault trace, two near-surface geophysical surveys were conducted. The Line-10-ERT profile shows that the segment is characterized by two oppositely dipping normal faults that merge into a single fault at depth (Figure 5.10a). The fault traces deform the high resistivity layer at the shallower part. The resistivity contrast at the HD 110 m, separating low and moderate resistivity, indicates the fault at the deeper portion. Two other faults are interpreted as inactive as they terminate just below the high resistivity layer at about 5 m depth. The Line-11-ERT section displays the segment as pop-up structures that uplift the high resistivity layer between the HD 50 m and 80 m (Figure 5.10b). The faults on the Line-11-ERT are correlated to the faults at the HD 50 m and 100 m on the Line-11-GPR section (Figure 5.10c). Some discontinuities were recognized on this GPR section from the HD 120 m southward. They do not have deeper continuation as no faults are observed on the ERT section at the southern portion, and these discontinuities are interpreted as shallow coseismic cracks.

From the DM 15 km westward, the Balawai segment traverses mountainous terrain until the DM 27 km (Figure 5.3b). Prominent lineaments and fault scarps mark this fault segment. Locally, fault traces are associated with ponded alluviums or tectonic depressions (Figure 5.8c). Two river offsets suggest a left-lateral displacement of about 1 km (Figure 5.3b). At the western termination, a pressure ridge develops as the fault steps to the right. A fault exposure on a cliff at location 7 shows a primarily left-lateral motion (Figure 5.8f).

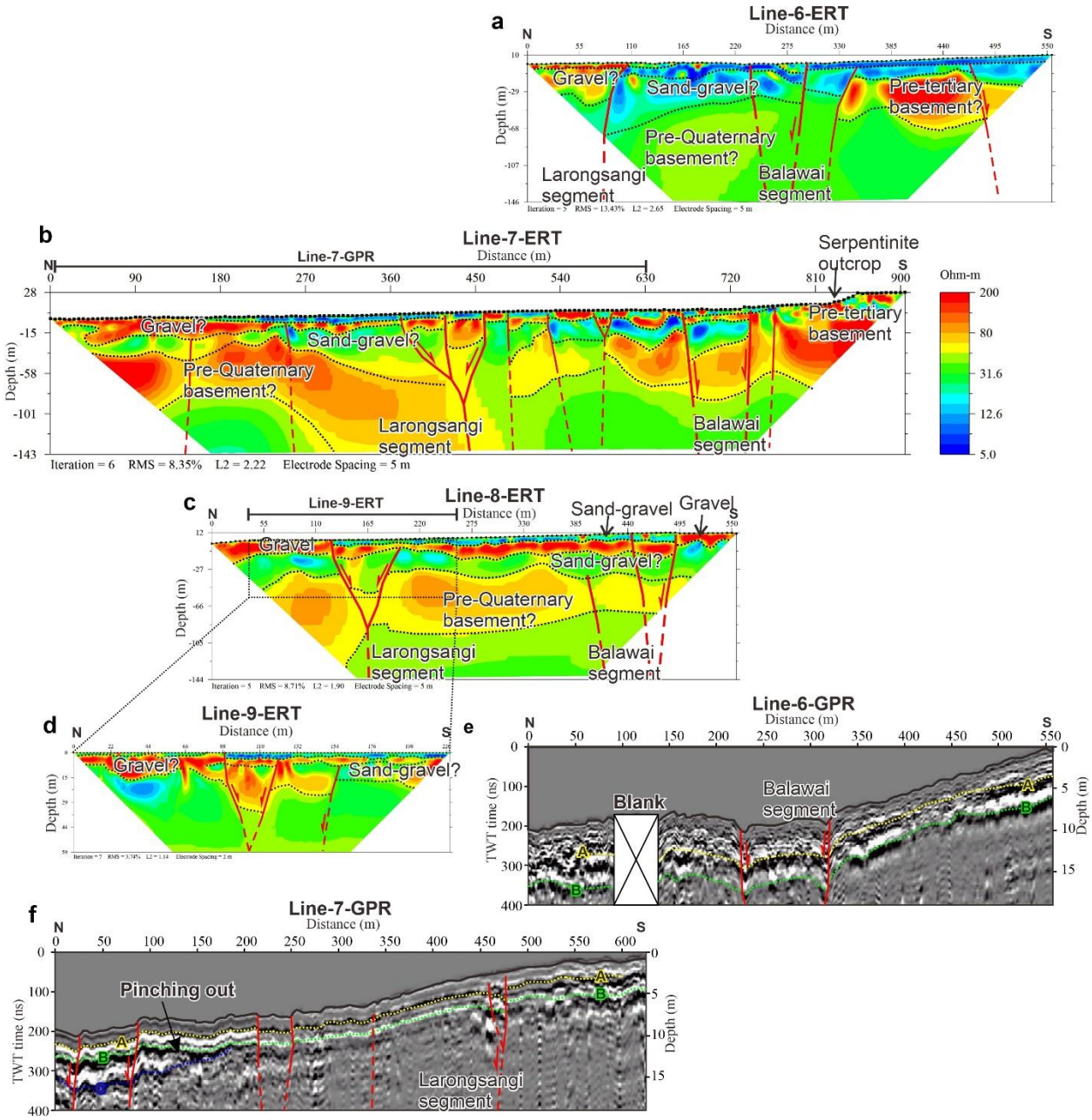

Figure 5.9 Interpretation of the Line-6–9-ERT (a–d) and Line-6–7-GPR sections (e–f). The Line-9-ERT section is a detailed measurement along the northern portion of the Line-8-ERT.

5.3.3 Larongsangi segment

The 3.5-km long Larongsangi segment is in the narrow basin between the Geresa and Balawai segments (Figure 5.3a). This segment branches into two strands further west. A 1-m high north-facing fault scarp associated with the beheaded channel characterizes the southern strand's western termination.

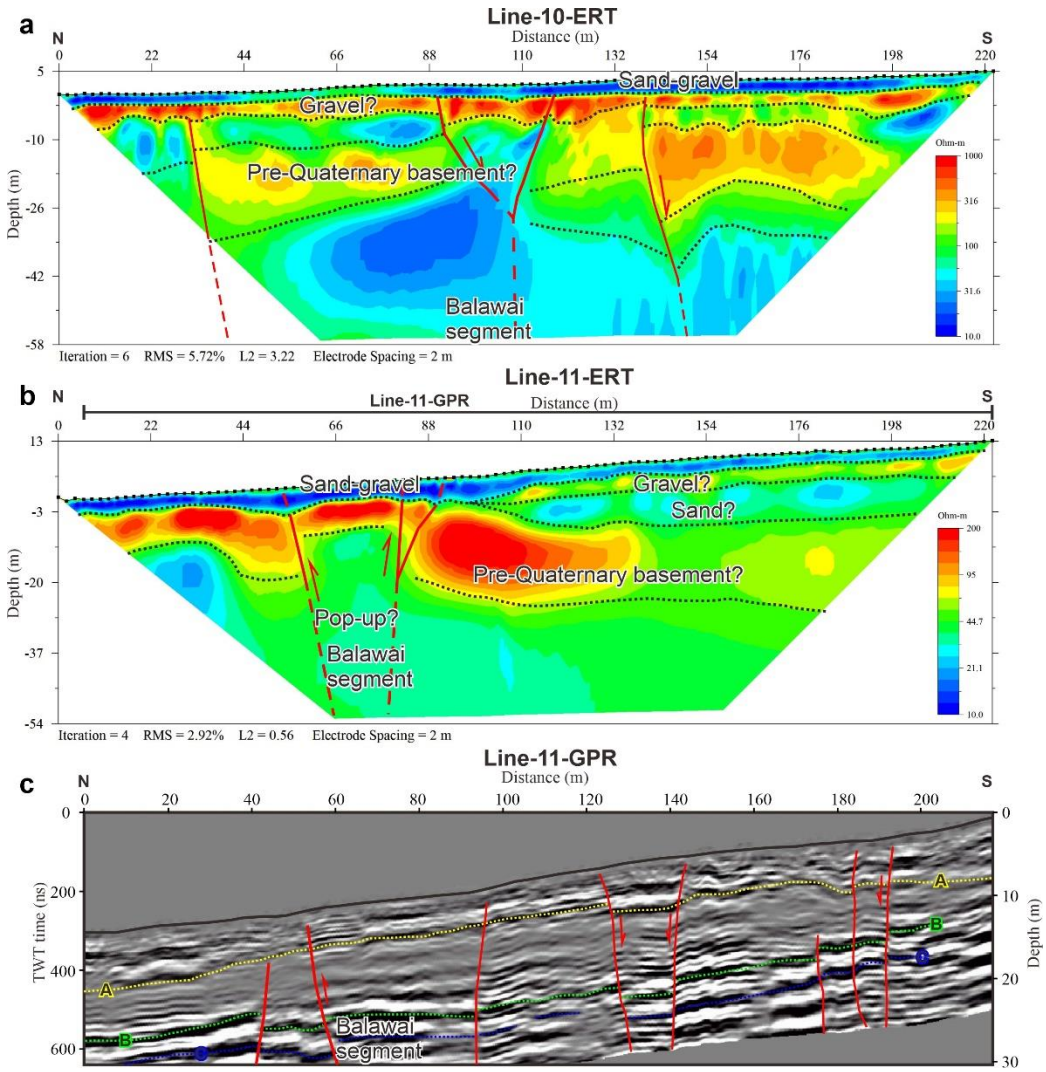

Figure 5.10 Interpretation of the Line-10–11-ERT (a–b) and Line-11-GPR sections (c).

The Larongsangi segment appears on the ERT and GPR profiles. On the Line-6-ERT section, this segment is observed as a resistivity contrast at about the HD 100 m (Figure 5.9a). The fault steeply dips to the north. Further west, on the Line-7-ERT profile, the graben structure between the HD 360 m and 450 m is interpreted as the Larongsangi segment (Figure 5.9b). This structure is characterized by the truncation of the high resistivity layers below the 60 m deep. On the Line-

8-ERT section between the HD 120 m and 200 m, a similar graben structure appears as two conjugate faults merging into a single fault at a deeper portion (Figure 5.9c). The structure deforms the shallow to deep resistivity layers. A more detailed measurement of the Line-9-ERT confirms the existence of these structures (Figure 5.9d).

5.3.4 Bahomoahi segment

South of the Geresa segment, the Bahomoahi segment is mainly east-west trending. It deviates northwestward at the western end and disappears at the coast at its eastern termination (Figure 5.3a). The total length of this segment is ~7 km. The south-facing fault scarps traverse the young alluvial plain, suggesting its recent activity. The scarps' heights are generally ~1 m.

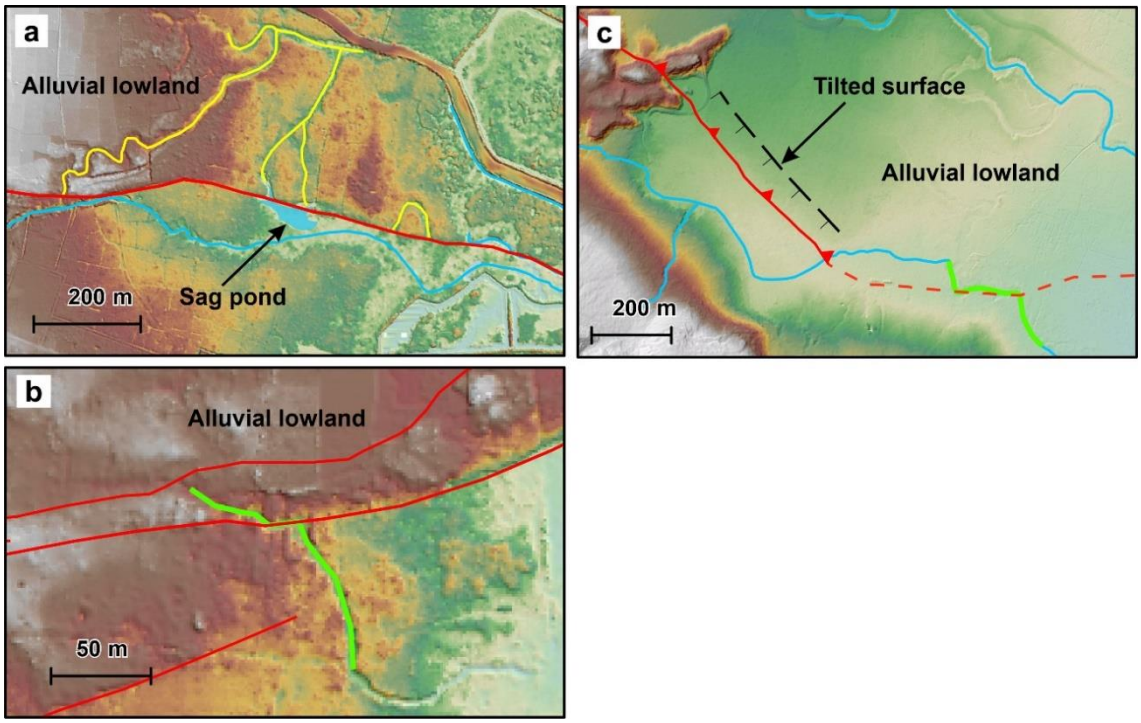

Figure 5.11 Typical geomorphic features of the Bahomoahi segment. (a) Faulted abandoned rivers to the north of the fault and a sag pond to the south. (b) 14-m left-lateral river offset associated with the 0.6-m high fault scarp. (c) Tilted surface at the restraining fault bend.

In addition, several north-facing and south-facing fault scarps are identified on the alluvial plain south of Bahomoahi. Between the DM 3 km and 4 km, the fault cuts several abandoned rivers to the north and forms a sag pond to the south (Figure 5.11a). About 15 m left-lateral river offset and a 1-m high fault scarp at the DM 5 km pronounce that this segment's vertical to horizontal

displacement ratio is about 7% (Figure 5.11b). Further west, two river offsets locate the fault trace before the segment bends. A tilted alluvial plain at the restraining bend indicates reverse faulting (Figure 5.11c).

The Line-12-ERT section crosses the fault scarp at about the DM 5 km. The ERT section shows the fault at the HD 133 m as gently deformed resistivity layers down to the south (Figure 5.12a). The high resistivity layer, interpreted as gravel, indicates a vertical displacement down to the south. The uppermost high resistivity layer at the HD 138–260 m truncates the deeper layer near the main fault. Two other faults are identified at the HD 83 km and 110 km on this ERT section, slightly deforming the deeper high resistivity layer. The Line-12-GPR profile covers some portion of the Line-12-ERT section line. On the GPR section, the main fault at about the HD 120 m displaces four distinct reflectors (Figure 5.12b). The vertical displacements of the reflectors A and B are about 1 m, similar to the fault scarp's height. At depth, the reflectors C and D are offset by about 2 m. These suggest multiple earthquakes on this fault segment. There are several fault traces north of the main fault, but only two at the HD 80 and 110 m appear to cut the reflector A. These faults are interpreted as older coseismic ruptures or other obscured active fault traces within the fault zone.

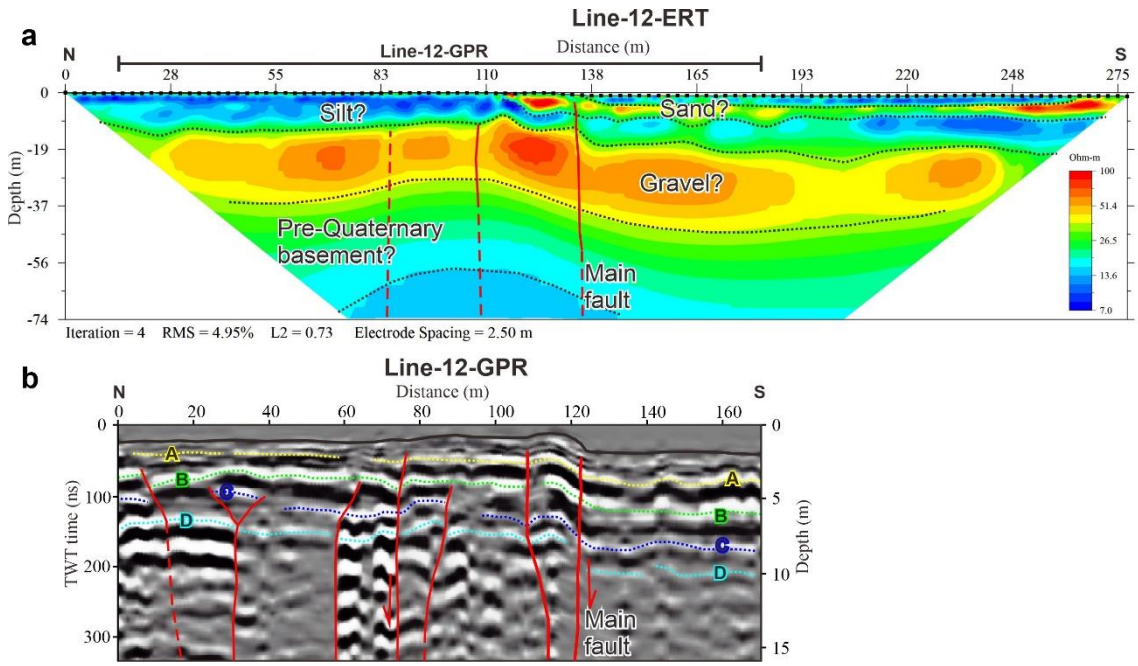

Figure 5.12 Interpretation of the Line-12-ERT (a) and Line-12-GPR sections (b).

5.3.5 Onepute segment

The Onepute segment traverses across mountainous terrain for about 15 km in length south of the Balawai segment (Figure 5.3a, c). It is oriented southeast, oblique to the Balawai segment. It terminates at the Balawai segment at its northern end, the DM 14 km. To the northwest, the segment is evidenced by the steep fault scarps separating the mountain from the river's valley (Figure 5.3a). Aligned wind gaps in the mountain to the west might be formed as uplifted abandoned rivers and indicate the vertical motion of the segment. Another fault trace deforms the alluvial terrace, forming aligned ridges (Figure 5.8b). A ponded alluvium might be formed due to the uplift of the ridges.

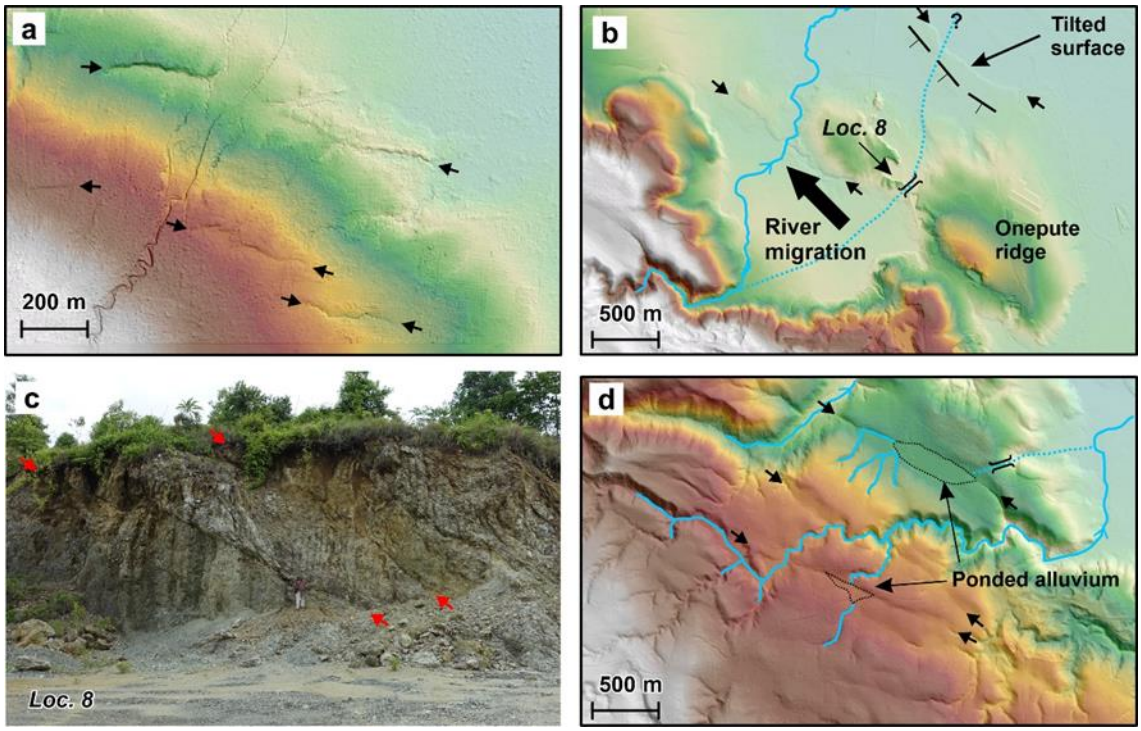

Figure 5.13 Typical geomorphic and geological features of the Onepute segment (a) Deformed surface at the distal of an alluvial fan. (b) Plausible river migration associated with the Onepute Ridge. (c) Fault exposure at location 8 with an attitude of N66°W, 42°SW. (d) Ponded alluviums associated with mountain-facing scarps on the mountainous terrain.

Several fault traces deform the alluvial lowland south of Bahomotefe (Figure 5.3c). Deformed distal alluvial fan southwest of Bahomotefe indicates the recent activity of this segment (Figure 5.13a). A wind gap at the Onepute Ridge might have resulted from the uplift of the former river, previously crossing the ridge (Figure 5.13b). This uplift also caused the formation of the

ponded alluvium and the migration of a former river to the northwest. Exposure in the ridge shows reverse faults, gently dipping to the southwest (Figure 5.13c). The Onepute Ridge might have developed in association with reverse faulting. To the north, a prominent tilted terrace associated with a fault scarp indicate recent faulting activity (Figure 5.13b).

In the mountainous terrain, uphill-facing scarps associated with ponded alluvium in some places mark the fault locations (Figure 5.3c). Several left-lateral river offsets are observed at the DM 9 km, suggesting that the segment may accommodate a part of the horizontal slip. A wind gap north of a ponded alluvium suggests that the river flowed across the fault, and then the valley has been uplifted due to the faulting activity (Figure 5.13d). There is another ponded alluvium to the south, bounded by a fault scarp.

5.4 Fault scarp analysis on the Geresa and Bahomoahi segments

The fault scarp heights of the Geresa and Bahomoahi segments were analyzed because they comprise continuous fresh scarps cutting young geomorphic surfaces. The fault scarp heights were extracted across prominent fault scarps using the LiDAR data (Figure 5.14).

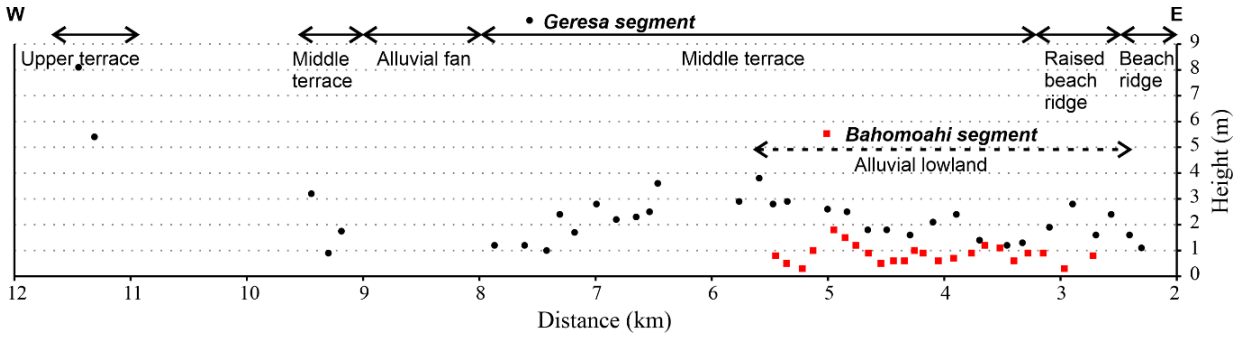

Figure 5.14 Distribution of the fault scarp height on the Geresa and Bahomoahi segments.

The Geresa segment has fault scarps cutting young geomorphic surfaces, such as beach ridges and alluvial terraces. The lowest scarp is 1 m high on the beach ridge. The fault scarps are on average 2.1 m high on the raised beach ridges, about twice on the beach ridge. The fault scarp cutting beach ridge represents a single surface-rupturing earthquake. Thus, the observed fault scarps on the raised beach ridge may account for two earthquakes. The fault scarps on the middle terrace are 1.2 m to 4 m high between the DM 3 km and 6 km, and the scarps' heights decrease to

about 1 m at the DM 8 km. These fault scarps likely record several surface faulting events. No fault scarp on the alluvial fan indicates that this surface remains undeformed. Further west, fault scarps on the upper terrace are about 6–8 m high and represent multiple earthquake movements.

The Bahomoahi segment's fault scarps are generally less than 1 m high on the alluvial plain. At about the DM 5 km, the height of the scarps becomes slightly higher, about 1.2–1.8 m. This increase corresponds to the releasing bend on this segment (Figure 5.3a). The Bahomoahi segment's scarps are lower than the Geresa segment's scarps. These low scarps are interpreted as due to a single surface-rupturing earthquake.

5.5 Paleoseismic analysis on the Geresa segment in Ululere

5.5.1 Geomorphic setting

In Ululere, the fault scarp separates the middle and lower fluvial terraces down to the south (Figure 5.15). The east-trending fault scarp extends for about 700 m from Ululere to the west before it disappears on the Ululere alluvial fan surface. West of the alluvial fan, the fault scarp exists again with a similar height to the scarp in Ululere. As previously suggested that the fault scarp in Ululure may record multiple surface faulting events, and this fault scarp is suitable for paleoseismic trench excavation.

The topographic profiles (x–x') along the geomorphic surface shows that the alluvial fan surface is 8–10 m higher than the middle fluvial terrace (Figure 5.15c). This indicates that the alluvial fan has developed after the faulting event that cut the middle fluvial terrace. The absence of fault scarp on the alluvial fan surface indicates that this surface remains undeformed. Thus, the age of this surface serves as the upper limit of the last surface faulting event. The alluvial fan deposit is exposed at location UL-05. The fan deposit was dominated by gravel with intercalation of a sand layer (Figure 5.16). Clasts were limestone from the Tokala Formation. To determine the age of this surface, a wood sample was collected from the sand layer at ~1 m below the ground (Figure 5.16). The sample from this surface was dated AD 1696–1724 or AD 1809–1947 (Table 5.1).

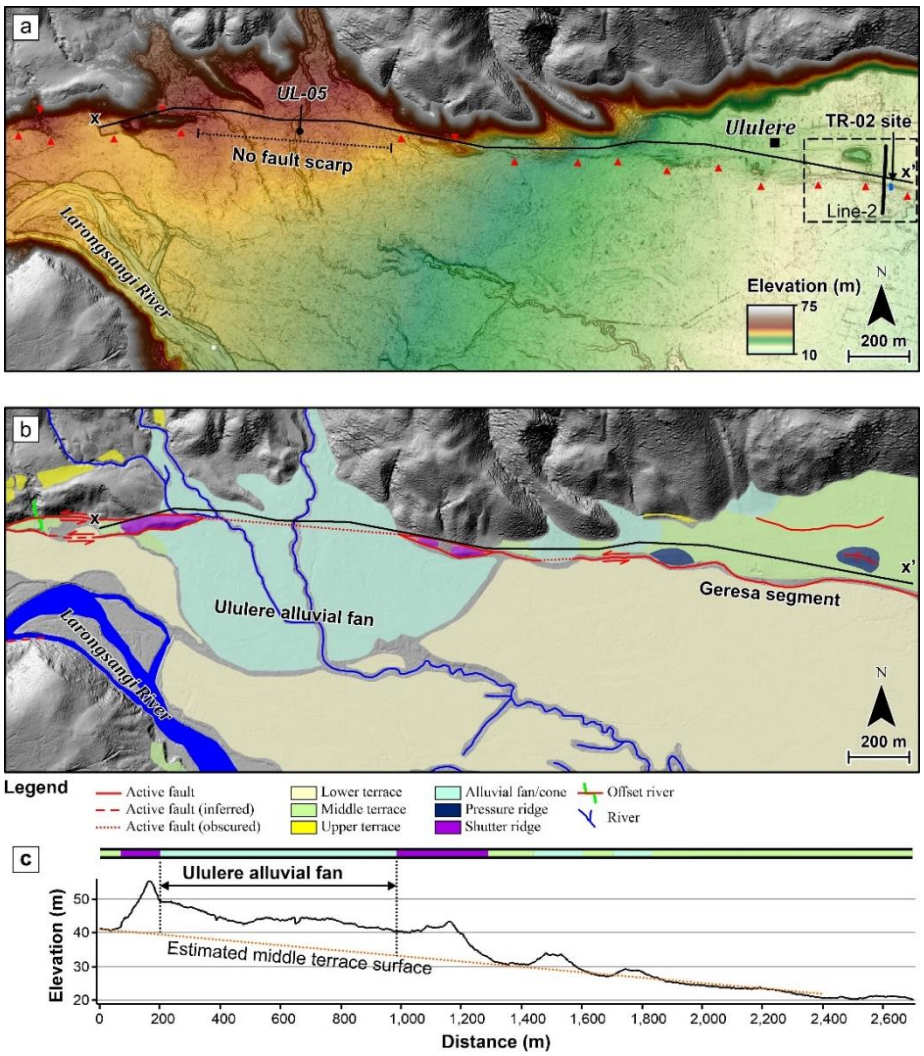

Figure 5.15 (a and b) DEM and tectonic geomorphic features of Ululere and nearby areas. Red triangles indicate fault scarps. See Figure 5.2 for location reference. (c) Topographic profile along the x-x' line.

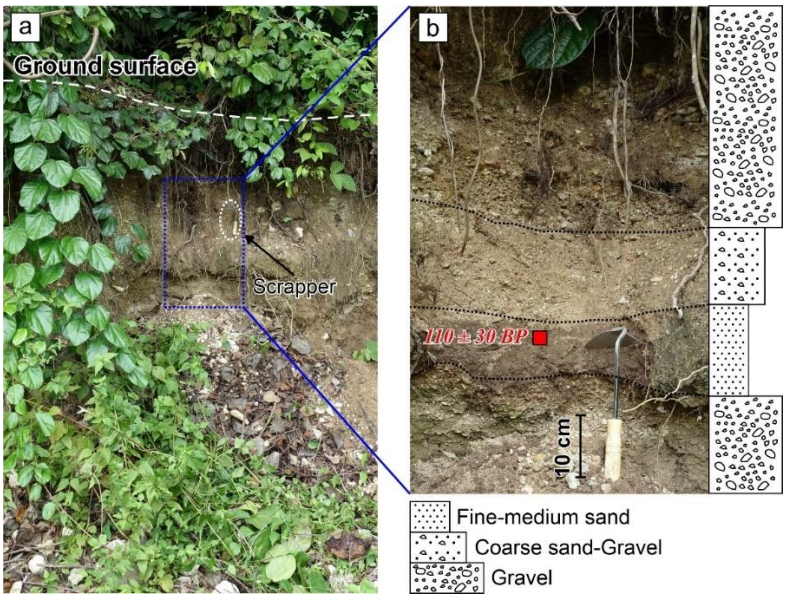

Figure 5.16 (a) Alluvial fan deposit at location UL-05. (b) Stratigraphic column of the fan deposit, and the wood was sampled from the sand horizon.

Table 5.1 Radiocarbon ages of samples from the alluvial fan and paleoseismic trench.

Loc.	Sample No.	Lab. No (Beta-)	Strat. Unit	Material	Measured ^{14}C age (yBP)*	δ13C (‰)	Conventional ^{14}C age (yBP)*	Calendar age (2σ)
UL-05	UL-05B	593057	Sand layer	Wood	160 ± 30	-28.2	110 ± 30	AD 1696–1724, AD 1809–1947
Ululere trench	TR02-01	592143	10	Organic sediment	103.78 ± 0.39 pMC	-22.1	103.16 ± 0.39 pMC	Post 1950
	TR02-02	592144	20	Organic sediment	380 ± 30	-16.7	520 ± 30	AD 1406–1455
	TR02-03	592145	31	Organic sediment	580 ± 30	-17.8	700 ± 30	AD 1284–1327, AD 1340–1392
	TR02-06	592146	40	Organic sediment	360 ± 30	-20.0	440 ± 30	AD 1439–1510, AD 1550–1558, AD 1580–1622
	TR02-07	592147	50	Organic sediment	970 ± 30	-19.8	1060 ± 30	AD 988–1050, AD 1082–1146

*or Percent Modern Carbon (pMC)

5.5.2 Stratigraphy and faults of the paleoseismic trench

The paleoseismic trench TR-02 was excavated in Ululure on the fault scarp (Figure 5.17a). The fault scarp is about 2 m high. The trench was excavated in March 2021 and located immediately west of the Line-2 (Figure 5.17b). The trench was oriented north-south crossing the fault trace and sized 13 m long, 1 m wide, and up to 3 m deep (Figure 5.17c). The trench walls were steep, about 80°. The excavation was completed until reaching the water table. The west and east walls were grided for the reference system. Both walls were logged by recording the stratigraphic units and faults. Organic sediment samples were taken for the AMS radiocarbon dating and the results are shown in Table 5.1.

The middle terrace deposits and two faults were exposed on the trench walls (Figure 5.18). The fluvial deposits were predominantly gravel and sand. Clasts in the deposits were mostly serpentinite, originating from the ophiolite complex. Table 5.2 lists the description of the stratigraphic units observed in the trench. Two faults, F1 and F2, show the vertical motion, down to the south, consistent with the south-facing fault scarp. The faults appear vertical and steeply dipping to the north.

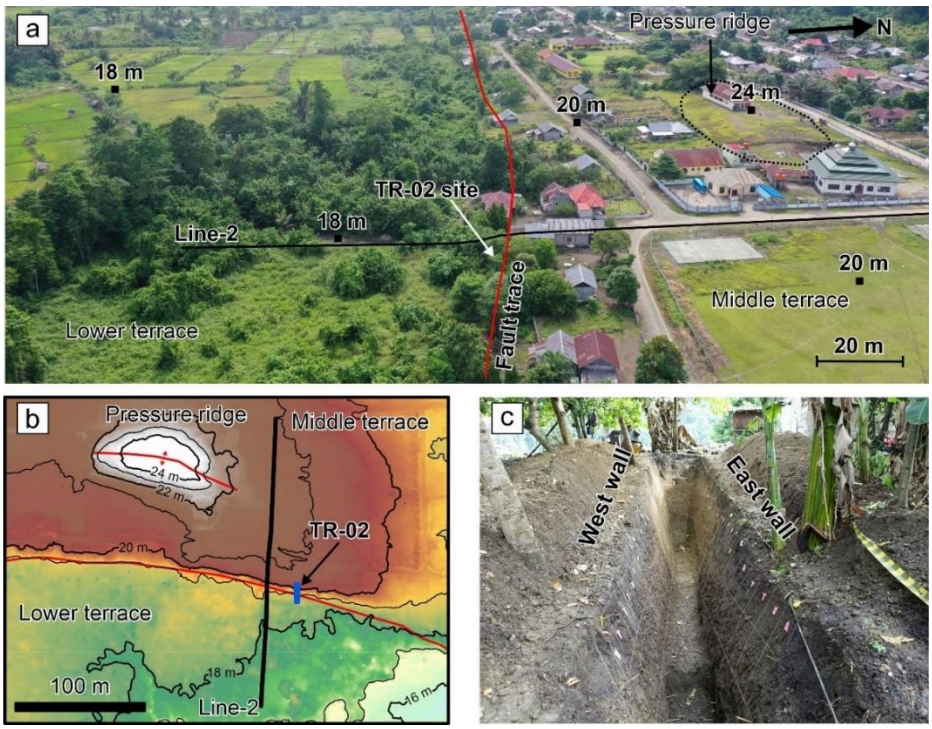

Figure 5.17 (a) Oblique view of Ululere village with elevation marks from the LiDAR data. (b) Topographic map of the trench site, based on the LiDAR data. (c) Photograph of the trench dimension.

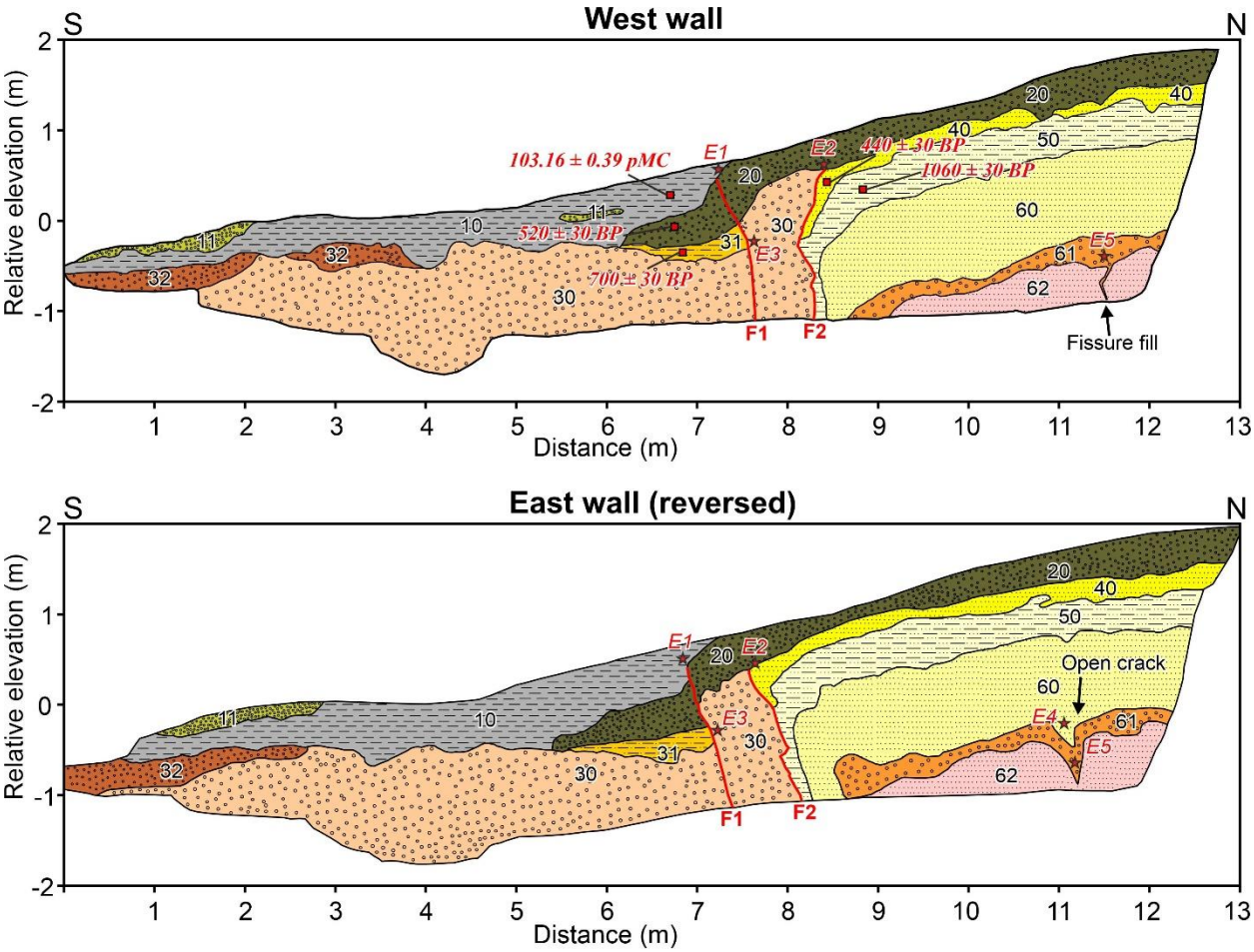

Figure 5.18 Log of the west and east walls of the paleoseismic trench TR-02.

Table 5.2 Description of the stratigraphic units on the paleoseismic trench TR-02.

Unit	Description
Unit 10	Blackish grey gravelly clay. Its color likely indicates high organic contents. This unit contains a few sparsely distributed sub-rounded to rounded pebbles and comprises gravel lenses of unit 11. This unit onlaps Unit 20 at the fault scarp. The sample from this unit were dated post-1950.
Unit 11	Sub-rounded to rounded pebble lenses within unit 10. This unit is clast supported deposit with clay to very fine sand matrix.
Unit 20	Dark grey gravel. This unit contains sub-rounded to rounded pebbles. A shell fragment was observed within this unit. This unit pinches immediately south of the fault. This unit is deformed by the fault. The sample from this unit was dated at 520 ± 30 yBP.
Unit 30	Greyish brown to dark-grey and grain-supported gravel. This unit contains sub-rounded to rounded pebbles. This unit truncates to the F1. Off the faults, the clasts are well oriented with a horizontal long axis while the clasts are skewed on the fault, indicating disruption due to faulting.
Unit 31	Yellowish-brown silty fine sand. This unit truncates to the F1 to the north and pinches to the south. This unit is interpreted as a colluvial wedge, likely originating from unit 50 based on the similarity. The sample from this unit was dated at 700 ± 30 yBP.
Unit 32	Blackish grey clast-supported gravel with sub-rounded to rounded pebbles. This unit appeared on the southern portion of the trench walls.
Unit 40	Blackish to brownish-grey deposits with medium sand to granule. The upper surface of this unit was eroded by unit 20. This unit truncates to and drastically plunges at the F2. The sample from this unit was dated at 440 ± 30 yBP.
Unit 50	Light grey very fine sand. This unit is homogenous. This unit warps towards and becomes vertical at the F2. The sample from this unit was dated at 1160 ± 30 yBP.
Unit 60	Light yellowish and brownish brown layer with very fine to fine sand. This unit also slopes towards the F2 and plunges vertically near the F1.
Unit 61	Blackish brown matrix-supported gravel with granules and pebbles. This unit tilts toward the F2. A crack filled by unit 60 was observed on the west wall.
Unit 62	Dark yellowish-grey fine sand layer with fissure fill. The fissure is filled by unit 61.

5.5.3 Paleoseismic events

Evidence of the earthquakes includes upward termination of fault structures, open cracks, and fissure fill (Figure 5.18). Based on the stratigraphic relationship and fault structures, five earthquakes (E1–5) were documented on the trench log in which three of them (E1–3) ruptured the surface. Two other earthquakes (E4, 5) are undetermined whether they displaced the surface or not.

Event 1 (E1): The most recent surface rupturing earthquake occurred after the deposition of unit 20 and before the deposition of unit 10. Unit 20 is offset by the F1 and the fault terminates below unit 10. The northern portion of unit 10 partly overlies the southern part of unit 20. The vertical displacement due to this earthquake is about 40–45 cm based on the offset of the lower boundary of unit 20 on both walls.

Event 2 (E2): The penultimate earthquake happened after the deposition of unit 40 and before the deposition of unit 20. The F2 separates the stratigraphic units north of the F2 with unit 30. The F2 terminates at the lower boundary of unit 20.

Event 3 (E3): The anti-penultimate event is constrained sometime between the deposition of unit 30 and unit 31. The wedge geometry and toward-fault truncation of unit 31 suggest that this unit is a colluvial deposit developed after a seismic event.

Event 4 (E4): This earthquake is indicated by an open crack on unit 61, filled by unit 60, observed on the east wall. The timing of this earthquake is not well constrained because the age of both units is not available.

Event 5 (E5): This event is marked by a fissure fill on unit 62, filled by unit 61, shown on the west wall.

To constrain the timing of the earthquake, the paleoseismic history was modeled using OxCal 4.4 program (Figure 5.19) (Bronk Ramsey, 2009). Table 5.3 shows the timing of the paleoseismic events based on the event modeling. The most-recent surface faulting event predates the age of the Ululere alluvial fan surface because this fan surface remains undeformed. The earthquake record from National Geophysical Data Center (NGDC) (2022) indicates that the earliest seismic event in eastern Indonesia was in AD 1629. No report about large seismic events on the Matano fault, suggests that the Matano fault has not ruptured at least since the 17th century. However, there is still a possibility that the Matano fault had ruptured between AD 1629 and AD 1900 (initial time of instrumental record for seismic), but the event was not documented.

A recent archeological investigation by (Adhityatama et al., 2022) revealed that an iron production settlement dated in the 8th century on Lake Matano had submerged 3–15 m below the current water line. It was postulated that large earthquakes might be the cause of the disappearance of this settlement. Although it is not possible to directly account for the earthquakes observed on the paleoseismic trench to this submerged site, one of these earthquakes might be the cause of this settlement extinction.

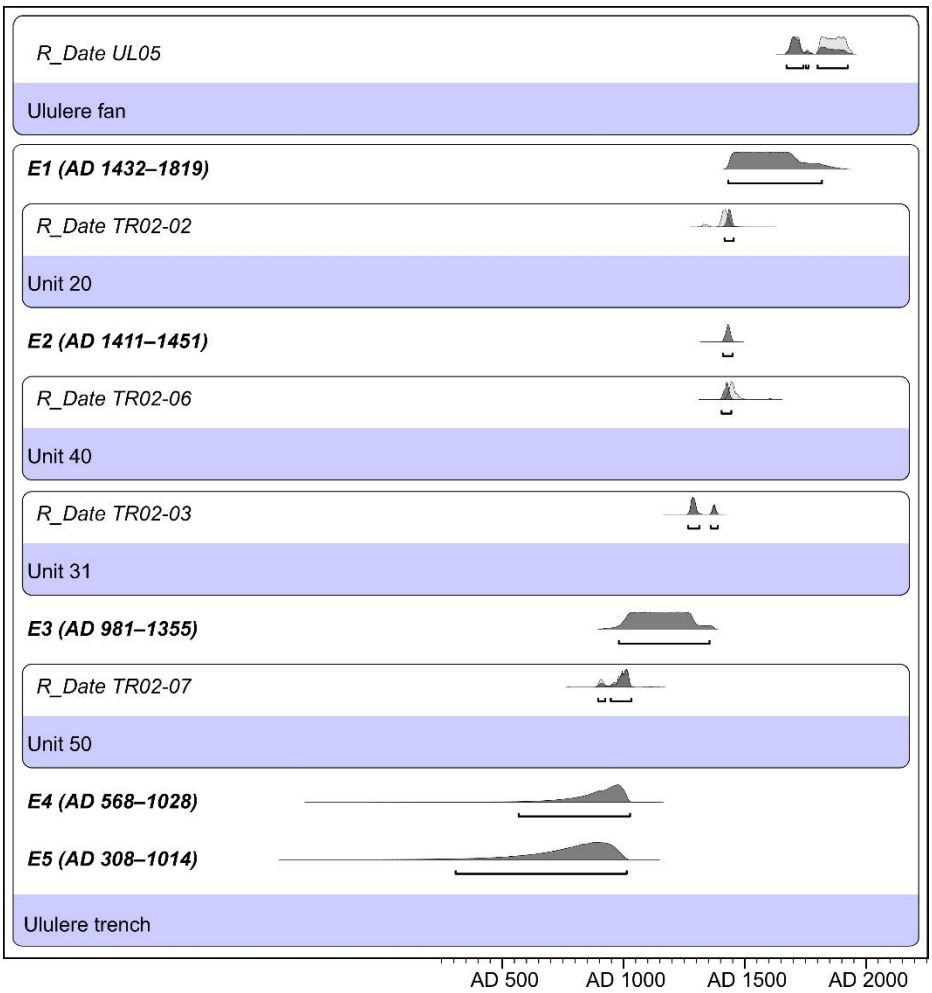

Figure 5.19 The OxCal modeling of the paleoseismic events on the Geresa segment based on observation of the paleoseismic trench. The age of the Ululere alluvial fan is included in this modeling as the upper boundary.

Table 5.3 Timing of paleoseismic events on based on the OxCal modeling.

Event	From (AD)	To (AD)	Median date (AD)
E1	1432	1819	1626
E2	1411	1451	1431
E3	981	1355	1168
E4	568	1028	798
E5	308	1014	661

Note: Recurrence interval is calculated using the age model of E1 to E3 only.

5.6 Structures of the easternmost Matano fault

Geomorphic observations indicate that the fault is prominent and traverses the Larongsangi basin and mountainous terrains (Figure 5.20). However, the primary fault traces often appear associated with some minor subsurface faults. Although the minor fault traces displace shallow

sedimentary layers, they mostly do not have evident surface expressions. The eastern Matano fault is interpreted to behave as a wide shear/fault zone rather than a single fault line.

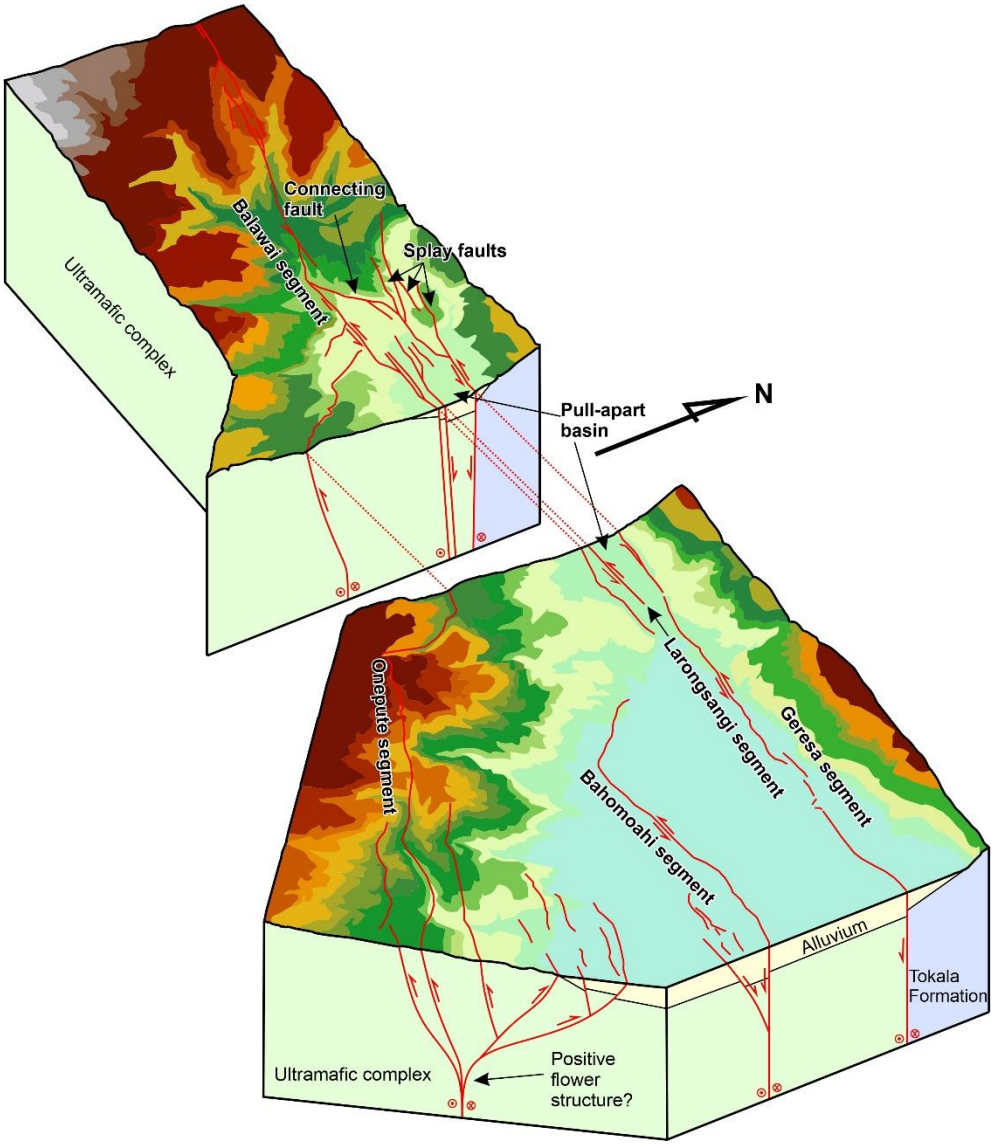

Figure 5.20 3D geological model of active faults. The subsurface geological units are adapted from Simandjuntak et al. (1993).

The Geresa segment steps to the Balawai segment and these two segments form a narrow pull-apart basin (Figure 5.20). Two subsidence centers tend to develop at a narrow releasing step-over where the separation is significantly less than the overlapping distance (Deng et al., 1986). A detailed analysis of the drainage patterns at the narrow basin indicates two tilting directions within the basin (Figure 5.21). Rivers located at the western portion flow toward the northeast, whereas

those in the eastern part flow towards the southeast. Therefore, the flow directions of the drainage system may represent the two subsidence centers.

The Larongsangi segment is an intra-basin strike-slip fault that may connect the left-lateral slip between the Geresa and Balawai segments (Figure 5.20). South of the Geresa segment, the Bahomoahi segment is also a left-lateral strike-slip fault crossing the Larongsangi basin. This segment deviates northwestward and forms a restraining bend as it approaches the mountain. The Onepute segment forms a restraining bend that translates the left-lateral motion into a reverse motion (Figure 5.20). It consists of oppositely dipping reverse faults as a positive flower structure. Since the eastern fault traces deforms young geomorphic surfaces, the eastern portion mainly accommodates the fault motion. The faulting activity of this segment might have migrated eastward.

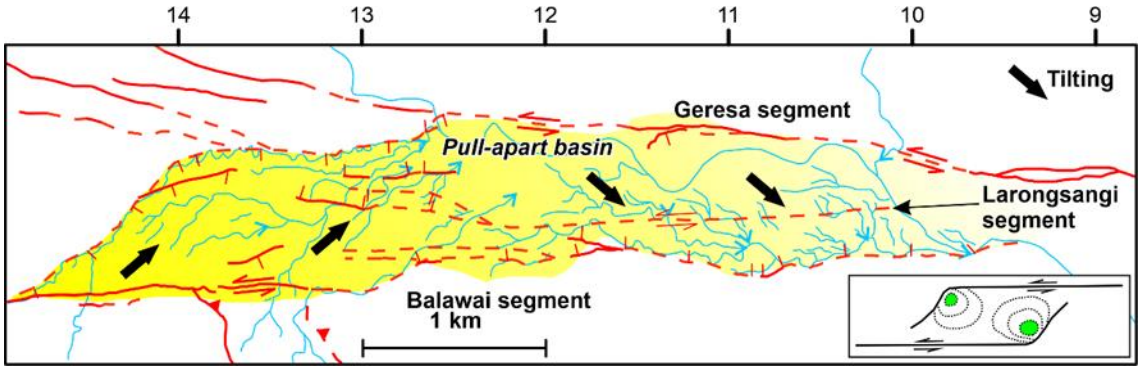

Figure 5.21 Drainage pattern of the narrow basin at the overlapping and overstepping zone of the Geresa and Balawai segments. Inset is a model of a pull-apart basin at step-over where the overlap separation is smaller than overlap (Deng et al., 1986). Green polygons mark the subsidence centers.

Detailed bathymetry interpretation from Titu-Eki and Hall (2020) shows several faults in the Tolo complex, an offshore area between the South Sula fault and the Matano fault (Figure 5.22). To make it clear, names were assigned to these faults as the F1–F4 fault. Titu-Eki and Hall (2020) argue the possible linkage between the Matano fault and the Tolo thrust via the F4 fault. However, the Matano fault appears to connect to the South Sula fault because the Geresa and Bahomoahi segments are east-west trending and terminate at the coast. Therefore, both segments may continue offshore and connect to the F2 fault east of the study area. The linkage possibly includes the F3

fault and propagates to the South Sula fault. There is a left-lateral bathymetric offset of about 5 km on the F3 fault. This connection implies that the Matano fault accommodates the left-lateral motion from the South Sula fault and translates the Tolo thrust's convergence to the left-lateral slip.

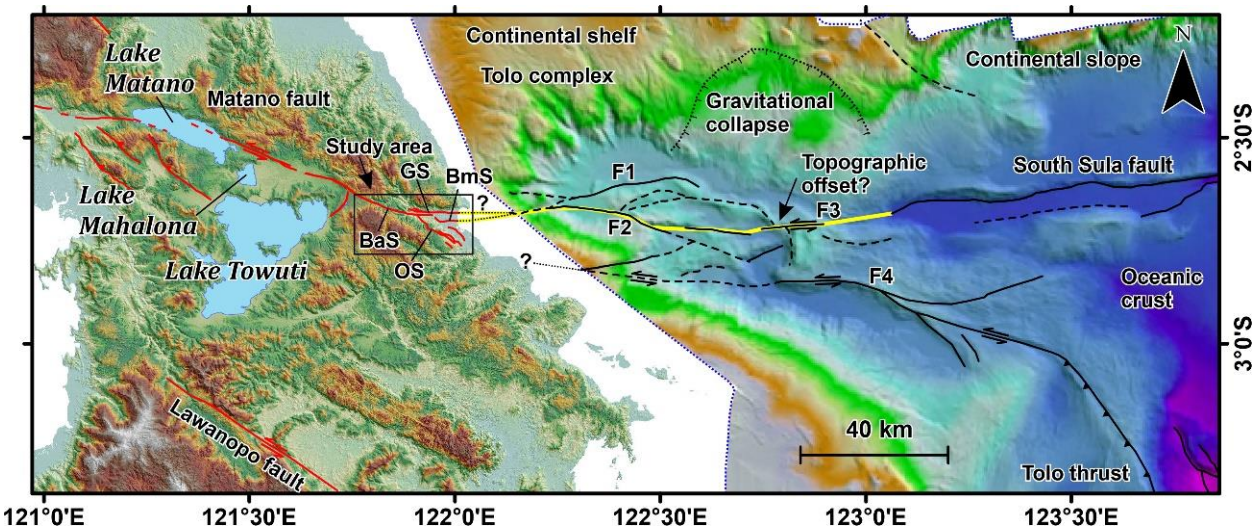

Figure 5.22 Proposed relationship between onshore and offshore structures. BaS: Balawai segment, BmS: Bahomoahi segment, GS: Geresa segment, OS: Onepute segment. Offshore structures and multibeam bathymetry are from Titu-Eki and Hall (2020). The onshore active faults outside the study area are from National Center of Earthquake Study (PUSGEN) (2017).

5.7 Magnitude and extent of the most-recent surface-rupturing earthquake

The ~7 m left-lateral offset of the beach ridge and ~1 m high fault scarp at location 1 are interpreted as a result of the most recent surface-rupturing earthquake in AD 1432–1819, recorded on the paleoseismic trench. The horizontal offset appears to be maximum earthquake displacement and is comparable to the 2018 M_w 7.5 Palu earthquake's maximum left-lateral slip of 6 m. Using a scaling relation by Wells and Coppersmith (1994), the ~7 m maximum displacement yields a probable magnitude M_w of 7.4 ± 0.3 and a probable rupture length of 107 ± 2 km for the most recent surface-rupturing earthquake.

Based on observation of strike-slip fault earthquakes in the world, Wesnousky (2006) suggested that ≥4 km wide stepover might be a barrier to earthquake rupture propagation. Along the Matano fault, Lake Matano marks the only ~6 km wide releasing stepover separating the

Matano and Pamsoa segments (Figure 5.22), and it may act as an earthquake barrier. So, Lake Matano might be the western termination of the most recent surface-rupturing earthquake. However, the distance between Lake Matano and the study area, about 85 km, is less than the calculated probable rupture length for the most recent surface-rupturing earthquake. Thus, the eastern end of the most recent earthquake rupture might be located offshore at least 20 km eest of Kolono Bay. The Geresa segment is likely to continue further east offshore because it disappears at the Kolono Beach.

5.8 Recurrence interval and slip rate

Based on the paleoseismic events modeling, the average recurrence intervals between events 1 and 2, and events 2 and 3 are estimated at 195 and 263 years, respectively. Rounding this value yields an average recurrence interval of the surface-rupturing earthquake of 190–270 years or 230 ± 40 years. This recurrence interval is longer than the Palu-Koro fault, ~110 years (Daryono and Natawidjaja, 2019). Using a coseismic slip of 7 ± 1.4 m based on the offset ridge at location 1 and the average recurrence interval, the slip rate is estimated at 30 ± 7 mm/yr. This slip rate is comparable to the maximum geodetic slip rate of 28 mm/yr, calculated by Khairi et al. (2020) and higher than the geodetic slip rate of 20 mm/yr, modeled by Walpersdorf et al. (1998a) for the Matano fault. The Matano fault is concluded to move slower than the Palu Koro fault which slips at 35–40 mm/yr (e.g., Bellier et al., 2001; Socquet et al., 2006; Walpersdorf et al., 1998b). The slower slip rate of the Matano fault corresponds to the longer large earthquake recurrence interval, compared to the Palu-Koro fault.

5.9 Potential seismic hazards

This study has uncovered the timing and magnitude of the most-recent surface-rupturing earthquake on the eastern Matano fault. At least 200 years have already passed since the last surface faulting event, exceeding the shortest estimated recurrence interval of 190 years. Hence, the next surface rupturing earthquake is already due for the eastern portion of the Matano fault. The future surface-rupturing earthquake may be similar to the postulated scenario for the last

surface faulting event with a magnitude M_w of ~7.4. Moreover, it may carry a significant risk because the area around the easternmost Matano fault has been developed as a ferronickel industrial zone[1)]. A large earthquake may damage vulnerable sites such as mining sites, smelters, seaports, and power plants in this area.

Offshore fault ruptures and or seismic shaking could trigger a subaerial and submarine landslides tsunami, like the 2018 Palu earthquake case. There is ~40 km wide gravitational collapse at the bathymetric slope east of the study area (Titu-Eki and Hall, 2020). Such a submarine landslide could occur during a large earthquake and would generate a tsunami along the eastern coast of Sulawesi. Additionally, another potential hazard related to earthquakes is liquefaction which could be caused by strong shaking on saturated sand layers (e.g., Castilla and Audemard, 2007). ERT sections show the evidence of sand boiling at the Ululere ridge (Figure 5.6). During the paleoseismology excavation in Ululere between March and April 2021, sand is dominant at the subsurface, and the water table is shallow at about 1–3 m deep. The shallow water table (<10 m deep) is one of the favorable conditions for liquefaction during earthquakes (Youd and Hoose, 1977).

[1] (https://kppip.go.id/en/national-strategic-projects/s-priority-industry-zone-development-special-economic-zone/morowali-industrial-zone-central-sulawesi/

Chapter 6

Active faults system in the northern Banda Arc

6.1 Overview

The Banda Arc is a prominent tectonic feature in eastern Indonesia, which curves 180° enclosing the Banda Sea (Figure 6.1a). The northern Banda Arc currently converges with the Bird's Head of Papua (e.g., Bock et al., 2003; Stevens et al., 2002). Based on seismicity analysis, McCaffrey (1988) suggested the interplay of thrust and strike-slip faulting in accommodating the convergence. Historical records show that significant earthquakes have occurred in the northern Banda Arc and mostly struck Ambon (Figure 6.1b). Watkinson and Hall (2017) mapped the Quaternary faults in eastern Indonesia. For the northern Banda Arc, they mainly used SRTM 90 m and ASTER 30 m to map major lineaments associated with fault traces but lacking recent faulting evidence. The National Center of Earthquake Study (PUSGEN) (2017) published an earthquake source and hazard map of Indonesia. However, details of the active fault traces and geomorphic evidence have not been discussed in detail. These data are essential in understanding the active tectonics and evaluating the potential seismic hazard in the northern Banda Arc.

The study in the northern Banda Arc intends to understand the active tectonics of the region by interpreting the tectonic geomorphology of Seram, Buru, Ambon, and surrounding islands. Active faults were mapped based on the interpretation of 3D anaglyph images together with shaded-relief, slope, and topographic maps. The active fault map is available in Appendix B. The focal mechanism solution of earthquakes between 1976–2015 from the Global Centroid-Moment-Tensor (CMT) (Ekström et al., 2012) catalog was plotted to show the possible earthquakes associated with active faults (Figure 6.1b). To better constrain the location of earthquake solutions, the Global CMT catalog is matched with the ISC-EHB catalog (Engdahl et al., 2020) based on event time similarity. Only earthquakes with a depth less than 20 km were analyzed because they are related to the upper crustal deformation.

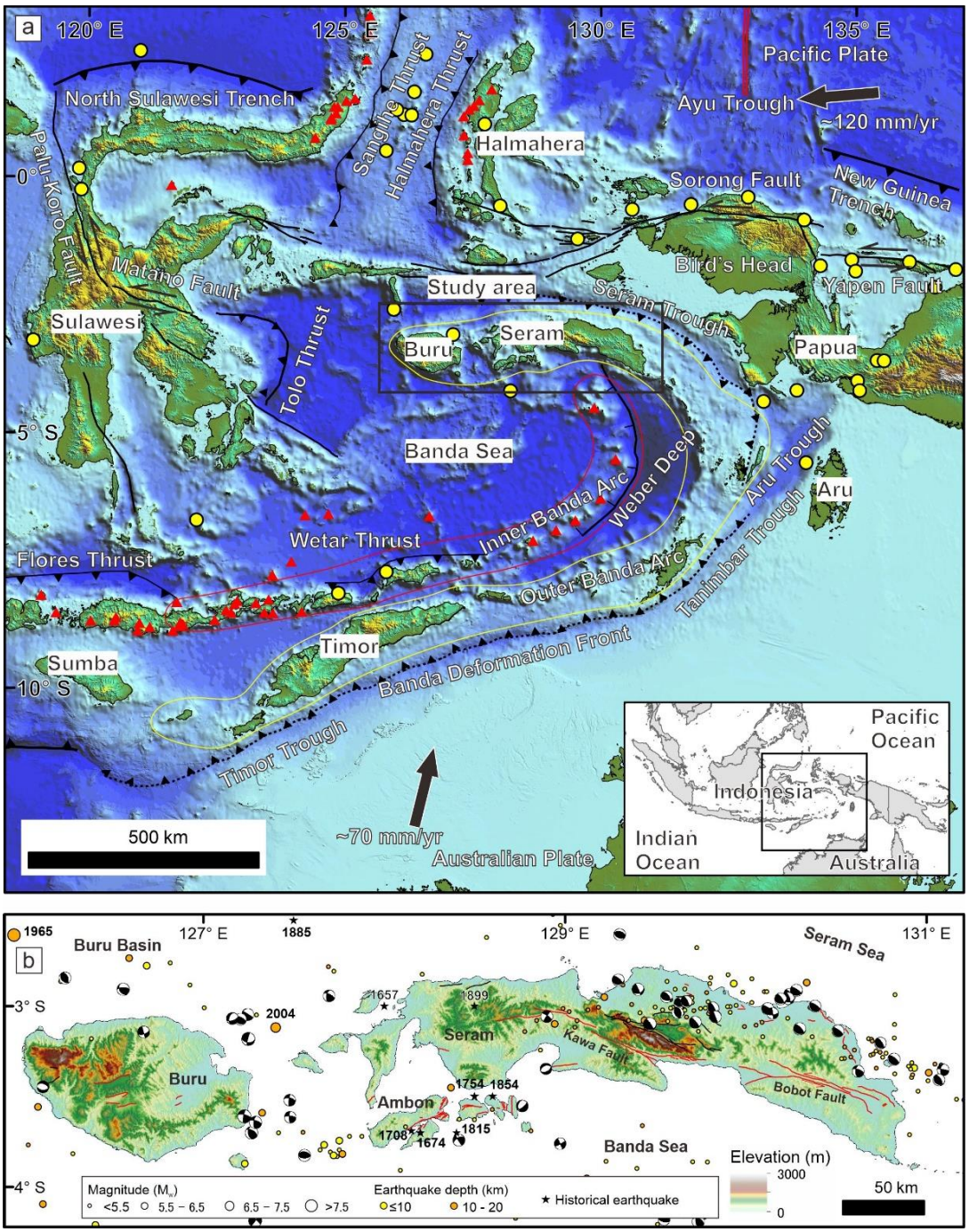

Figure 6.1 (a) Tectonic map of eastern Indonesia showing major structural elements (modified after Hall, 2012 and Pownall et al., 2016). Plate motion vectors relative to Eurasia are from DeMets et al. (2010). The red line marks the inner Banda Arc, and the yellow line marks the outer Banda Arc. Red triangles indicate volcanoes. Yellow circles mark the hypocenter of the modern earthquakes with a depth ≤ 20 km and $M_w \geq 7$ between 1910 and 2019 from the USGS global earthquakes catalog. (b). Simplified active fault map of the onshore northern Banda Arc with selected earthquake solutions with a depth ≤ 20 km and $M_w \geq 4.5$ between 1976 and 2015 from the Global CMT catalog. Circles indicate the hypocenter of the earthquakes with depth ≤ 20 km and $M_w \geq 4.5$ during 1950–2019 from the USGS earthquake catalog. Historical earthquakes before 1900 are from National Geophysical Data Center (NGDC) (2022). Red lines mark the active fault trace, and black lines indicate the presumed active fault trace.

Additionally, the Ambon fault was further investigated based on a detailed tectonic geomorphic analysis, and GPR survey to delineate accurate fault locations and subsurface continuations. Shallow manual boring was done to obtain representative samples of deformed geomorphic surfaces for radiocarbon dating.

The potential maximum earthquake magnitudes of each active fault were calculated using the scaling relationship between magnitude and surface rupture length, proposed by Wells and Coppersmith (1994). The results of active fault mapping were integrated with other published geological interpretations covering the surrounding offshore region (e.g., Baillie et al., 2019; Hall et al., 2017; Patria and Hall, 2017; Teas et al., 2009) to link the identified active faults with offshore structures. The geodetic velocity fields from Bock et al. (2003) were also analyzed to bring the results into regional tectonic kinematics.

6.2 Geomorphic observations on the onshore northern Banda Arc

In this section, the study area is divided into five based on the tectonic geomorphic features observed in each area (Figure 6.2).

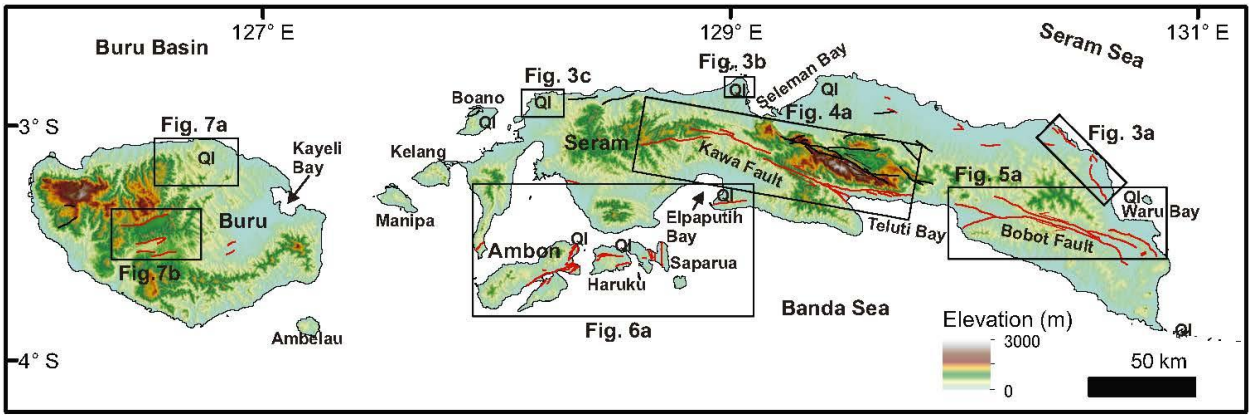

Figure 6.2 Division of the study area: North Seram (Figure 6.3a–c), Central Seram (Figure 6.4a), East Seram (Figure 6.5a), South Seram, and Ambon (Figure 6.6a), and Buru (Figure 6.7a, b). Ql marks the uplifted marine terraces.

6.2.1 North Seram

Topographically, Seram's northern coast can be divided into two areas, separated by Seleman Bay (Figure 6.2). The eastern portion of north Seram is characterized by broad lowlands

in the north of the central Seram mountains, while the western part has a narrow coastal area. The mountain fronts are highly sinuous. Although north Seram is known as the Seram fold-and-thrust belt, there is limited evidence of active faulting, such as in Bula (Figure 6.3a). Shallow seismicity in north Seram mainly shows thrust fault earthquake solutions (Figure 6.1).

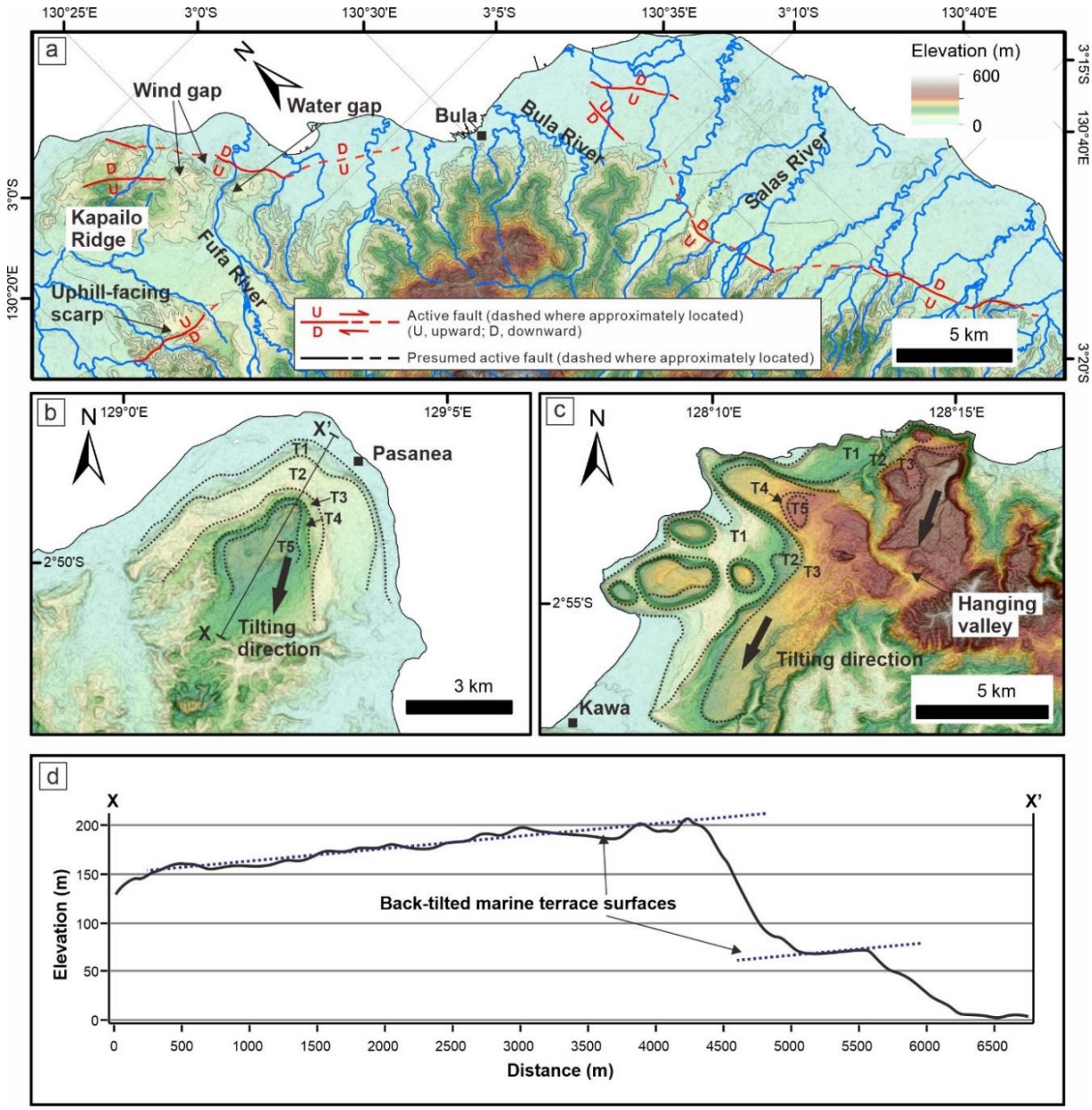

Figure 6.3 (a) Tectonic geomorphic features in Bula and surrounding areas. (b) Raised marine terraces in Pasanea back tilted toward the south. (c) Uplifted and back tilted marine terraces in Kawa. The terraces are associated with a hanging valley that is elevated at about 250 m a.s.l. Dotted black lines mark the terrace surface boundaries. (d) Topographic profile along tilted marine terraces in Pasanea.

Northwest of Bula, the southeast-trending Kapailo Ridge is cut by the Fufa River, forming a water gap (Figure 6.3a). The ridge is composed of limestone of the Pleistocene Fufa Formation

(Gafoer et al., 1993). Three wind gaps are located along the ridge crest west of the Fufa River and elevated 20–120 m, from east to west, above the Fufa River. These geomorphic features indicate that the Kapailo ridge has been uplifted while the Fufa River keeps down-cutting and flowing northward. A northeast-facing scarp bounds the ridge in the north, extends for 14 km, and terminates immediately before reaching Bula (Figure 6.3a). Another ~40-m-high uphill-facing scarp is identified south of the Kapailo Ridge, cutting a relatively flat surface. Some other 5–10 m high scarps can be observed south of Bula, deforming lowland surface and fluvial terraces.

Raised marine terraces are observed along the northern coast of Seram from the Boano to Waru Bays (Figure 6.2). The terraces are classified as late Pleistocene–Holocene age based on Gafoer et al. (1993) and Tjokrosapoetro et al. (1993c, 1993a). The terraces are relatively undeformed and consist of several surfaces. The maximum elevation of each terrace varies from 60 to 250 m. For example, marine terraces in Pasanea consist of 5 surfaces (Figure 6.3b). In two localities of Pasanea and Kawa, the terraces are back tilted towards the south-southwest (Figure 6.3b, c). A hanging valley is identified on the Kawa marine terraces at an elevation of ~130 m (Figure 6.3c). The existence of the marine terraces and hanging valley attests to the uplift in north Seram.

6.2.2 Central Seram

Central Seram is a mountainous area from the north of Elpaputih Bay to the north of Teluti Bay. The maximum elevation reaches 3000 m at Manusela Mountain. Two active faults are identified in this area, the Kawa and Manusela faults (Figure 6.4a). Most of the active fault traces traverse mountainous terrains.

6.2.2.1 Kawa Fault

The ~137-km-long Kawa fault mostly crosses the mountainous terrain from the north of the Elpaputih Bay to the north of the Teluti Bay (Figure 6.4a). The Kawa fault consists of four geometric segments, from east to west: the Teluti, Alau, Nakupia, and Mala segments. A 16 km deep strike-slip fault earthquake between Mala and Nakupia segment might be related to the Kawa

fault since its southeast nodal plane is concordant with the strike and slip sense of the Nakupia segment (Figure 6.4a).

Teluti segment. The southeast-trending Teluti segment extends along the southern foot of the Manusela Mountain north of the Teluti Bay (Figure 6.4a). Series of left-lateral offset rivers mark the location and slip sense of the segment (Figure 6.4b). About 5 km west of its eastern end, a restraining double bend is identified associated with an uplifted topography. South of the main fault trace, several shorter fault traces are identified as south-facing fault scarps and left-lateral river offsets.

North of Hatu and Teluti Baru, two beheaded rivers suggest ~1 km left-lateral displacement (Figure 6.4b). Between Yaputih and Piliana, a shutter ridge with a wind gap marks the largest left-lateral river offset of ~2 km. Another ridge also left-laterally deflects the Hatuputih River for about 700 m (Figure 6.4b). Another fault branch bounds the southwestern margin of the Kawa River's valley. There is no left-lateral offset associated with this strand. Further west, the fault is delineated by the narrow linear valley of the Kawa River (Figure 6.4a). Within the valley, hillside ridges mark the location of the fault trace. At the western end, the fault is marked by aligned saddles.

Alau segment. From the Teluti segment, the fault steps right for ~ 3 km to the Alau segment (Figure 6.4a). This segment traverses an intramountain depression for ~20 km (Figure 6.4c). A wind gap between the Alau and Teluti segments indicates that the Yua River might have previously flew southward through the Minim River. To the east, the fault follows the Yua River's linear valley, where the fault is marked by a southeast-trending trough that separates aligned ridges from the mountain slope south of the fault. Two river offsets of the Sunemaikuh and Alau Rivers suggest ~1 km left-lateral displacement. The western end of the segment is associated with hill-side ridges.

Nakupia segment. The Nakupia segment steps right for ~500 m from the Alau segment (Figure 6.4a). The fault segment bounds the southern edge of a ridge and then follows the Nakupia River (Figure 6.4e). The fault segment extends in an east-southeast direction for ~20 km with several left-lateral offset rivers. The maximum of left-lateral river offsets is about 300 m. About 1

km to the north of this segment's eastern part, there is another 6 km long fault trace bounding the northern edge of a ridge with a left-lateral river offset in the Hisi River.

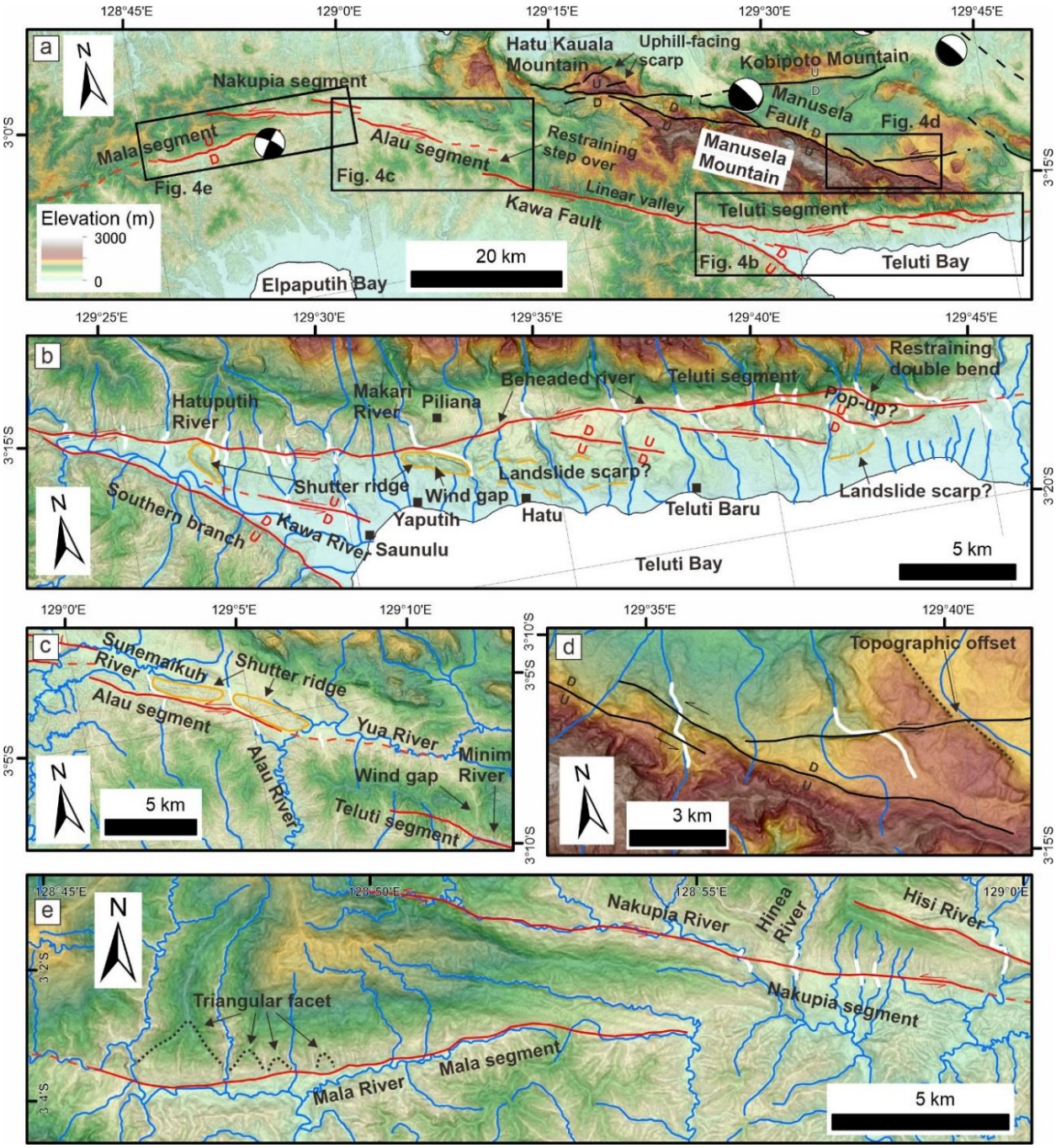

Figure 6.4 (a) Active fault map of the central Seram showing the trace of the Kawa and Manusela fault. (b) Tectonic geomorphic features of the southern part of the Teluti segment. (c) Shutter ridge and river offset associated with the Alau segment and a restraining step over between the Teluti and Alau segments. (d) Geomorphic offsets associated with the southern end of the Manusela fault. (e) Systematic left-lateral river offsets along the Nakupia segment and triangular facets along the Mala segment. Refer to Figure 6.3a for the legend. White lines along the fault trace indicate the river offset.

Mala segment. The Mala segment is located about 3 km south of the Nakupia segment (Figure 6.4a). This segment extends for about 33 km in an east direction (Figure 6.4e). The eastern part of this segment is characterized by a linear valley of the Mala River. Triangular facets are observed in the north of the Mala River and indicate vertical movement on this segment. The size of the facets increases towards the west. Further west, the fault trace runs along aligned saddles and south-facing scarps.

6.2.2.2 Manusela Fault

The Manusela fault is ~60 km long and subparallel to the Kawa fault (Figure 6.4a). The fault is considered a presumed or potentially active fault because the fault trace is mainly characterized by topographic lineament lacking evidence of recent faulting activity. In the eastern part of the fault, an offset of topographic slope on the mountainous area and river offsets record a left-lateral motion (Figure 6.4d). In the central part, the fault bounds the northern side of Manusela Mountain (Figure 6.4a). A fault strand traverses the southern edge of the Kobipoto Mountain. South of Hatu Kauala Mountain, the south-facing cliff marks the fault trace. Uphill-facing scarps are identified on the northern slope of the Hatu Kauala Mountain. The western end of the fault is associated with an intramountain depression. The nearest seismicity between the Manusela and Kobipoto Mountain indicates a shallow thrust fault solution with a small component of left-lateral slip on the east-trending nodal plane (Figure 6.4a).

6.2.3 East Seram

East Seram extends from Teluti Bay to the south of Waru Bay. The area lies on a mountainous terrain separated by the Bobot and Masiwang Rivers (Figure 6.5a). Two active faults are identified in this area, the Bobot and Masiwang faults.

6.2.3.1 Bobot Fault

In east Seram, the Bobot fault extends for ~90 km from the Teluti Bay to the south of the Waru Bay in a southeast direction (Figure 6.5a). From the west to the east, the fault traverses the broad valley of the Bobot River and crosses the valley of the Masiwang River. The fault consists

of two geometric segments, the Bemu and Kali segments. There is a strike-slip fault earthquake with a 16 km depth close to the Waru Bay and the southeast-trending plane records left-lateral movement (Figure 6.5a).

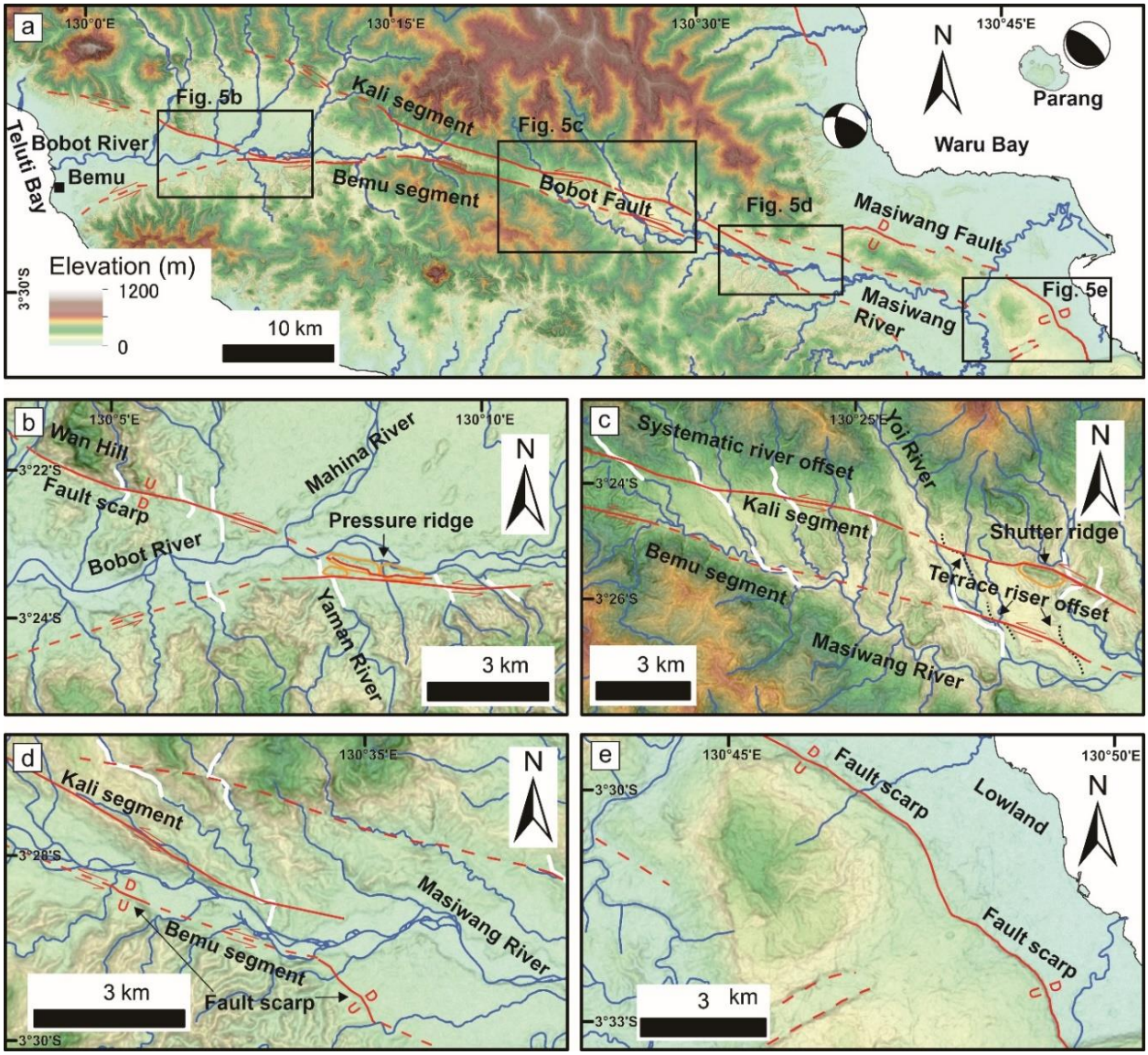

Figure 6.5 (a) Active fault map of east Seram showing the trace of the Kawa and Masiwang fault. (b) Pressure ridge on the fluvial surface at the junction of the fault splays. (c) Systematic left-lateral river offsets and terrace riser offsets along the Kali and Bemu segment. (d) ~15 m high fault scarps on a fluvial terrace along the Bemu segment. (e) Fault scarp of the eastern portion of the Masiwang fault. Refer to Figure 6.3a for the legend. White lines along the fault trace indicate the river offset.

Bemu segment. The Bemu segment extends for ~90 km from the Bobot River's valley to the Masiwang River's valley, showing a concave-to-the-south fault trace. To the west, the fault branches into two splays in the Bobot River's valley (Figure 6.5a, b). There are pressure ridges on

the fluvial terrace that emerged ~10 to 20 m from the adjacent surface, indicating the recent activity of this segment (Figure 6.5b). The ridges along the northern strand are intersected by a north-flowing river, indicating that the ridges have been uplifted while the river flows. Close to the Yaman River, a ridge deflects the river left-laterally. South of Wan Hill, the northern splay is marked by a fault scarp for 5 km, and further west, it continues along the mountain front with left-lateral river offsets.

Another fault splay is interpreted along the mountain front south of the Bobot River. Prominent left-lateral offset rivers denote the central part of the segment (Figure 6.5c). The river offset ranges from 200 m to 1.3 km. Two terrace riser offsets are identified in the Masiwang River's valley (Figure 6.5c). Two ~15 m high northeast-facing fault scarp on a fluvial terrace is identified in the valley, attesting to the fault's recent activity (Figure 6.5d). The geomorphic expression becomes faint further east after the 5 km wide restraining bend in the Masiwang River's valley.

Kali segment. To the north, the Kali segment extends for ~70 km and is mostly parallel to the Bemu segment (Figure 6.5a). The western part of this segment crosses mountainous areas, marked by saddles and left-laterally offset rivers. In the central part, systematic offset rivers show left-lateral displacement up to ~500 m, and a shutter ridge is identified along the fault trace (Figure 6.5c). There is a south-facing scarp on a fluvial terrace with a ~500 m left-lateral terrace riser offset immediately west of the shutter ridge. The eastern part of the segment is interpreted as a fault bounding the northern edge of the Masiwang River's valley.

6.2.3.2 Masiwang Fault

South of the Waru Bay, the Masiwang fault bounds the coastal lowland (Figure 6.5a). The fault extends for ~24 km in an east-southeast direction along the northern margin of a ridge in between the coastal lowland and the Masiwang River's valley. Northeast-facing fault scarps pronounce the fault trace. The fault concaves toward the northeast. In its eastern portion, a fault

scarp cuts a part of the ridge slope, indicating that the scarp is related to the faulting activity (Figure 6.5e). The geomorphic features suggest that the vertical component dominates the slip on the fault.

6.2.4 Amahai, Ambon, and surrounding Islands

There are many raised marine terraces south of the Elpaputih Bay, Ambon, Haruku, and Saparua (Figure 6.6a). The terraces are the late Pleistocene–Holocene age (Tjokrosapoetro et al., 1993c) and indicate Quaternary uplift relative to the area north of the Seram Strait. Most of the fault traces vertically deform the lowest marine terraces, indicating relatively young faulting activity.

6.2.4.1 Amahai Fault

The Amahai fault is indicated by 30–40 m high north-facing scarps on the marine terraces east of the Elpaputih Bay (Figure 6.6a, b). The fault is ~17 km long and disappears at the coast in Amahai. West of Amahai, a 12 km deep normal fault earthquake shows that its nodal planes have a similar orientation to the Amahai fault (Figure 6.6a). The fault plausibly continues offshore in Elpaputih Bay.

6.2.4.2 Ambon, Haruku and Saparua Faults

There are many northeast-trending fault scarps on the marine terraces in Ambon facing to the southeast or northwest (Figure 6.6a), defined as the Ambon fault. The Ambon fault traverses from the Ambon Bay to the northernmost of Ambon for ~34 km. North of Ambon Bay, the marine terraces are vertically offset ~100 m by the fault (Figure 6.6c). South of Ambon Bay, the fault also deforms several marine terraces. In Tulehu, fault scarps are identified cutting the marine terraces (Figure 6.6d). Most of the fault scarps face to the northwest. The height of the scarps ranges 30–90 m. A depression occupied by Tihu Lake is bounded by fault scarps (Figure 6.6d). To the north of Tulehu, 30–70 m high fault scarps cut the marine terraces in Lengkong (Figure 6.6e). There is a ~1.6 km gap separating this fault trace in Lengkong from the fault trace in Tulehu. The southeast-facing fault scarps displace the lowest terrace surface (Figure 6.6e). The fault trace disappears further north, close to the coastline.

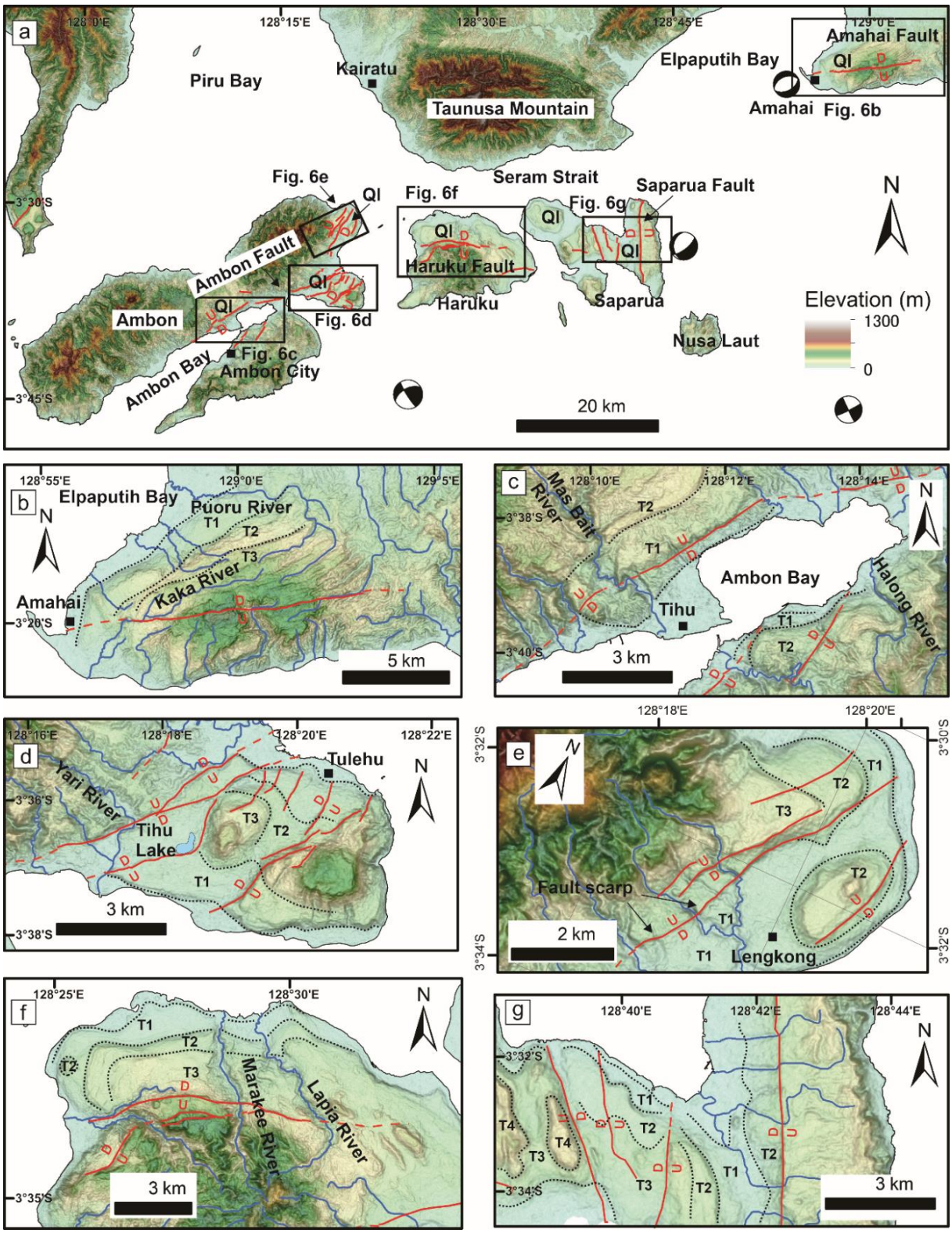

Figure 6.6 (a) Active fault map of the Ambon and surrounding areas. (b) The Amahai fault that cuts the marine terraces in Amahai. (c) Fault scarp in the north of Ambon Bay. (d) Faults deforming the marine terraces in Telehu. The Tihu Lake is bounded by fault scarp on the southern and eastern sides. (e). Fault scarp on the T1 surface west of Lengkong. (f) Fault scarp in Haruku, clearly deforming the marine terraces. (g) Fault scarp on marine terraces in Saparua. Refer to Figure 6.3a for the legend. Dotted black lines mark the terrace surface boundaries.

Other faults in Haruku and Saparua also show vertical displacement, but the faults show different orientations (Figure 6.6a). The 14-km-long Haruku fault generally trends in an east-west direction, but the western part of the fault curves into a northeast direction (Figure 6.6f). The Haruku fault deforms the marine terrace. The 12-km-long Saparua fault has a north-south orientation and cuts the marine terraces (Figure 6.6g). The nearest earthquake is a 17 km deep normal fault earthquake east of Saparua (Figure 6.6a). The north-south nodal plane is parallel to the Saparua fault.

6.2.5 Buru

Buru lies on mountainous terrains, except for a lowland at Kayeli Bay (Figure 6.2). On Buru's northern coast, several flights of marine terraces indicate young tectonic uplift (Figure 6.7a). The marine terraces are back tilted southeastward. Several hanging valleys associated with the fluvial terrace deposits are identified within the mountainous terrain, such as in the Putih River's upstream area and the east of the Rana Lake (Figure 6.7a, b). Tjokrosapoetro et al. (1993b). suggested an age of the late Pleistocene–Holocene for the fluvial terraces.

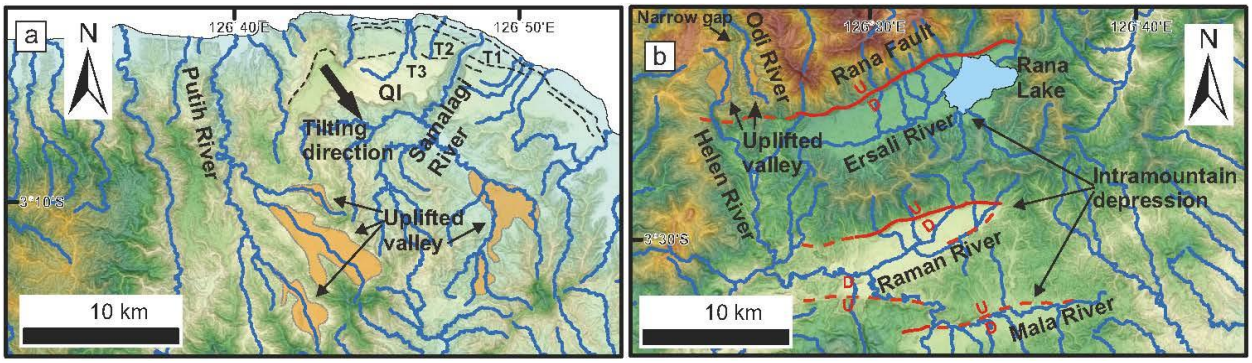

Figure 6.7 (a) Marine terraces in the north Buru and uplifted valley (orange-colored polygons) associated with fluvial terrace deposits in the upstream area of the Samalagi and Putih River. Dashed black lines mark the marine terrace surface boundaries. (b) Intramountain depressions bounded by the active faults in central Buru. Refer to Figure 6.3a for the legend and Figure 6.6a for the elevation color scale.

Several parallel fault traces are identified within the mountainous terrain (Figure 6.7b). The faults are associated with the intramountain depressions, filled by the late Pleistocene–Holocene deposits. These faults are defined as the Rana fault system. The Rana fault north of Rana Lake is the longest fault trace of this system. Two hanging valleys are identified in the western part of the

Rana fault (Figure 6.7b). A narrow gap between these valleys indicates that the upstream valley in the Helen River was previously connected to the Odi River, and the Rana fault's motion might cause the valley to uplift and now flows southward through the Helen River. A 10 km deep normal fault earthquake solution, located ~40 km east of Lake Rana, shows a similar plane orientation to these faults (Figure 6.7b).

6.3 Tectonic landforms and shallow-subsurface structures of the Ambon fault

The Ambon fault is segmented into three geometrical segments based on its strike directions (Figure 6.8). This section describes the Ambon fault based on the segmentation. The colored dotted lines on GPR mark examples of prominent reflectors on each profile and are referred by their color in this section.

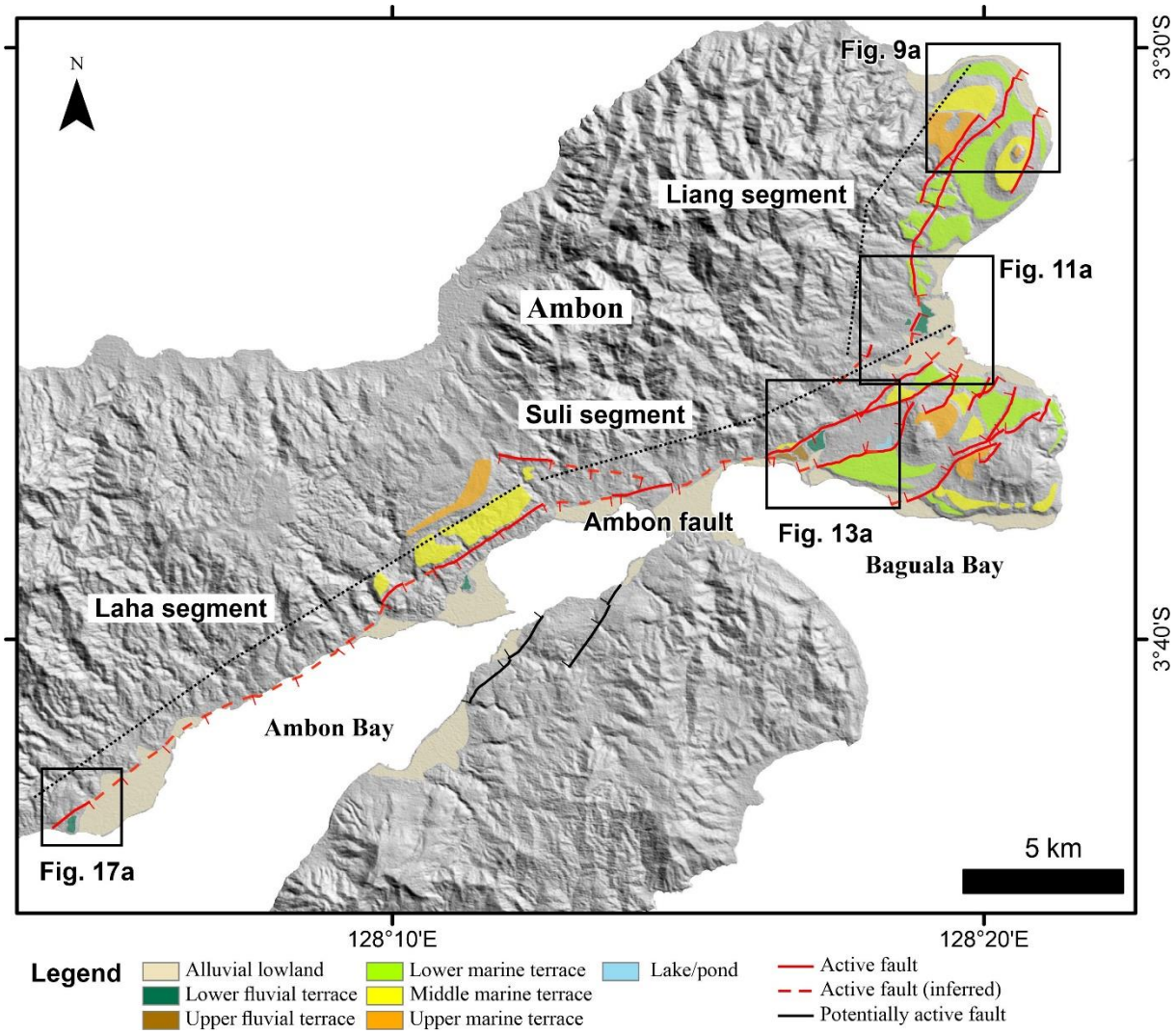

Figure 6.8. Active fault map of Ambon. The Liang, Suli, and Laha segment trends in N20°E, N70°E, and N55°E directions, respectively.

6.3.1 Liang segment

The Liang segment is characterized by fault scarps cutting lower marine terraces (Figure 6.8). The segment is composed of three surface traces. The longest trace is about ~10 km long, while the other two traces are ~3 km long. The scarp height is as large as 50 m, suggesting that the fault scarps are relatively old, plausibly Pleistocene. However, a warped surface on the alluvial lowland at location AM01 indicates a recent deformation on this geomorphic surface (Figure 6.9b, c). The topography of this surface tilt ~1° toward the fault. At the northern portion, two GPR profiles were acquired crossing two fault traces of this segment (Figure 6.9a).

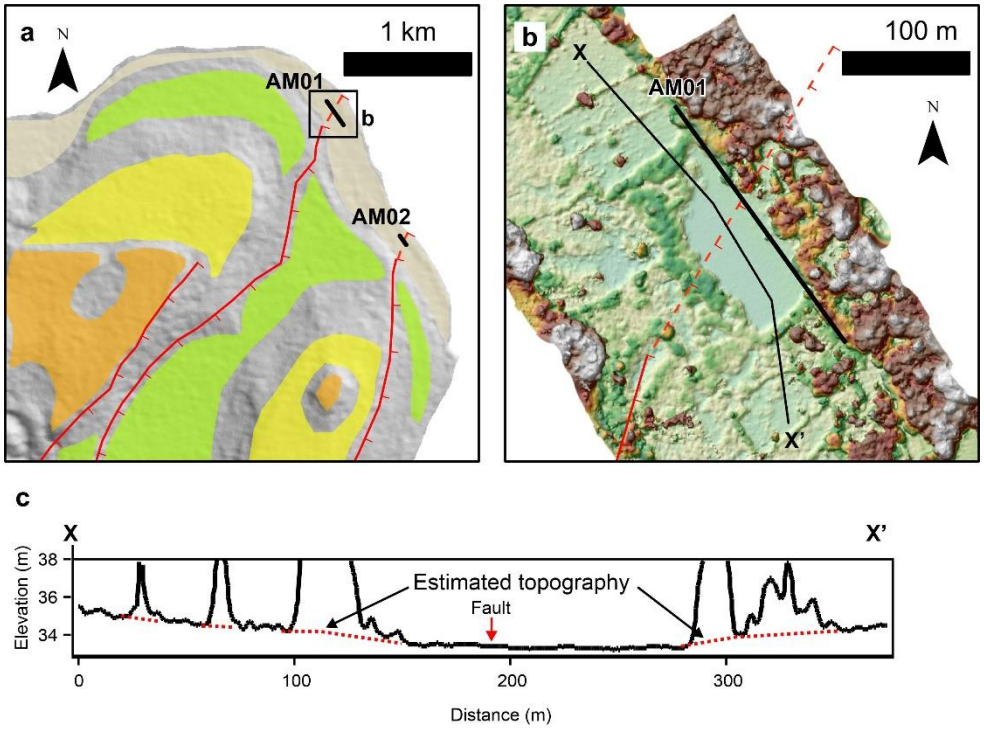

Figure 6.9 (a) Tectonic geomorphic features on the northern portion of the Liang segment. (b) DSM of the area around the AM01 line. (c) Profile along the X–X' line in b. Note that spikes are due to vegetation.

The AM01 line crossed the main trace of the Liang segment (Figure 6.9a, b). The depth-converted section and its interpretation are shown in Figure 6.10a and b. The section shows prominent undeformed reflectors at the shallower part, 0–2 m deep (yellow). The deeper part is characterized by several faulted reflectors (green and cyan). Warped reflectors are identified between the distance of 75 and 125 m beneath the undeformed reflectors. This observation is in agreement with the geomorphic expression recorded in Figure 6.9c. Seven fault traces are

interpreted based on reflectors' discontinuities below the undeformed reflectors, and the main fault is located at the distance of 77 m with the largest vertical displacement of ~1 m (Figure 6.10b). The main fault records a normal sense of movement, down to the south with a dip of ~60°.

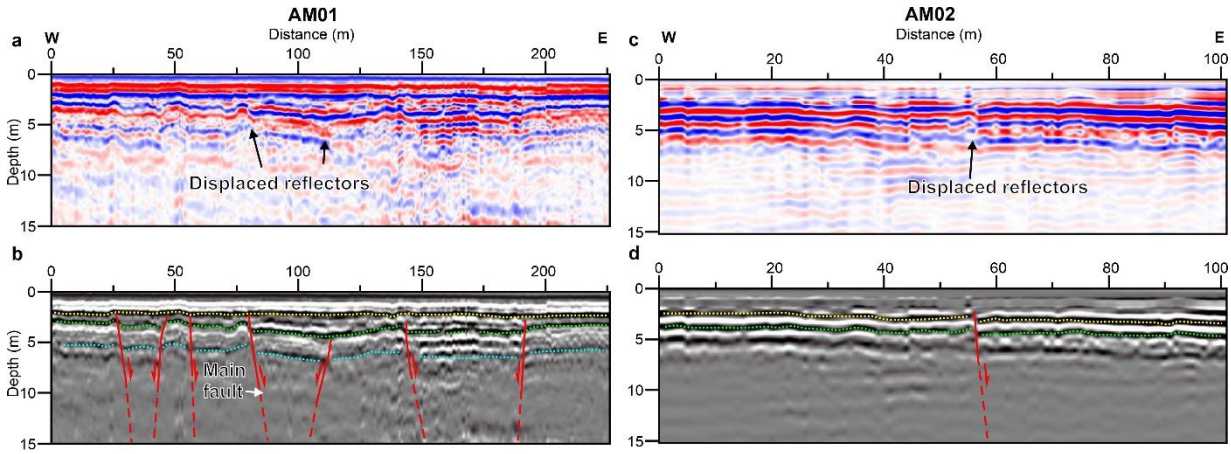

Figure 6.10. (a and b) Processed GPR section of the AM01 line and its interpretation. (c and d) Processed GPR section of the AM02 line and its interpretation.

The AM02 line intersected a fault trace east of the major fault line. Figure 6.10c and d show the processed section and its interpretation. The 2 m uppermost portion is characterized by faint reflection. However, beneath this portion, prominent continuous reflectors indicate a parallel stratification. A ~0.6 m down-to-the-east vertical offset at the distance of 56 m marks the fault. The fault dips toward the east at ~60°, similar to the main fault at the AM01 profile.

Further south, at location 1, a fluvial terrace deposit shows a tilt of 6–7° towards the fault or westward (Figure 6.11a, b). The tilted deposit is composed of interbedding of sand, gravel, and silt in places with abundant plant materials. The tilting is interpreted to be related to tectonic activity, rather than associated with the initial slope of deposition. The river where the deposit was observed flows eastward, and the initial slope of deposition follows the direction of river flow. Modern alluvium overlies the tilted deposit. The base of the alluvium slopes eastward, similar to the flow river's direction. Based on this observation, the tilted deposit might be caused by a faulting activity after its deposition and before alluvium.

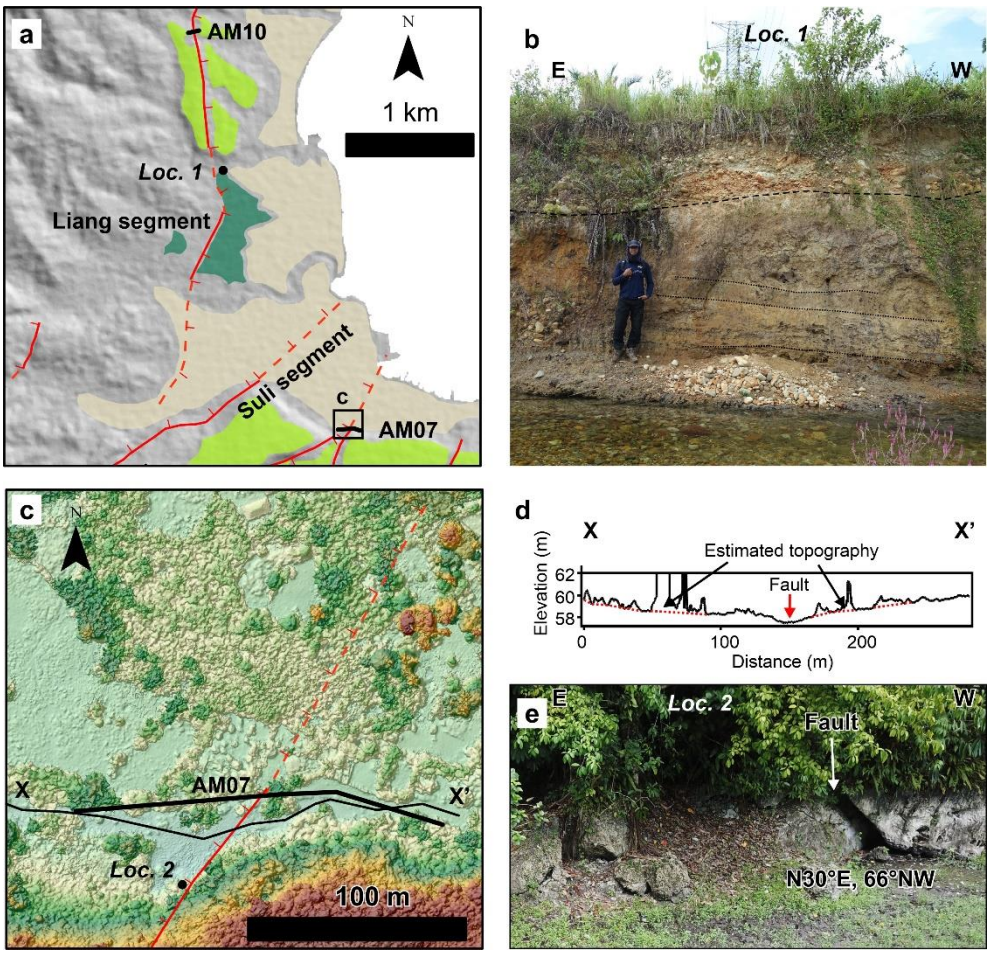

Figure 6.11 (a) Tectonic geomorphic features on the southern portion of the Liang segment and the northern part of the Suli segment. (b) Toward-the-west tilted fluvial deposits at location 1. (c) DSM of the area around the AM07 line. (d) Profile along the X–X' line in c. Note that spikes are due to vegetation. (e) A fault on the limestone of the middle marine terrace.

The AM10 profile was acquired north of location 1, crossing a ~8 m high fault scarp (Figure 6.11a). The section shows strong reflections at the 5 m uppermost portion (Figure 6.12a, b). The shallow reflectors are parallel to the topography. However, a normal fault is interpreted at the distance of 56 m where a reflector (green) onlaps another displaced reflector. The dip of the fault is ~60°, down to the east. The vertical offset is calculated at 2 m, twice as large as the vertical offset observed in the AM01 profile.

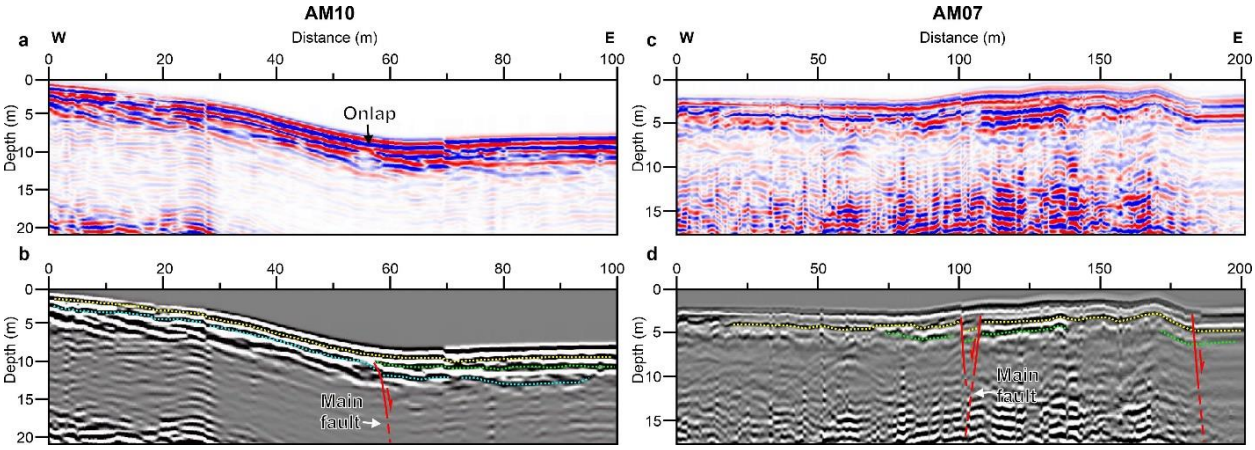

Figure 6.12 (a and b) Processed GPR section of the AM10 line and its interpretation. (c and d) Processed GPR section of the AM07 line and its interpretation.

6.3.2 Suli segment

The Suli segment consists of numerous fault traces and it extends for ~15 km (Figure 6.8). The segment cuts the lower marine terraces, and lower and upper fluvial terraces. The fault scarps on the lower marine terrace range ~9–30 m high. There are also fault scarps on younger geomorphic surfaces such as the lower and upper fluvial terraces, with a height of ~1 and ~5 m, respectively. A prominent depression partly occupied by Lake Tihu is bounded by ~10 m high scarp to the south (Figure 6.13).

In the northern part of this segment, at location 2, a fault outcrop indicates an attitude of N210°E/66°NW (Figure 6.11c, e). This orientation agrees with the northwest-facing fault scarp. There is a hot spring next to this location. The DSM profiles along low vegetated surfaces indicate that topography is curved toward the fault with a ~1° slope (Figure 6.11d). Local people informed that location 2 is inundated during the rainy season, meaning that location 2 is slightly lower than the adjacent area. The warped topography suggests a young deformation that might be due to paleoseismic activity.

The AM07 profile was acquired immediately north of location 1. The final GPR section with the interpretation is presented in Figure 6.12c and d. Parallel stratified reflectors are observed at the shallower part down to a depth of ~3 m. The offset reflectors at the distance of ~107 m mark the main fault. The fault is evident of the normal sense of motion, down to the west with a dip of

about 60°. The main fault on the GPR profile is the subsurface continuation of the fault at location 2. On the GPR section, the main fault splays into two upward, and this plausibly relates to the depression at location 2. There is another normal fault at the distance of ~185 m, down-to-the east.

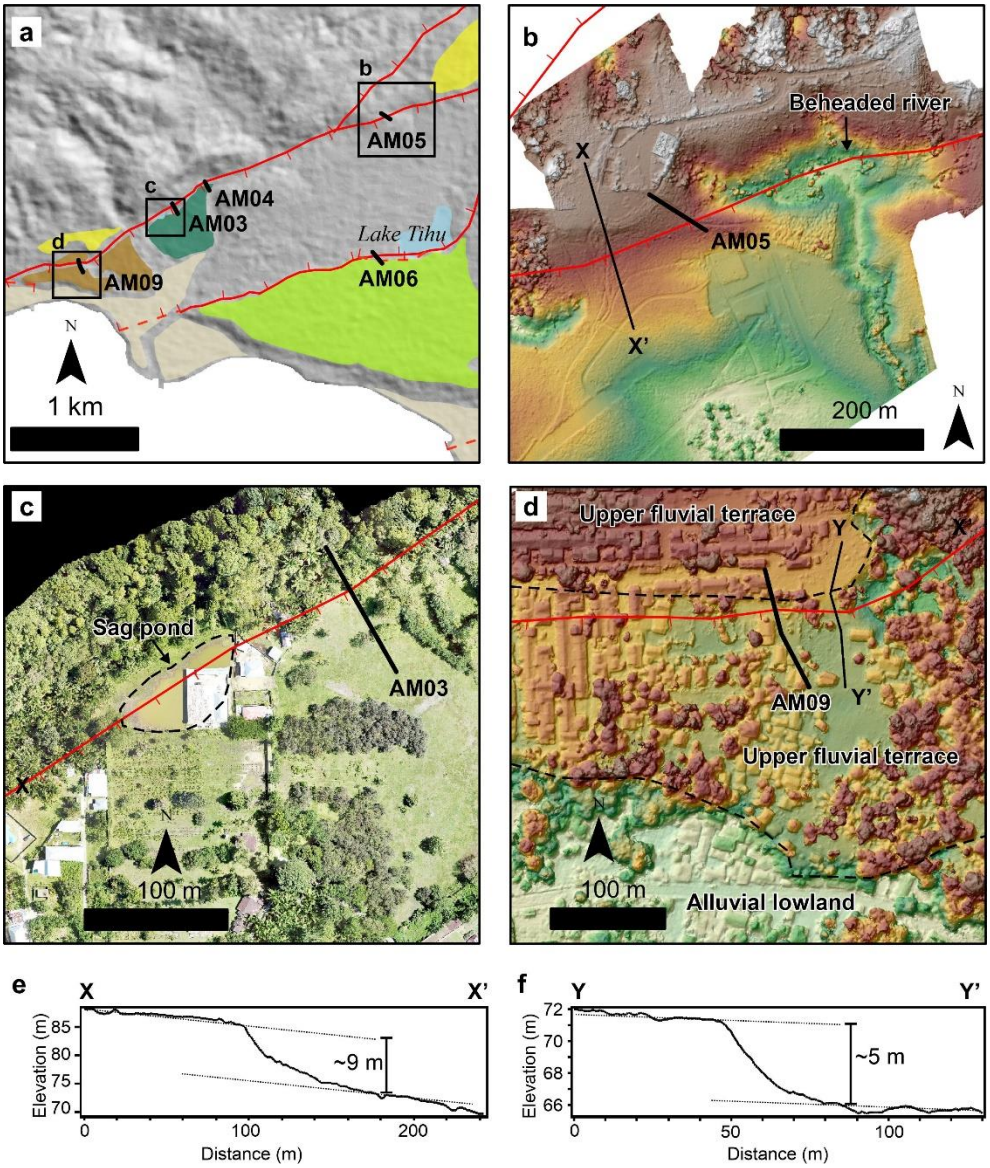

Figure 6.13 (a) Tectonic geomorphic features on the central portion of the Suli segment around Lake Tihu. (b) DSM of the area around the AM06 line, showing a fault scarp and beheaded river. (c) Orthophoto of the area around the AM03 line. (d) DSM of the area around the AM09 line, showing the deformed fluvial terrace. (e) Profile along the X–X' line in (b). Vegetation covers are relatively low. (f) Profile along the Y–Y' line in (d). Vegetation cover at the Y–Y' line is relatively low.

North of Lake Tihu, there is a fault scarp and a beheaded river (Figure 6.13b). Field inspection reveals tuff underlies this site. The vertical offset of the scarp is calculated at ~9 m (Figure 6.13e). A beheaded river suggests that it truncates to the fault, and there is no possible

river further north that might be its upstream portion. At this location, there are a geothermal well and a geothermal manifestation as warm ground. The AM05 section was acquired crossing the fault scarp (Figure 6.13b). The depth-converted profile and its interpretation are displayed on Figure 6.14a and b. A fault is interpreted as offset reflectors at the distance of 56 m with a normal sense of slip, down to the southeast and steeply dips ~80°. A reflector at a depth of 7 m records ~5 m vertical displacement (cyan).

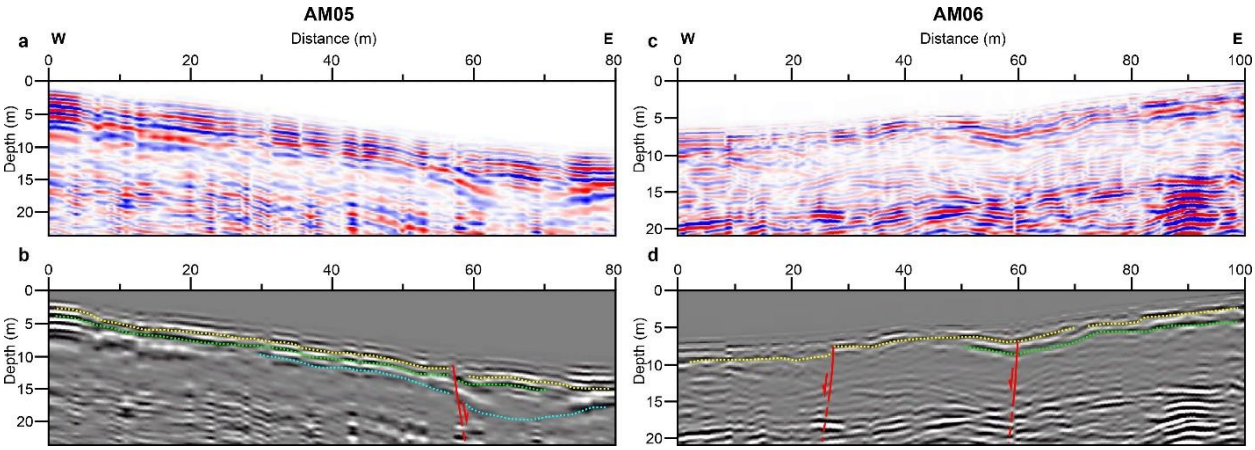

Figure 6.14 (a and b) Processed GPR section of the AM05 line and its interpretation. (c and d) Processed GPR section of the AM06 line and its interpretation.

The AM06 line intersects a northwest-facing fault scarp west of Lake Tihu (Figure 6.13a). Figure 6.14 c and d show the final-processed profile and interpretation. A displaced reflector (yellow) at the distance of 27 m indicates a normal fault, down to the northwest. The reflectors at the distance of 60–70 m dip westward and those at the distance of 50–60 incline toward the east, and a fault is interpreted in between the oppositely dipping reflectors.

The AM03 profile was collected on the lower fluvial terrace, crossing an interpreted fault trace northeast of a sag pond (Figure 6.13a, c). The profile and its interpretation are presented on Figure 6.15a and b. The main fault is identified at the distance of 37 m as displaced reflectors and dips ~70° towards the east. A thickened-toward-fault reflector at ~7 m deep and 35–55 m distance is truncated by the main fault. The vertical displacements of reflectors become larger downward from 0.6 m on the yellow reflector to 2.6 m on the cyan reflector. These features might be due to

multiple surface faulting events. Two other faults at the distance of 78 and 97 m are indicated by offset reflectors and dip in opposite direction, westward.

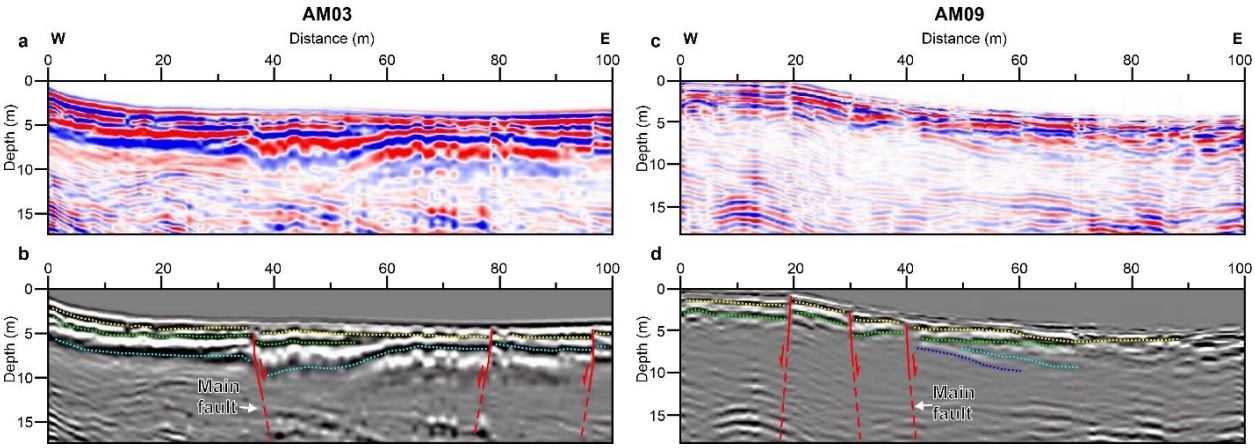

Figure 6.15 (a and b) Processed GPR section of the AM03 line and its interpretation. (c and d) Processed GPR section of the AM09 line and its interpretation.

Further southwest from the AM03 site, a deformed fluvial terrace is identified at the AM09 site (Figure 6.13a, d). The fault scarp is 4–5 m high, facing to the south (Figure 6.13f). The AM09 profile was acquired on the fluvial terrace. The depth-converted sections and interpretation are shown on Figure 6.15c and d. Several discontinuities mark the fault location, but the fault at the distance of 40 m is interpreted as the main trace as it exhibits the fault scarp. The main fault has a normal sense of motion down to the east. All faults vertically displace the shallower-than 4 m depth reflectors (yellow and green). There are reflectors beneath these reflectors at the distance of 40–70 m that incline eastward and truncate to the main fault (cyan and blue).

In addition, shallow boring was done manually to obtain the stratigraphy of this upper fluvial terrace in the AM09 site (Figure 6.16). Holes 1 and 2 are located on the upthrown side whereas Hole 3 is in the downthrown block. This reveals that both sides of the fault are composed of sand with intercalation of silt. The silt can be a marker for correlating the unit from these holes. Several charcoal materials were collected from these holes.

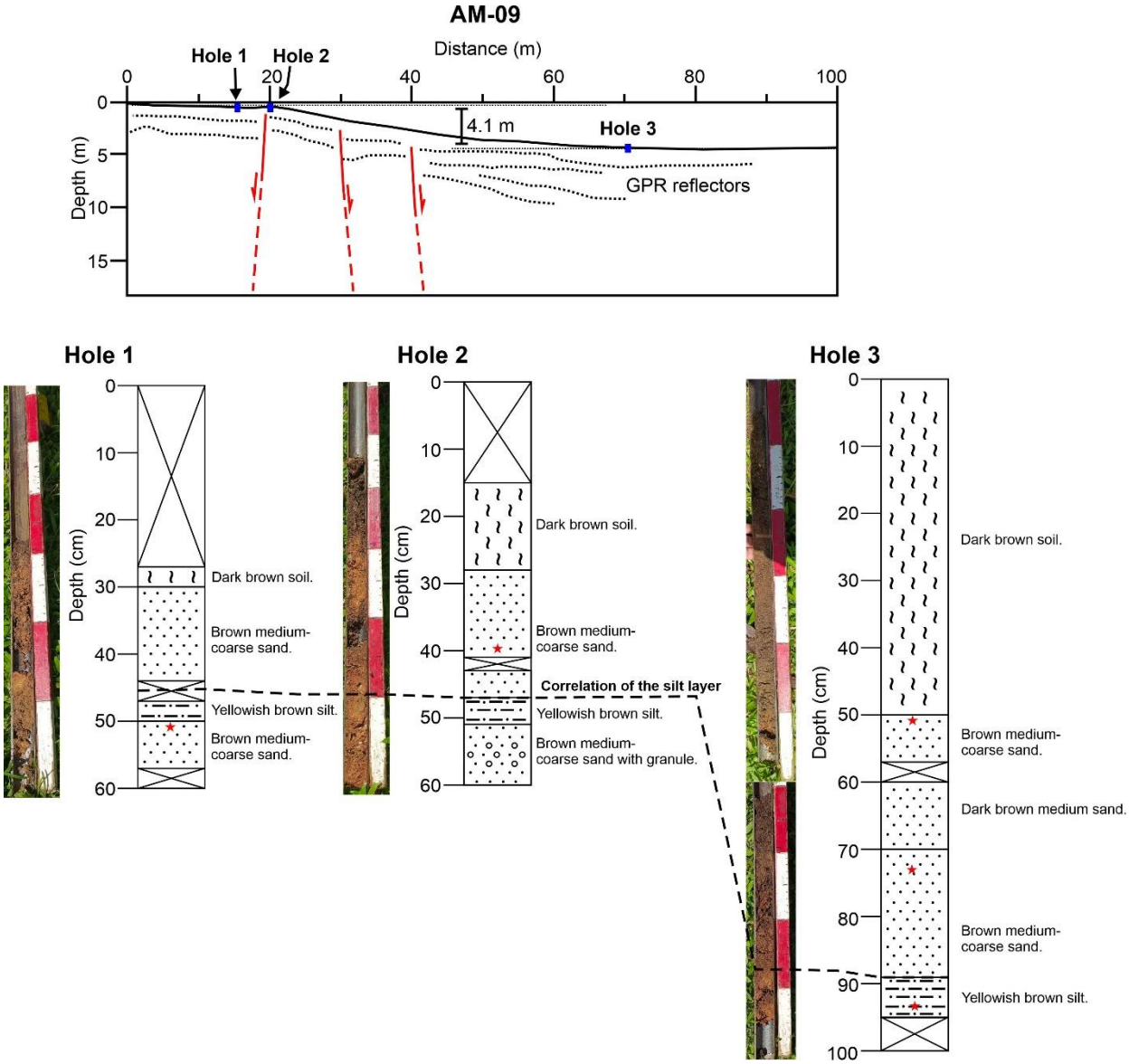

Figure 6.16 Stratigraphic correlation between Holes 1, 2, and 3 at the AM09 line.

6.3.3 Laha segment

The Laha segments extend for about ~18 km in an N 55° E direction. Its northern portion is identified as a 70–100 m high fault scarp cutting the middle marine terraces (Figure 6.8). The fault trace is interpreted further south following mountain foot (Figure 6.8). A fault scarp is observed at its southernmost end (Figure 6.17). To confirm the fault locations, the GPR profiling was conducted on the alluvial lowland, just north of the fault scarp (Figure 6.17).

On the AM-11 section, the 2 m uppermost reflectors are generally flat (Figure 6.17). The fault is marked by displaced reflectors (blue) at the distance of 67 m. The fault is almost vertical with a 1 m offset, down to the east. East of the fault, a reflector (green) truncates to the fault. The

observation on this GPR section suggests that the latest faulting event predates the deposition of alluvium at the surface. The truncated reflectors may represent sedimentary units that were deposited after the most recent seismic event on the fault.

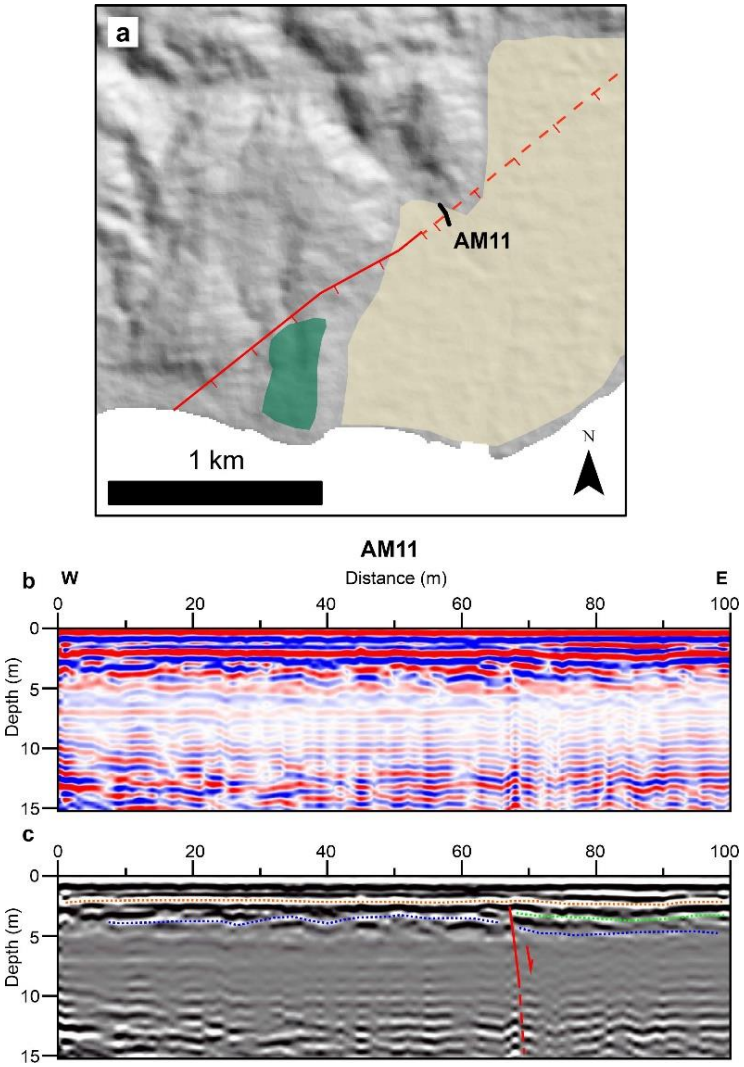

Figure 6.17 (a) Geomorphology of the southern portion of the Laha segment. (b and c) Processed GPR section of the AM11 lines and its interpretation.

6.4 Potential seismic hazards

The study of the northern Banda arc has identified active faults and fault segments in the northern Banda Arc onshore region that may rupture independently. The earthquake potential magnitudes for each fault and fault segment were estimated using an empirical relationship between surface rupture length and magnitude from Wells and Coppersmith (1994) (Figure 6.18, Table 6.1). For the calculation, maximum potential rupture lengths for active faults are determined

based on the nature of fault termination. Earthquake rupture are likely to be arrested at ≥4 km wide gaps, as suggested by Wesnousky (2008). The calculation is purely based on the observed length on land. Some fault traces disappear at the coastline, so the faults may continue offshore or link to the adjacent faults. In such a case, the potential earthquake might be larger than the calculations in this section.

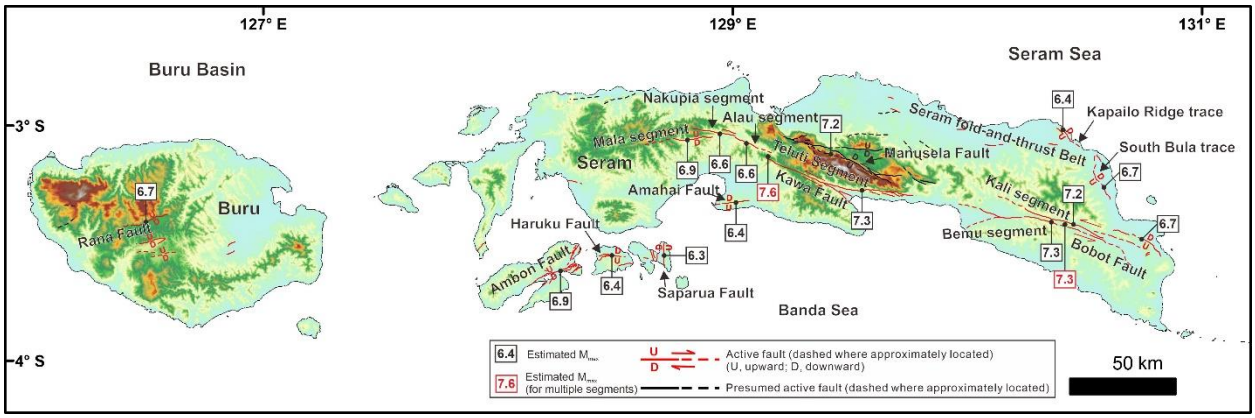

Figure 6.18 Map of the magnitude (M_w) of the maximum potential earthquakes of the study area's active faults.

Since active faults in north Seram and the Masiwang fault are related to the thrusting activity, the active faults are assigned as reverse faults for the calculation. Active faults in central and east Seram clearly show left-lateral strike-slip movement. Active faults in Amahai, Ambon, and Buru are assigned as normal faults in this calculation because the nearest seismicity shows normal fault solutions. Additionally, the investigation in Ambon has revealed that the Ambon fault is a normal fault.

All active faults in the region have a maximum potential earthquake M_w ≥6.4. All strike-slip faults have a potential M_w of 7. The largest potential M_w of 7.6 is attributed to the Kawa fault if all segments rupture simultaneously. In 1899, an M_w 7.8 earthquake occurred in Seram and damaged the Teluti, Elpaputih, and Piru Bay and the event has also generated a tsunami along these bays (Brune et al., 2010). The earthquake might have ruptured the Kawa and Bobot faults simultaneously (Watkinson and Hall, 2017).

Table 6.1. Potential earthquake magnitudes for the active faults in the onshore northern Banda Arc.

Structure Name		Length (km)	Type	Potential magnitude*	Geomorphic features	Nature of fault terminations
Fault	**Segment**					
Seram fold-and-thrust Belt	Kapailo Ridge trace	14	R	6.4	Kapailo ridge, wind gaps, fault scarps	The northwest end disappears close to the coastline. The southeast end terminates before reaching Bula.
Seram fold-and-thrust Belt	South Bula trace	24	R	6.7	Fault scarps on lowland and fluvial terraces	Both ends terminate on lowland.
Kawa	-	137	S	7.6	-	-
Kawa	Teluti	75	S	7.3	River offsets, shutter ridges, wind gaps, fault scarps, linear valley	~1.5-km-wide restraining double bend at the eastern end. ~3-km-wide contractional step over at the western end.
Kawa	Alau	20	S	6.6	Shutter ridges, river offsets	~3-km-wide contractional step over at the eastern end. ~500-m-wide contractional step over at the western end.
Kawa	Nakupia	21	S	6.6	Linear valley, river offsets	~500-m-wide contractional step over at the eastern end. The western end terminates in Nakupia River
Kawa	Mala	33	S	6.9	Linear valley, triangular facets.	The eastern end is deflected. The western end terminates in mountainous terrain.
Manusela	-	60	S	7.2	River offsets, slope offset, fault scarps	The eastern end branches into two strands. The western end is associated with intramountain depression.
Bobot	-	90	S	7.3	-	-
Bobot	Bemu	90	S	7.3	Fault scarps, river offsets, pressure ridges, terrace riser offsets	~5-km-wide restraining bend at the eastern end. Western end branches into two strands.
Bobot	Kali	72	S	7.2	Fault scarps, River offsets, shutter ridges, terrace riser offsets	The eastern end terminates in Masiwang River's valley. The western end is deflected.
Masiwang	-	24	R	6.7	Fault scarps	Both ends curved towards the southwest.
Amahai	-	16	N	6.4	Fault scarps on marine terraces	The eastern end terminates. The western end disappears near the coastline, at Amahai.
Ambon	-	34	N	6.9	Fault scarps on marine terraces, Tihu Lake	The northern end disappears near the coastline, at Liang. The southern end disappears north of Ambon Bay.
Haruku	-	15	N	6.4	Fault scarps on marine terraces	The western end disappears near the coastline. The eastern end terminates on the marine terrace surface.
Saparua	-	12	N	6.3	Fault scarps on marine terraces	Both ends disappear at the coastline.
Rana	-	24	N	6.7	Rana, fault scarps, Hanging valleys	The western end is deflected. The eastern end terminates close to Rana Lake.

*Using empirical length-magnitude relationship from Wells and Coppersmith (1994).

$M_w = 5.00 + 1.22 \times \log10(SRL)$ for reverse fault (R)

$M_w = 5.16 + 1.12 \times \log10(SRL)$ for strike-slip fault (S)

$M_w = 4.86 + 1.32 \times \log10(SRL)$ for normal fault (N)

The Ambon fault can produce an M_w 6.9 earthquake. Ambon has experienced several damaging earthquakes since 1674, but none of them were attributed to the Ambon fault. The recent

2019 M_w 6.5 Ambon earthquake damaged Ambon Island and possibly occurred on an offshore fault (Sahara et al., 2021). However, the Ambon fault can cause a devastating seismic event and pose a significant risk because it lies near the populous area, Ambon City. Since the Ambon and Haruku faults disappear at the coast, there is a possibility that both faults are linked. The relationship between the Ambon and Haruku faults offshore should be clarified to estimate more accurately the potential seismic hazard in Ambon and the surrounding area.

6.5 Kinematics of the northern Banda Arc

Fault scarps and wind gaps on ridges in Bula attest the active deformation in north Seram. The Seram fold-and-thrust belt's activity offshore as imaged by seismic reflection profiles (e.g., Baillie et al., 2019; Pairault et al., 2003; Patria and Hall, 2017) might have uplifted marine terraces along the northern coast of Seram, two of which are back tilted (Figure 6.19). The Seram fold-and-thrust belt is active because the thrust faults deform the upper stratigraphic unit (Pairault et al., 2003; Patria and Hall, 2017). Shallow thrust fault earthquakes are mainly located in north Seram (Figure 6.1b). So, the deformation observed in north Seram's geomorphology is plausibly due to the Seram fold-and-thrust belt. Limited geomorphic expression in north Seram suggests that the thrust faulting mainly occurs offshore. The Masiwang fault is interpreted to be associated with the thrusting activity because the geomorphic evidence mainly shows the vertical displacement.

Left-lateral strike-slip faults are dominant in central and east Seram. The systematic left-lateral offsets are as large as ~2 km for the Kawa fault. The Kawa fault is the largest structure in central Seram and is separated from the Bobot fault by the Teluti Bay. Immediate offshore east Seram, an offshore fault identified by Patria and Hall (2017) based on multibeam bathymetry, has a similar strike to the Bobot fault (Figure 6.19). There are also two left-lateral strike-slip faults in the west of Kumawa and north of Boano, identified on multibeam bathymetry (e.g., Patria and Hall, 2017; Teas et al., 2009). The fault in the west of Kumawa extends for ~120 km in a southeast direction. The left-lateral strike-slip fault in the north of Boano trends in an east direction and

extends for ~110 km. Watkinson and Hall (2017) have proposed a left-lateral strike-slip fault system extending from Kumawa to Seram. However, the fault system plausibly extends further north of Seram to the strike-slip fault in the north of Boano to form a ~580 km fault system and terminates at the Buru Basin. (Figure 6.19).

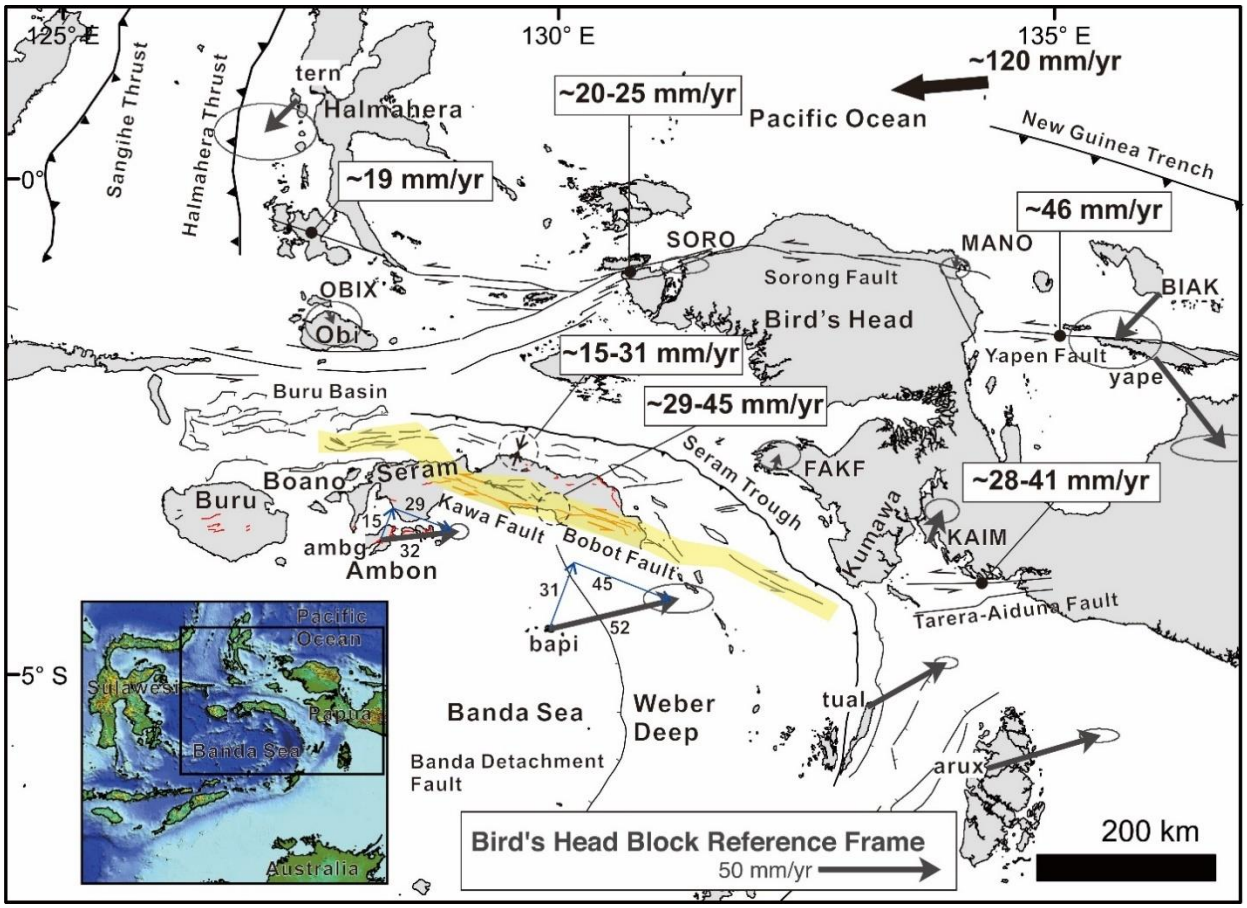

Figure 6.19 Schematic active tectonics model for the northern Banda Arc and Bird's Head. Major structural elements are from Hall (2012). The yellow-colored zone is the proposed strike-slip fault system. Geological structures in offshore Seram, Buru Basin, and Weber Deep are compiled from Pownall et al. (2016), Patria and Hall (2017), and Hall et al. (2017). The velocity field is derived from GPS surveys, relative to the Bird's Head, estimated by minimizing velocities at capital-labeled sites, from Bock et al. (2003).

All dip-slip faults in Amahai, Ambon, and surrounding islands cut Quaternary marine terraces. Boekschoten et al. (1989) suggested that the uplift of Ambon has begun in the Quaternary and the marine terraces have ages of the early–middle Pleistocene as the oldest. The Ambon fault cuts the lowest terrace surfaces and the alluvial lowland surfaces, indicating the recent activity of the fault. Most of the active faults have an east-to-northeast direction, except the north-south

oriented Saparua fault (Figure 6.19). The Saparua fault might serve as a transfer fault that links two other faults. The Amahai, Ambon, Haruku, and Saparua faults disappear at the coast, suggesting that these faults might extend further offshore. The Rana fault system in Buru which is associated with intramountain depressions indicates the extension in central Buru. The fault system has a similar orientation to the Miocene oceanic-spreading-related normal faults in the Buru Basin (Figure 6.19) identified by Patria and Hall (2017). Uplifted valleys and back-tilted marine terraces in north Buru attest that Buru has uplifted since the late Pleistocene.

Geodetic analysis by Stevens et al. (2002) suggested that the Bird's Head moves at ~80 mm/yr westward relative to Australia. This motion is translated on several left-lateral strike-slip faults in eastern Indonesia (Figure 6.19). The Yapen fault slips at ~46 mm/yr (Bock et al., 2003). The Sorong fault in the Bird's Head shows slight left-lateral motion (2–4 mm/yr) between Sorong (SORO) and Fakfak-Kaimana (FAKF-KAIM) sites (Bock et al., 2003). Two GPS sites, SORO and Manokwari (MANO), are close to the Sorong fault in the Bird's Head, within 20 km. If the fault is locked within the upper crust, GPS stations near the fault would not resolve significant differential motion during the interseismic period and should not be included in the slip rate calculation. Alternatively, using other sites: Ternate (tern) and FAKF-KAIM obtains a 20–25 mm/yr slip rate on the Sorong fault. Further west, south of Halmahera the Sorong fault's splay moves at ~19 mm/yr, between Ternate (tern) and Obi (OBIX) sites (Bock et al., 2003). Some portion of the left-lateral slip in eastern Indonesia is also accommodated by the Tarera-Aiduna fault, indicated by the 28–41 mm/yr velocity difference between KAIM and Tual-Aru (tual-arux) sites.

The northern Banda Arc could potentially absorb some portion of the Pacific plate's rapid motion (Watkinson and Hall, 2017). Bock et al. (2003) and Stevens et al. (2002) suggested that the northern Banda Arc converges with the Bird's Head in an east-northeast direction, oblique to the Seram Trough. If the geodetic velocity of Ambon (ambg) and Banda Api (bapi) sites are separated into parallel and normal components, relative to the Seram Trough, the parallel

component ranges 29–45 mm/yr in a southeast direction (Figure 6.19) and is plausibly accommodated by the strike-slip fault system in the northern Banda Arc. The strike-slip fault system also translates a left-lateral slip transferred from the Tarera-Aiduna fault. The Seram fold-and-thrust Belt accommodates 15–31 mm/yr convergence across the northern Banda Arc. The geodetic velocity of Ambon and Banda Api increases toward the east. The dip-slip faults in Ambon, Amahai, and Buru are plausibly related to this eastward velocity increase, which causes extensional deformation. A subduction rollback mechanism of the Banda Subduction, proposed by Spakman and Hall (2010), could explain the extensional deformation in a converging region.

The velocity difference between Ambon (ambg) and Banda Api (bapi) sites indicates a southeast-northwest extensional deformation in the Banda Sea south of Seram (Figure 6.19 and 6.20). The difference is estimated at 16 mm/yr, and the Ambon fault might accommodate a portion of this rate. The investigation in Ambon uncovers that the Ambon fault predominantly dips ~60° towards the east. The fault likely acts as an antithetic fault and attaches to the Banda detachment fault. The Banda detachment fault is a prominent low-angle (~8°) normal fault at the Weber Deep and slips at a rate of ~6 mm/yr (Cummins et al., 2020). The 7.2 km deep Weber Deep is a prominent submarine feature, which is not a subduction trench, in the region formed due to forearc extension driven by eastward subduction rollback (Pownall et al., 2016).

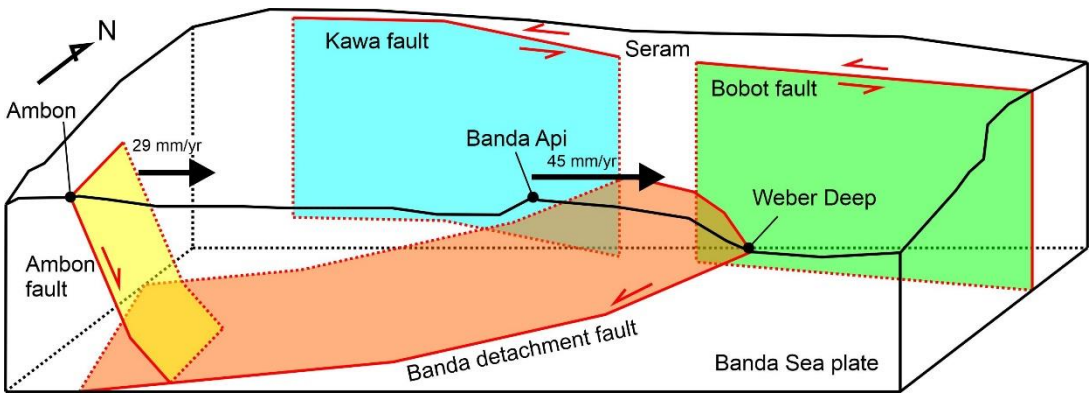

Figure 6.20 Schematic diagram of fault model in the northern Banda Arc. Arrows indicate the motion of Ambon and Banda Api sites parallel to the Kawa and Bobot faults, relative to Bird's Head of Papua, derived from geodetic velocity fields by Bock et al. (2003). There is 16 mm/yr velocity difference between Ambon and Banda Api sites. Structures of the Ambon, Kawa, Bobot faults are based on this study, while the Banda detachment fault is adapted from Pownall et al. (2016).

Chapter 7

Discussions

7.1 Active fault trace revisions

Results from the tectonic geomorphic observation have provided new detailed active fault traces for the study areas. This section presents the comparison between the previously published active fault maps and the results of this research and discusses the significance of the new revised active fault trace. Although primary locations of active faults along the strike-slip fault system have been identified (e.g., National Center of Earthquake Study (PUSGEN), 2017; Watkinson and Hall, 2017), the new active fault maps produced in this study differ from previous interpretations. In the previous map, the active faults are often interpreted following major lineaments with a lack of evidence of late Quaternary deformation. In this research, the active fault traces were identified based on an integrated technique for tectonic geomorphic interpretations described in section 2.1. High-resolution DEM (DEMNAS and LiDAR) and drone mapping have helped in the identification of subtle geomorphic features which may be related to recent faulting activities. In addition, shallow-subsurface geophysical surveys, described in sections 3.3 and 3.4, have aided to confirm active fault locations and determine fault geometry at the subsurface. The precise active fault traces in this study are essential geological data to accurately assess the seismic hazards in eastern Indonesia.

The 2018 M_w 7.5 Palu earthquake ruptured the intra-basin fault in the northwest Palu valley and the basin-bounding fault further south, separated by a 1 km wide gap (Figure 7.1). The intra-basin fault was interpreted as a result of the eastward faulting migration from the basin margin to intra basin. The intra-basin fault in a strike-slip basin often develops due to the tendency of the strike-slip fault to straighten, and it primarily accommodates the horizontal slip (Wu et al., 2009; Zhang et al., 1989). Before the 2018 earthquake, the surface traces of the Palu-Koro fault were not precisely mapped in the Palu Valley. This could be due to the low resolution of DEM data, which did not allow to identify subtle tectonic geomorphic features, or active fault traces have been

obscured by sediments or removed due to erosion. The Palu-Koro fault trace was interpreted following the basin margin separating the mountainous terrain and the Palu valley (National Center of Earthquake Study (PUSGEN), 2017) or as cross-basin faults which diagonally elongated within the Palu Valley (Watkinson and Hall, 2017). The existence of this intra-basin fault should be anticipated for a better seismic hazard assessment in a strike-slip basin.

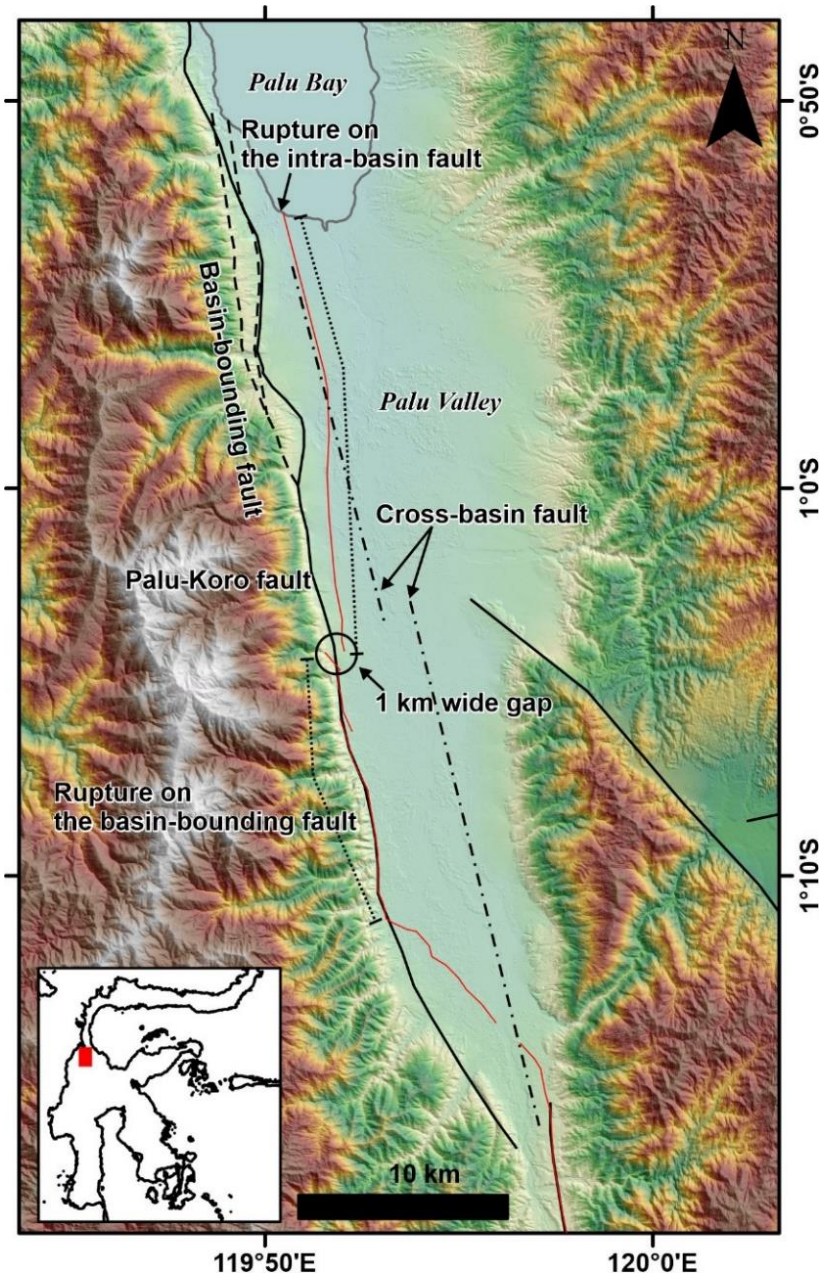

Figure 7.1 Comparison between the published active fault traces (solid black lines) by National Center of Earthquake Study (PUSGEN) (2017), the cross-basin faults (dot-and-dash black line) proposed by Watkinson and Hall (2017), and the surface ruptures of the 2018 earthquake in the Palu Valley (solid red lines) from this study and Natawidjaja et al. (2021). The dashed black lines indicate other basin-bounding faults in the northwest Palu Valley.

The easternmost Matano fault was previously interpreted as a fault bounding the Larongsangi basin's northern margin (National Center of Earthquake Study (PUSGEN), 2017; Watkinson and Hall, 2017). Using the high-resolution LiDAR data, the surface traces of the fault were precisely mapped (Figure 7.2). Unlike the published active fault map by National Center of Earthquake Study (PUSGEN) (2017) in which the easternmost Matano fault was only composed of two segments, the eastern Matano fault comprises complex fault traces. The complexity includes a step over between the Geresa and Balawai segments, forming a narrow basin with the Larongsangi segment as the intra-basin fault. The Larongsangi segment is also identified within the Larongsangi basin, parallel to the Geresa segment. Additionally, the Onepute segment is oblique to the Balawai segment and acts as a restraining bend at the termination of the Balawai segment. All segments appear to deform similar-age geomorphic features suggesting plausible simultaneous faulting activity. On strike-slip faults, the slip is often accommodated by multi fault segments which might rupture together during an earthquake, such as the 2018 Palu earthquake (This study, Natawidjaja et al., 2021), the 2016 Kumamoto earthquake in Japan (Toda et al., 2016), and the 1930 Pegu earthquake in Myanmar (Tsutsumi and Sato, 2009).

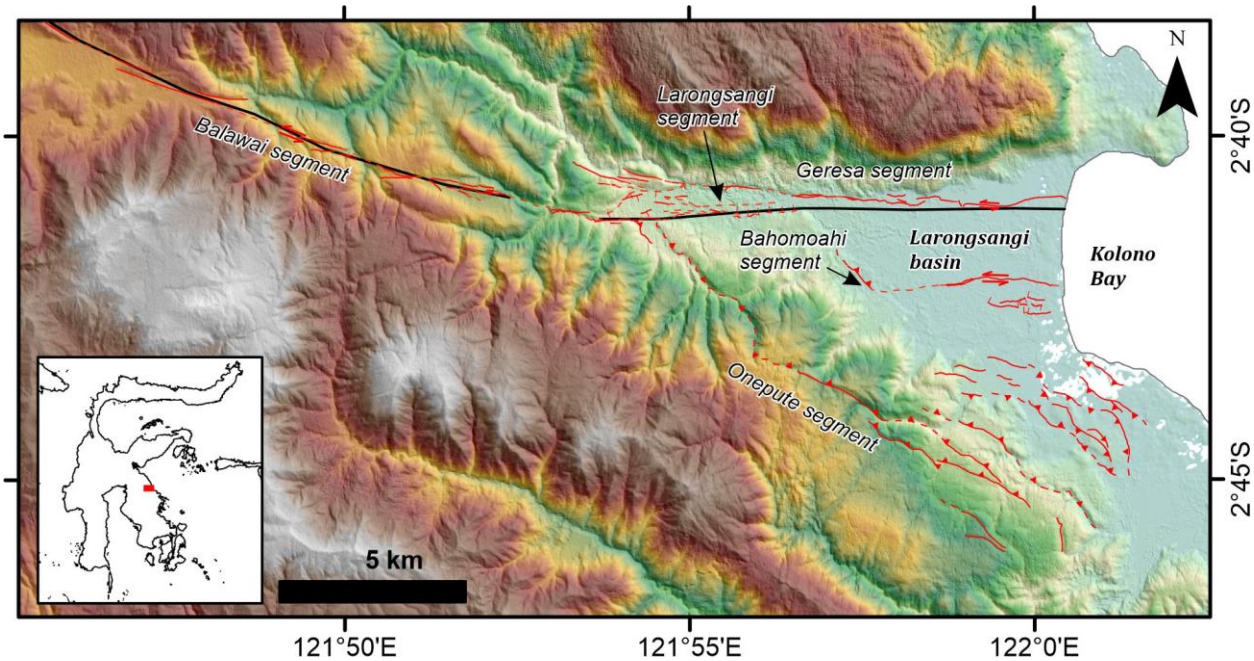

Figure 7.2 Comparison between the published active fault trace (black) by National Center of Earthquake Study (PUSGEN) (2017) and the new active fault interpretation (red) for the easternmost Matano fault.

Results from active fault mapping in the onshore northern Banda Arc showed the detailed distribution of active faults in the region (Figure 7.3). On the published active fault map by National Center of Earthquake Study (PUSGEN) (2017), the region was only characterized by the Kawa and Bobot faults in Seram. The new results provided details of geomorphic evidence and segmentations of the active faults. The Kawa fault is longer than in the previous interpretation and consists of four geometrical segments. The Bobot fault is also segmented into two portions. Although the faulting evidence of the Seram fold-and-thrust belt was observed offshore (Pairault et al., 2003; Patria and Hall, 2017; Teas et al., 2009), some active fault trace in north Seram is plausibly associated with the belt. Several faults are identified as active in Ambon, Buru, and the adjacent islands. Previous interpretations by Watkinson and Hall (2017) indicated that the Ambon is occupied by northeast-and-northwest-oriented faults with an unknown sense of motion. The study in Ambon reveals that the Ambon fault is a normal fault striking northeast. The Ambon fault possesses a significant seismic risk because it traverses near populous areas including Ambon City.

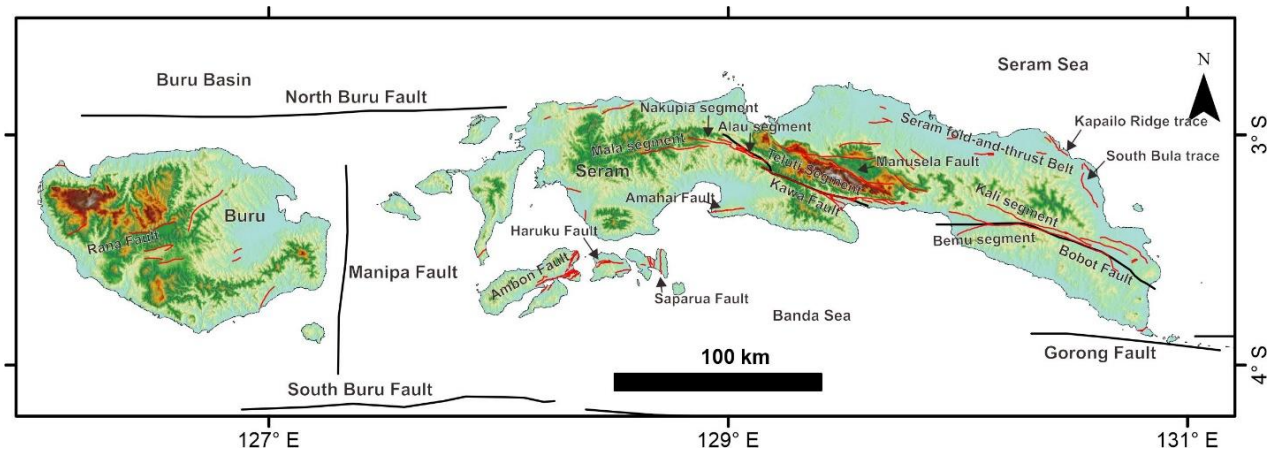

Figure 7.3. Comparison between the published active fault trace (black) by National Center of Earthquake Study (PUSGEN) (2017) and the new active fault interpretation (red) for the onshore northern Banda Arc.

7.2 Seismic hazard and tectonic implications

This study has highlighted the importance of the intra-basin fault in accommodating lateral motion of strike-slip faults. In Sulawesi, there are several valleys or basins associated with strike-slip faults, for example, the Rampi, Sapu, Lake Poso, and Lake Matano valleys in Sulawesi. The active fault traces in these depressions were commonly interpreted as basin-bounding faults

(National Center of Earthquake Study (PUSGEN), 2017; Watkinson and Hall, 2017). Learning from the 2018 Palu earthquake's surface rupture, there is a possibility that intra-basin faults traverse within the basins. Thus, the existence of intra-basin faults should be carefully examined for these basins.

Two large earthquakes have occurred along the Palu-Koro fault (Figure 7.4). The 1968 M_w 7.2 earthquake might have ruptured the northern portion of the Palu-Koro fault offshore (Prasetya et al., 2001). The 2018 M_w 7.5 earthquake ruptured the ~170-km-long central portion of the Palu-Koro fault on land and offshore (Bao et al., 2019; Jaya et al., 2019; Natawidjaja et al., 2021; Socquet et al., 2019). The remaining portion of the fault to the south has not yet ruptured at least in the last two centuries. Considering that the southern part of the Palu-Koro fault has a similar recurrence interval to the central portion, ~110 years (Daryono and Natawidjaja, 2019), the southern Palu-Koro fault may form a seismic gap and the next large earthquake is already due. This gap is ~110 km long, and it would generate an M_w 7.5 earthquake if this portion ruptures simultaneously, based on a scaling relation by Wells and Coppersmith (1994). A slip rate of about 35–40 mm/yr and an elapsed time of about 200 years would have accumulated ~7–8 m slip on this portion, similar to the maximum displacement of the 2018 Palu earthquake and the smallest offset identified on the easternmost Matano fault.

The study of the easternmost Matano fault has revealed a slip rate of ~30 mm/yr for the Matano fault (Figure 7.4). Based on the geodetic modeling, the fault's slip rate is 17–28 mm/yr (Khairi et al., 2020; Walpersdorf et al., 1998a). However, its northeastern extension, the Palu Koro fault, moves faster at ~35 or ~40 mm/yr, based on geologic or geodetic studies, respectively (Bellier et al., 2001; Socquet et al., 2006; Walpersdorf et al., 1998b). This slip-rate increase toward the Palu-Koro fault might be related to the rollback of the North Sulawesi subduction zone (Figure 7.4). The North Sulawesi trench has been progressively migrated northwards since the late Miocene, currently facilitated by the Palu-Koro fault (Hall, 2018). The slip difference between the Palu-Koro and Matano faults would yield extensional deformation in between both faults.

Beaudouin et al. (2003) noted a ~9 mm/yr opening rate in a north-south direction at the Gorontalo Bay west of the Palu-Koro fault based on geodetic measurement, and this might correspond to the slip rate difference between the Palu-Koro and Matano faults.

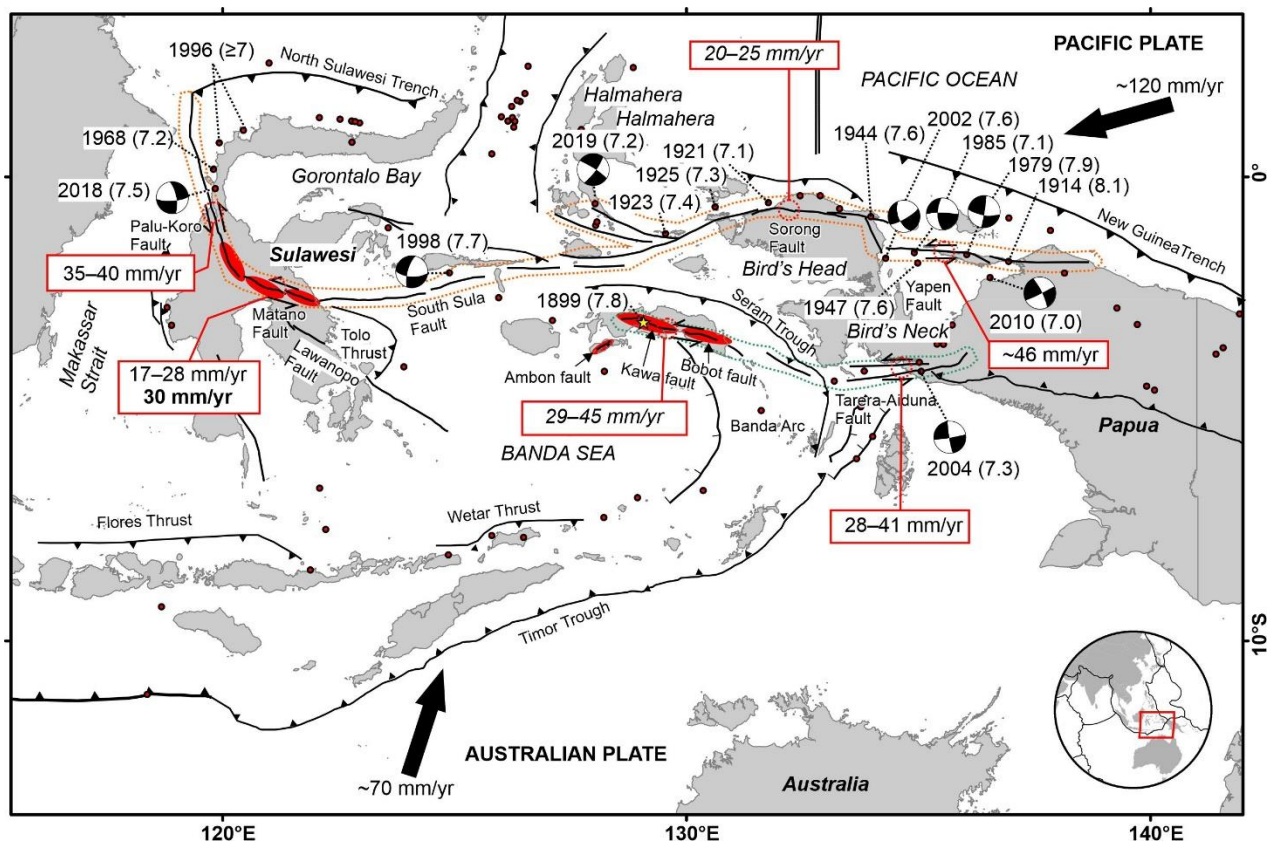

Figure 7.4 Seismotectonic map of eastern Indonesia showing the plausible seismic gaps (red highlighted) on the left-lateral strike-slip fault system. The slip rate in bold for the Matano fault is based on the calculation in this study. The slip rate in italic for the Kawa, Bobot, and Sorong faults is estimated in this study using geodetic velocity fields from Bock et al. (2003). Dots indicate $M_w \geq 7$ earthquake hypocenters with a depth ≤40 km during 1910–2022 (dots) are from the USGS earthquake catalog.

This study has indicated that the Matano fault preferably extends offshore through the Geresa segment (Figure 5.22). Extending the Geresa segment offshore suggests that the Matano fault connects to the South Sula fault. The multibeam bathymetric interpretation by Titu-Eki and Hall (2020) shows that a strike-slip fault from the northern end of the Tolo thrust is directed toward the Matano fault, although the linkage is unclear. Therefore, the Matano fault plausibly bifurcates offshore to the South Sula fault and Tolo thrust (Figure 7.4), and the left-lateral slip on the Matano

fault is transferred to both offshore structures. However, slip portioning between those structures remain unresolved.

The absence of surface faulting events on the Matano fault in the last two centuries indicates that the fault may form two seismic gaps, separated by a ~6 km wide stepover at Lake Matano (Figure 7.4). The western gap spans from the Korue Mountain to Lake Matano, while the eastern gap extends from Lake Matano to the Kolono Bay (see Figure 5.1b for locations). In this study, the recurrence interval of the eastern portion of the Matano fault has been estimated at 190–270 years. The most recent earthquake in the easternmost Matano fault was dated between the 15th and 19th centuries with an estimated M_w of ~7.4. At least 200 years have already passed since the last surface faulting event, exceeding the shortest estimated recurrence interval of 190 years. Therefore, the next surface rupturing earthquake is already due for the eastern portion of the Matano fault. The western portion of the Matano fault lacks geological information, such as the timing of the latest surface faulting event, slip rate, and recurrence interval. It has remained unruptured at least for the past 2 centuries. If its recurrence interval of surface-rupturing earthquakes is similar to the eastern portion, the western portion may be considered at the end of the interseismic period and potentially host the next large earthquake in near future. Assuming that the slip rate of the eastern portion applies to the western portion, at least 6 m slip has been accumulated and this would translate to an M_w 7.4 earthquake. Further investigation of the western portion is required to precisely evaluate its seismic behavior.

The active fault investigation of the northern Banda Arc has uncovered that the Kawa, Bobot faults, and other offshore faults accommodate 29–45 mm/yr left-lateral slip, which might be translated from the Tarera-Aiduna fault (Figure 7.4). The Kawa and Bobot faults appear separating between a contractional deformation of the Seram fold-and-thrust belt to the north and extensional faulting to the south such as the Ambon fault and the Banda detachment fault at the Weber Deep. There is a ~16 mm/yr slip difference south of Seram, and a portion of the slip might be absorbed by the Ambon fault (Figure 7.4).

In Seram, the 1899 M_w 7.8 earthquake might have been caused by the simultaneous rupture of the Kawa and Bobot fault (Watkinson and Hall, 2017). The accumulated slip on these faults since the last faulting event was estimated at 3 m, calculated using a slip rate of ~30 mm/yr. Although the recurrence interval of surface rupturing earthquakes for these faults remains unknown, the 3 m displacement is equivalent to an M_w 7.1 earthquake, based on a scaling relation by Wells and Coppersmith (1994). Even if the 1899 earthquake was not generated by these faults, the faults would have accumulated 6 m slip within 200 years. The Kawa and Bobot faults may form two seismic gaps (Figure 7.4) because the last faulting event on these faults remains unclear. Other smaller faults in the northern Banda Arc, such as the Ambon fault may have a low slip rate. The typical slip rate for a similar size fault near Ambon is about 5 mm/yr with an earthquake recurrence interval of ~115 years (Meilano et al., 2021). Although Ambon has experienced damaging earthquakes, there has been no report on the earthquake surface rupture in Ambon. This may indicate that the Ambon fault has not ruptured since the 17th century and might be considered a seismic gap (Figure 7.4).

Chapter 8

Conclusions

This research aimed to reveal faulting behaviors of several active faults along the fast-slipping left-lateral strike-slip fault system in eastern Indonesia to clarify the active tectonics and to evaluate the potential seismic hazard of the region. This dissertation has presented new essential geologic data on late Quaternary faulting activities, such as precise fault traces, slip rates, and paleoseismic history on the fault system in Palu-Koro and Matano faults, and other faults in the northern Banda arc. This dissertation has provided detailed information on the seismic hazard posed by the investigated faults and unraveled the active tectonics significance of new findings in this study. The investigation of the Palu-Koro fault in the northwest Palu Valley has clarified the nature of faulting migration of the Palu-Koro fault during the Quaternary. The comprehensive study in the Larongsangi basin has shown the segmentation and paleoseismic history of the easternmost Matano fault which aid in estimating the slip rate and recurrence interval of surface rupturing earthquakes of the fault and determining the probable magnitude and rupture extent of the most-recent surface faulting event. The research in the northern Banda Arc has disclosed the active fault distribution and the potential seismic hazard in this region and provided detailed evidence of faulting activity for the Ambon fault.

The dynamics of the Palu-Koro fault, Sulawesi are recorded in the geomorphology of the northwest Palu Valley. The topographic break between the western mountain and the Palu Valley indicates a major basin-bounding fault that controlled the deposition of old alluvial fans. Fault scarps along the eastern part of old alluvial fans represent the normal faulting activity, which initiated the deposition of young alluvial fans. The intra-basin strike-slip fault, which deforms distal portions of the young alluvial fans, is expressed by a series of north-south trending ridges. The 2018 M_w 7.5 Palu earthquake also indicates the intra-basin strike-slip faulting in the northwest Palu Valley. The development of the Palu-Koro fault in the northwest Palu Valley is characterized by the eastward progressive faulting migration from the basin-bounding fault to a more easterly

normal fault and, most recently, to the intra-basin strike-slip fault. The intra-basin fault should be carefully evaluated in a strike-slip basin as it accommodates most lateral motion.

The study on the easternmost Matano fault, Sulawesi has investigated the active fault based on remote sensing, field observation, shallow geophysical survey, and paleoseismic analysis. The eastern Matano fault deforms young geomorphic surfaces and sedimentary strata. It consists of four left-lateral strike-slip fault segments and one reverse fault segment. The Geresa and Balawai segments form a pull-apart basin at the overlapping zone. The Larongsangi and Bahomoahi segments are intra-basin faults, and the Onepute segment is related to a contractional fault bend. Analysis of fault scarp heights of the Geresa and Bahomoahi segments indicates that the fault scarps have been formed due to multiple faulting events. The Geresa segment likely extends further offshore and connects to the South Sula fault. The 7 m left-lateral offset on the beach ridge on the Geresa segment was related to the latest earthquake with an estimated magnitude M_w of 7.4 and about 107 km long rupture. The paleoseismic investigation on the Geresa segment documented five earthquakes before the 19th century. The timing of the latest surface-rupturing earthquake was dated AD 1432–1819. The average recurrence interval of surface-rupturing earthquakes was calculated at 190–270 years, and the slip rate was estimated at ~30 mm/yr. The elapsed time since the last surface faulting event is at least 200 years, exceeding the shortest average recurrence interval, therefore the future large earthquake is already due.

In the northern Banda Arc, the active structures on land were mapped using 3D anaglyph images constructed from the DEMNAS. Evidence of the Seram fold-and-thrust belt's activity is recorded in north Seram as back tilted marine terraces, fault scarps, and uplifted ridges. Central and east Seram are zones of left-lateral strike-slip faulting, evidenced by river offsets, beheaded rivers, shutter ridges, and linear valleys. Further south, Amahai, Ambon, and surrounding areas are dominated by active dip-slip faults that cut young marine terraces. Detailed work on the Ambon fault revealed that the fault records predominantly normal motion. Warped alluvial lowland surfaces and tilted terraces deposits may indicate the most recent faulting on the Ambon fault. The

smallest fault scarp is ~4 m high, plausibly representing the cumulative vertical offset from multiple earthquakes. Eleven active faults are identified on land in the northern Banda Arc, and they are capable of generating earthquakes with a magnitude M_w of 6.4 to 7.6. The Kawa fault possesses the largest seismic potential in the region, and the Ambon fault may cause a devastating event as it lies close to a populous area the Ambon City. The active faults across the northern Banda Arc accommodate the eastward movement of the northern Banda Arc relative to the stable Bird's Head. The Kawa and Bobot faults in Seram accommodate 29–45 mm/yr left-lateral slip. The convergence rate across north Seram is estimated at 15–31 mm/yr. The Ambon fault is interpreted as an antithetic structure of the Banda detachment fault, which may accommodate a portion of ~16 mm/yr extension in the Banda Sea.

References

Abers, G., McCaffrey, R., 1988. Active deformation in the New Guinea fold-and-thrust belt: Seismological evidence for strike-slip faulting and basement-involved thrusting. J. Geophys. Res. Solid Earth 93, 13332–13354. https://doi.org/https://doi.org/10.1029/JB093iB11p13332

Adhityatama, S., Triwurjani, R.R., Yurnaldi, D., Janssen, R., Khoiru Dhony, M.D., Suryatman, Abbas, A., Lukman, A., Bulbeck, D., 2022. Pulau Ampat site: A submerged 8th century iron production village in Matano Lake, South Sulawesi, Indonesia. Archaeol. Res. Asia 29, 100335. https://doi.org/https://doi.org/10.1016/j.ara.2021.100335

Baillie, P., Keep, M., Duran, P.M., Carrillo, E., Duval, G., 2019. Broadband seismic imaging around the Banda Arc: changes in the anatomy of offshore fold-and-thrust belts. Geol. Soc. London, Spec. Publ. 490. https://doi.org/10.1144/sp490-2018-141

Bao, H., Ampuero, J.-P., Meng, L., Fielding, E.J., Liang, C., Milliner, C.W.D., Feng, T., Huang, H., 2019. Early and persistent supershear rupture of the 2018 magnitude 7.5 Palu earthquake. Nat. Geosci. 12, 200–205. https://doi.org/10.1038/s41561-018-0297-z

Beaudouin, T., Bellier, O., Sebrier, M., 2003. Present-day stress and deformation field within the Sulawesi Island area (Indonesia) : geodynamic implications. Bull. la Société Géologique Fr. 174, 305–317. https://doi.org/10.2113/174.3.305

Beauprêtre, S., Garambois, S., Manighetti, I., Malavieille, J., Sénéchal, G., Chatton, M., Davies, T., Larroque, C., Rousset, D., Cotte, N., Romano, C., 2012. Finding the buried record of past earthquakes with GPR-based paleoseismology: a case study on the Hope fault, New Zealand. Geophys. J. Int. 189, 73–100. https://doi.org/10.1111/j.1365-246X.2012.05366.x

Bellier, O., Beaudouin, T., Sébrier, M., Villeneuve, M., Bahar, I., Putranto, E., Pratomo, I., Massault, M., Seward, D., 1998. Active Faulting in Central Sulawesi (Eastern Indonesia), in: Wilson, P., Michel, G.W. (Eds.), The Geodynamics of S and SE Asia (GEODYSSEA) Project Final Report. Postdam.

Bellier, O., Bourles, D.L., Beaudouin, T., Braucher, R., 1999. Cosmic Ray Exposure (CRE) dating in a wet tropical domain: Late Quaternary fan emplacements in central Sulawesi (Indonesia). Terra Nov. 11, 174–180. https://doi.org/10.1046/j.1365-3121.1999.00242.x

Bellier, O., Sébrier, M., Seward, D., Beaudouin, T., Villeneuve, M., Putranto, E., 2006. Fission track and fault kinematics analyses for new insight into the Late Cenozoic tectonic regime changes in West-Central Sulawesi (Indonesia). Tectonophysics 413, 201–220. https://doi.org/10.1016/j.tecto.2005.10.036

Bellier, O., Siame, L., Beaudouin, T., Villeneuve, M., Braucher, R., 2001. High slip rate for a low seismicity along the Palu-Koro active fault in Central Sulawesi (Indonesia). Terra Nov. 13, 463–470. https://doi.org/10.1046/j.1365-3121.2001.00382.x

Bock, Y., Prawirodirdjo, L., Genrich, J.F., Stevens, C.W., McCaffrey, R., Subarya, C., Puntodewo, S.S.O., Calais, E., 2003. Crustal motion in Indonesia from Global Positioning System measurements. J. Geophys. Res. 108, 2367. https://doi.org/10.1029/2001jb000324

Boekschoten, G.J., Best, M.B., Oosterbaan, A., Molenkamp, F.M., 1989. Past corals and recent reefs in Indonesia. Netherlands J. Sea Res. 23, 117–122. https://doi.org/10.1016/0077-7579(89)90006-9

Bronk Ramsey, C., 2009. Bayesian Analysis of Radiocarbon Dates. Radiocarbon 51, 337–360. https://doi.org/DOI: 10.1017/S0033822200033865

Brune, S., Babeyko, A.Y., Ladage, S., Sobolev, S. V., 2010. Landslide tsunami hazard in the Indonesian Sunda Arc. Nat. Hazards Earth Syst. Sci. https://doi.org/10.5194/nhess-10-589-2010

Burbank, D.W., Anderson, R.S., 2012. Tectonic Geomorphology, 2nd ed. Blackwell Science, Victoria.

Castilla, R.A., Audemard, F.A., 2007. Sand blows as a potential tool for magnitude estimation of pre-instrumental earthquakes. J. Seismol. 11, 473–487. https://doi.org/10.1007/s10950-007-9065-z

Charlton, T.R., 2000. Tertiary evolution of the Eastern Indonesia collision complex. J. Asian Earth Sci. 18, 603–631. https://doi.org/10.1016/S1367-9120(99)00049-8

Cipta, A., Robiana, R., Griffin, J.D., Horspool, N., Hidayati, S., Cummins, P.R., 2017. A probabilistic seismic hazard assessment for Sulawesi, Indonesia, in: Cummins, P.R., Meilano, I. (Eds.), Geohazards in Indonesia: Earth Science for Disaster Risk Reduction. Geological Society of London, London, pp. 133–152. https://doi.org/10.1144/SP441.6

Crosetto, S., Watkinson, I.M., Min, S., Gori, S., Falcucci, E., Ngal, N.L., 2018. Evidence of Quaternary and recent activity along the Kyaukkyan Fault , Myanmar. J. Asian Earth Sci. 156, 207–225. https://doi.org/10.1016/j.jseaes.2018.01.013

Cummins, P.R., Pranantyo, I.R., Pownall, J.M., Griffin, J.D., Meilano, I., Zhao, S., 2020. Earthquakes and tsunamis caused by low-angle normal faulting in the Banda Sea, Indonesia. Nat. Geosci. 13, 312–318. https://doi.org/10.1038/s41561-020-0545-x

Daryono, M., Natawidjaja, D.H., 2019. Surface rupture of the 1909 event (M7) on Palukoro Fault in tropical forest of Central Sulawesi , Indonesia, in: Joint Convention Yogyakarta 2019, HAGI-IAGI-IAFMI-IATMI.

Daryono, M.R., 2016. Paleoseismology of Tropical Indonesia (Cases study in Sumatran Fault, Palukoro-Matano Fault, and Lembang Fault) (Paleoseismologi Tropis Indonesia (Dengan Studi Kasus di Sesar Sumatra, Sesar Palukoro-Matano, dan Sesar Lembang)). Dessertation Doctoral Program. Institut Teknologi Bandung. Unpublished. (in Indonesian with English abstract).

Daryono, M.R., Natawidjaja, D.H., Sapiie, B., Cummins, P., 2019. Earthquake Geology of the Lembang Fault, West Java, Indonesia. Tectonophysics 751, 180–191. https://doi.org/10.1016/j.tecto.2018.12.014

Davis, J.L., Annan, A.P., 1989. Ground-penetrating radar for high-resolution mapping of soil and rock stratigraphy. Geophys. Prospect. 37, 531–551. https://doi.org/10.1111/j.1365-2478.1989.tb02221.x

DeMets, C., Gordon, R.G., Argus, D.F., 2010. Geologically current plate motions. Geophys. J. Int. 181, 1–80. https://doi.org/10.1111/j.1365-246X.2009.04491.x

Deng, Q., Wu, D., Zhang, P., Chen, S., 1986. Structure and deformational character of strike-slip fault zones. pure Appl. Geophys. 124, 203–223. https://doi.org/10.1007/BF00875726

DesRoches, R., Comerio, M., Eberhard, M., Mooney, W., Rix, G.J., 2011. Overview of the 2010 Haiti Earthquake. Earthq. Spectra 27, 1–21. https://doi.org/10.1193/1.3630129

Dikbaş, A., Akyüz, H.S., Meghraoui, M., Ferry, M., Altunel, E., Zabcı, C., Langridge, R., Yalçıner, C.Ç., 2018. Paleoseismic history and slip rate along the Sapanca-Akyazı segment of the 1999 İzmit earthquake rupture (Mw = 7.4) of the North Anatolian Fault (Turkey). Tectonophysics 738–739, 92–111. https://doi.org/https://doi.org/10.1016/j.tecto.2018.04.019

Dujardin, J.-R., Bano, M., Schlupp, A., Ferry, M., Munkhuu, U., Tsend-Ayush, N., Enkhee, B., 2014. GPR measurements to assess the Emeelt active fault's characteristics in a highly smooth topographic context, Mongolia. Geophys. J. Int. 198, 174–186. https://doi.org/10.1093/gji/ggu130

Fazzito, S.Y., Cortés, J.M., Rapalini, A.E., Terrizzano, C.M., 2013. The geometry of the active strike-slip El Tigre Fault, Precordillera of San Juan, Central-Western Argentina: Integrating resistivity surveys with structural and geomorphological data. Int. J. Earth Sci. 102, 1447–1466. https://doi.org/10.1007/s00531-013-0873-9

Gafoer, S., Suwitodirdjo, K., Suharsono, 1993. Geological map of the Bula and Watubela sheet, Maluku. Geological Research and Development Centre, Bandung.

Goto, H., Arai, K., Sato, T., 2018. Topographic Anaglyphs from Detailed Digital Elevation Models Covering Inland and Seafloor for the Tectonic Geomorphology Studies in and around Yoron Island, Ryukyu Arc, Japan. Geosci. . https://doi.org/10.3390/geosciences8100363

Griffin, J.D., Stirling, M.W., Barrell, D.J.A., van den Berg, E.J., Todd, E.K., Nicolls, R., Wang,

N., 2021. Paleoseismology of the Hyde Fault, Otago, New Zealand. New Zeal. J. Geol. Geophys. 1–25. https://doi.org/10.1080/00288306.2021.1995007

Hall, R., 2018. The subduction initiation stage of the Wilson cycle, in: Wilson, R.W., Houseman, G.A., McCaffrey, K.J.W., Dore, A.G., Buiter, S.J.H. (Eds.), Fifty Years of the Wilson Cycle Concept in Plate Tectonics. Geological Society, London,. https://doi.org/10.1144/SP470.3

Hall, R., 2012. Late Jurassic-Cenozoic reconstructions of the Indonesian region and the Indian Ocean. Tectonophysics 570–571, 1–41. https://doi.org/10.1016/j.tecto.2012.04.021

Hall, R., Ali, J.R., Anderson, C.D., Baker, S.J., 1995. Origin and motion history of the Philippine Sea Plate. Tectonophysics 251, 229–250. https://doi.org/https://doi.org/10.1016/0040-1951(95)00038-0

Hall, R., Patria, A., Adhitama, R., Pownall, J.M., White, L.T., 2017. Seram, the Seram trough, the Aru trough, the Tanimbar trough and the Weber Deep: a new look at major structures in the eastern Banda Arc, in: Indonesian Petroleum Association, Forty-First Annual Convention & Exhibition, Jakarta, 2017. pp. IPA17-91-G.

Hall, R., Wilson, M.E.J., 2000. Neogene sutures in eastern Indonesia. J. Asian Earth Sci. 18, 781–808. https://doi.org/10.1016/S1367-9120(00)00040-7

Hamilton, W., 1979. Tectonics of the Indonesian Region., USGS Professional Paper.

Hinschberger, F., Malod, J.A., Réhault, J.P., Villeneuve, M., Royer, J.Y., Burhanuddin, S., 2005. Late Cenozoic geodynamic evolution of eastern Indonesia. Tectonophysics 404, 91–118. https://doi.org/10.1016/j.tecto.2005.05.005

Hogg, A.G., Heaton, T.J., Hua, Q., Palmer, J.G., Turney, C.S.M., Southon, J., Bayliss, A., Blackwell, P.G., Boswijk, G., Bronk Ramsey, C., Pearson, C., Petchey, F., Reimer, P., Reimer, R., Wacker, L., 2020. SHCal20 Southern Hemisphere Calibration, 0–55,000 Years cal BP. Radiocarbon 62, 759–778. https://doi.org/DOI: 10.1017/RDC.2020.59

Hutchings, S.J., Mooney, W.D., 2021. The Seismicity of Indonesia and Tectonic Implications. Geochemistry, Geophys. Geosystems 22, e2021GC009812.

https://doi.org/https://doi.org/10.1029/2021GC009812

Iqbal, I., Bin, X., Tian, G., Wang, H., Sanxi, P., Yang, Y., Masood, Z., Hanwu, S., 2021. Near surface velocity estimation using gpr data: Investigations by numerical simulation, and experimental approach with avo response. Remote Sens. 13. https://doi.org/10.3390/rs13142814

Jaya, A., Nishikawa, O., Jumadil, S., 2019. Distribution and morphology of the surface ruptures of the 2018 Donggala–Palu earthquake, Central Sulawesi, Indonesia. Earth, Planets Sp. 71, 144. https://doi.org/10.1186/s40623-019-1126-3

Jol, H., 2008. Ground Penetrating Radar: Theory and Applications, 1st ed. Elsevier BV.

Katili, J.A., 1991. Tectonic evolution of eastern Indonesia and its bearing on the occurrence of hydrocarbons. Mar. Pet. Geol. 8, 70–83. https://doi.org/10.1016/0264-8172(91)90046-4

Katili, J.A., 1989. Review of past and present geotectonic concepts of eastern indonesia. Netherlands J. Sea Res. 24, 103–129. https://doi.org/10.1016/0077-7579(89)90143-9

Katili, J.A., 1970. Large transcurrent faults in Southeast Asia with special reference to Indonesia. Geol. Rundschau 59, 581–600. https://doi.org/10.1007/BF01823809

Khairi, A., Awaluddin, M., Sudarsono, B., 2020. Analysis of Seismic Deformation on the Matano fault using GNSS and SAR interferometric (Analisis Deformasi Seismik Sesar Matano Menggunakan GNSS dan Interferometrik SAR). J. Geod. Undip 9, 32-42. (in Indonesian with English abstract).

Kopp, H., Flueh, E.R., Klaeschen, D., Bialas, J., Reichert, C., 2001. Crustal structure of the Central Sunda margin at the onset of oblique subduction. Geophys. J. Int. 147, 449–474. https://doi.org/10.1046/j.0956-540X.2001.01547.x

Lienkaemper, J.J., Ramsey, C.B., 2009. OxCal: Versatile Tool for Developing Paleoearthquake Chronologies—A Primer. Seismol. Res. Lett. 80, 431–434. https://doi.org/10.1785/gssrl.80.3.431

Linick, T.W., Damon, P.E., Donahue, D.J., Jull, A.J.T., 1989. Accelerator mass spectrometry:

The new revolution in radiocarbon dating. Quat. Int. 1, 1–6. https://doi.org/https://doi.org/10.1016/1040-6182(89)90004-9

Loke, M.H., Dahlin, T., 2002. A comparison of the Gauss-Newton and quasi-Newton methods in resistivity imaging inversion. J. Appl. Geophys. 49, 149–162. https://doi.org/10.1016/S0926-9851(01)00106-9

Malod, J.A., Karta, K., Beslier, M.O., Zen, M.T., 1995. From normal to oblique subduction: Tectonic relationships between Java and Sumatra. J. Southeast Asian Earth Sci. 12, 85–93. https://doi.org/10.1016/0743-9547(95)00023-2

Mann, P., Taylor, F.W., Edwards, R.L., Ku, T.-L., 1995. Actively evolving microplate formation by oblique collision and sideways motion along strike-slip faults: An example from the northeastern Caribbean plate margin. Tectonophysics 246, 1–69. https://doi.org/https://doi.org/10.1016/0040-1951(94)00268-E

Marliyani, G.I., Arrowsmith, J.R., Whipple, K.X., 2016. Characterization of slow slip rate faults in humid areas: Cimandiri fault zone, Indonesia. J. Geophys. Res. Earth Surf. 121, 2287–2308. https://doi.org/https://doi.org/10.1002/2016JF003846

McCaffrey, R., 2009. The Tectonic Framework of the Sumatran Subduction Zone. Annu. Rev. Earth Planet. Sci. 37, 345–366. https://doi.org/10.1146/annurev.earth.031208.100212

McCaffrey, R., 1988. Active tectonics of the eastern Sunda and Banda arcs. J. Geophys. Res. 93, 15163–15182. https://doi.org/10.1029/jb093ib12p15163

McCalpin, J., 2009. Paleoseismology, 2nd ed. Academic Press, London.

McClymont, A.F., Green, A.G., Kaiser, A., Horstmeyer, H., Langridge, R., 2010. Shallow fault segmentation of the Alpine fault zone, New Zealand revealed from 2- and 3-D GPR surveying. J. Appl. Geophys. 70, 343–354. https://doi.org/10.1016/j.jappgeo.2009.08.003

Meilano, I., Salman, R., Rahmadani, S., Shi, Q., Susilo, S., Lindsey, E., Supendi, P., Daryono, D., 2021. Source Characteristics of the 2019 Mw 6.5 Ambon, Eastern Indonesia, Earthquake Inferred from Seismic and Geodetic Data. Seismol. Res. Lett. 92, 3339–3348.

https://doi.org/10.1785/0220210021

Natawidjaja, D.H., Daryono, M.R., 2015. The Lawanopo Fault, central Sulawesi, East Indonesia. AIP Conf. Proc. 1658, 30001. https://doi.org/10.1063/1.4915009

Natawidjaja, D.H., Daryono, M.R., Prasetya, G., Liu, P.L.-F., Hananto, N.D., Kongko, W., Triyoso, W., Puji, A.R., Meilano, I., Gunawan, E., Supendi, P., Pamumpuni, A., Irsyam, M., Faizal, L., Hidayati, S., Sapiie, B., Kusuma, M.A., Tawil, S., 2021. The 2018 Mw7.5 Palu 'supershear' earthquake ruptures geological fault's multisegment separated by large bends: results from integrating field measurements, LiDAR, swath bathymetry and seismic-reflection data. Geophys. J. Int. 224, 985–1002. https://doi.org/10.1093/gji/ggaa498

National Center of Earthquake Study (PUSGEN), 2017. Earthquake sources and hazards map of Indonesia 2017 (Peta Sumber dan Bahaya Gempa Indonesia Tahun 2017). Pusat Penelitian dan Pengembangan Perumahan dan Permukiman, Bandung. (in Indonesian).

National Geophysical Data Center (NGDC), 2022. NCEI/WDS Global Significant Earthquake Database, NOAA National Centers for Environmental Information. https://doi.org/10.7289/V5TD9V7K [last accessed 18 January 2022]

Okal, E.A., 1999. Historical Seismicity and Seismotectonic Context of the Great 1979 Yapen and 1996 Biak, Irian Jaya Earthquakes. pure Appl. Geophys. 154, 633–675. https://doi.org/10.1007/s000240050247

Pairault, A.A., Hall, R., Elders, C.F., 2003. Structural styles and tectonic evolution of the Seram Trough, Indonesia. Mar. Pet. Geol. 20, 1141–1160. https://doi.org/10.1016/j.marpetgeo.2003.10.001

Pakpahan, S., Ngadmanto, D., Masturyono, M., Rohadi, S., Rasmid, R., Widodo, H.S., Susilanto, P., 2015. Analisis Kegempaan di Zona Sesar Palu Koro, Sulawesi Tengah. J. Lingkung. dan Bencana Geol. 6, 253–264.

Patria, A., Hall, R., 2017. The origin and significance of the Seram trough, Indonesia, in: Indonesian Petroleum Association, Forty-First Annual Convention & Exhibition, Jakarta,

2017. pp. IPA17-19-G.

Patria, A., Putra, P.S., 2020. Development of the Palu–Koro Fault in NW Palu Valley, Indonesia. Geosci. Lett. 7, 1. https://doi.org/10.1186/s40562-020-0150-2

Perez, J.S., Tsutsumi, H., 2017. Tectonic geomorphology and paleoseismology of the Surigao segment of the Philippine fault in northeastern Mindanao Island, Philippines. Tectonophysics 699, 244–257. https://doi.org/https://doi.org/10.1016/j.tecto.2017.02.001

Peri, V.G., Rapalini, A.E., Pérez, P., Franceschinis, P., Leiva, M.F., Fazzito, S.Y., Cortés, J.M., 2020. Subsurface characterization of quaternary scarps and their possible connection to main structures of the western margin of Precordillera, San Juan, Argentina. Tectonophysics 790, 228542. https://doi.org/10.1016/j.tecto.2020.228542

Pownall, J.M., Forster, M.A., Hall, R., Watkinson, I.M., 2017. Tectonometamorphic evolution of Seram and Ambon, eastern Indonesia: Insights from 40 Ar/ 39 Ar geochronology. Gondwana Res. 44, 35–53. https://doi.org/10.1016/j.gr.2016.10.018

Pownall, J.M., Hall, R., Lister, G.S., 2016. Rolling open Earth's deepest forearc basin. Geology 44, 947–950. https://doi.org/10.1130/G38051.1

Prasetya, G.S., De Lange, W.P., Healy, T.R., 2001. The Makassar Strait Tsunamigenic Region, Indonesia. Nat. Hazards 24, 295–307. https://doi.org/10.1023/A:1012297413280

Puntodewo, S.S.O., McCaffrey, R., Calais, E., Bock, Y., Rais, J., Subarya, C., Poewariardi, R., Stevens, C., Genrich, J., Fauzi, Zwick, P., Wdowinski, S., 1994. GPS measurements of crustal deformation within the Pacific-Australia plate boundary zone in Irian Jaya, Indonesia. Tectonophysics 237, 141–153. https://doi.org/10.1016/0040-1951(94)90251-8

Putra, P.S., Aswan, A., Maryunani, K.A., Yulianto, E., Kongko, W., 2019. Field Survey of the 2018 Sulawesi Tsunami Deposits. Pure Appl. Geophys. https://doi.org/10.1007/s00024-019-02181-9

Rangin, C., Le Pichon, X., Mazzotti, S., Pubellier, M., Chamot-Rooke, N., Aurelio, M., Walpersdorf, A., Quebral, R., 1999. Plate convergence measured by GPS across the

Sundaland/Philippine Sea Plate deformed boundary: the Philippines and eastern Indonesia. Geophys. J. Int. 139, 296–316. https://doi.org/10.1046/j.1365-246x.1999.00969.x

Reimer, P.J., Austin, W.E.N., Bard, E., Bayliss, A., Blackwell, P.G., Bronk Ramsey, C., Butzin, M., Cheng, H., Edwards, R.L., Friedrich, M., Grootes, P.M., Guilderson, T.P., Hajdas, I., Heaton, T.J., Hogg, A.G., Hughen, K.A., Kromer, B., Manning, S.W., Muscheler, R., Palmer, J.G., Pearson, C., van der Plicht, J., Reimer, R.W., Richards, D.A., Scott, E.M., Southon, J.R., Turney, C.S.M., Wacker, L., Adolphi, F., Büntgen, U., Capano, M., Fahrni, S.M., Fogtmann-Schulz, A., Friedrich, R., Köhler, P., Kudsk, S., Miyake, F., Olsen, J., Reinig, F., Sakamoto, M., Sookdeo, A., Talamo, S., 2020. The IntCal20 Northern Hemisphere Radiocarbon Age Calibration Curve (0–55 cal kBP). Radiocarbon 62, 725–757. https://doi.org/DOI: 10.1017/RDC.2020.41

Sahara, D.P., Nugraha, A.D., Muhari, A., Rusdin, A.A., Rosalia, S., Priyono, A., Zulfakriza, Z., Widiyantoro, S., Puspito, N.T., Rietbrock, A., Lesmana, A., Kusumawati, D., Ardianto, A., Baskara, A.W., Halauwet, Y., Shiddiqi, H.A., Rafie, M.T., Pradisti, R., Mozef, P.W., Tuakia, M.Z., Elly, E., 2021. Source mechanism and triggered large aftershocks of the Mw 6.5 Ambon, Indonesia earthquake. Tectonophysics. https://doi.org/10.1016/j.tecto.2020.228709

Sassa, S., Takagawa, T., 2019. Liquefied gravity flow-induced tsunami: first evidence and comparison from the 2018 Indonesia Sulawesi earthquake and tsunami disasters. Landslides 16, 195–200. https://doi.org/10.1007/s10346-018-1114-x

Schlüter, H.U., Gaedicke, C., Roeser, H.A., Schreckenberger, B., Meyer, H., Reichert, C., Djajadihardja, Y., Prexl, A., 2002. Tectonic features of the southern Sumatra-western Java forearc of Indonesia. Tectonics 21, 11–15. https://doi.org/10.1029/2001TC901048

Scholz, C.H., 2019. The Mechanics of Earthquakes and Faulting, 3rd ed. Cambridge University Press, Cambridge. https://doi.org/DOI: 10.1017/9781316681473

Shnizai, Z., 2020. Mapping of active and presumed active faults in Afghanistan by interpretation

of 1-arcsecond SRTM anaglyph images. J. Seismol. 24, 1131–1157. https://doi.org/10.1007/s10950-020-09933-4

Shulgin, A., Kopp, H., Mueller, C., Planert, L., Lueschen, E., Flueh, E.R., Djajadihardja, Y., 2011. Structural architecture of oceanic plateau subduction offshore Eastern Java and the potential implications for geohazards. Geophys. J. Int. 184, 12–28. https://doi.org/10.1111/j.1365-246X.2010.04834.x

Sieh, K., Natawidjaja, D., 2000. Neotectonics of the Sumatran fault, Indonesia. J. Geophys. Res. 105, 28295–28326. https://doi.org/10.1029/2000JB900120

Silver, E.A., McCaffrey, R., Smith, R.B., 1983. Collision, rotation, and the initiation of subduction in the evolution of Sulawesi, Indonesia. J. Geophys. Res. 88, 9407–9418.

Simandjuntak, T.O., Rusmana, E., Supandjono, J.B., Koswara, A., 1993. Geological map of Bungku quadrangle, Sulawesi. Geological Research and Development Centre, Bandung.

Smith, D.G., Jol, H.M., 1995. Ground penetrating radar: antenna frequencies and maximum probable depths of penetration in Quaternary sediments. J. Appl. Geophys. 33, 93–100. https://doi.org/10.1016/0926-9851(95)90032-2

Socquet, A., Hollingsworth, J., Pathier, E., Bouchon, M., 2019. Evidence of supershear during the 2018 magnitude 7.5 Palu earthquake from space geodesy. Nat. Geosci. 12, 192–199. https://doi.org/10.1038/s41561-018-0296-0

Socquet, A., Simons, W., Vigny, C., McCaffrey, R., Subarya, C., Sarsito, D., Ambrosius, B., Spakman, W., 2006. Microblock rotations and fault coupling in SE Asia triple junction (Sulawesi, Indonesia) from GPS and earthquake slip vector data. J. Geophys. Res. 111, B08409. https://doi.org/10.1029/2005JB003963

Spakman, W., Hall, R., 2010. Surface deformation and slab-mantle interaction during Banda arc subduction rollback. Nat. Geosci. https://doi.org/10.1038/ngeo917

Stevens, C., McCaffrey, R., Bock, Y., Genrich, J., Endang, Subarya, C., Puntodewo, S.S.O., Fauzi, Vigny, C., 1999. Rapid rotations about a vertical axis in a collisional setting revealed

by the Palu fault, Sulawesi, Indonesia. Geophys. Res. Lett. 26, 2677–2680. https://doi.org/10.1029/1999GL008344

Stevens, C.W., McCaffrey, R., Bock, Y., Genrich, J.F., Pubellier, M., Subarya, C., 2002. Evidence for block rotations and basal shear in the world's fastest slipping continental shear zone in NW New Guinea, in: S. Stein; J. T. Freymeuller (Ed.), Plate Boundary Zones. American Geophysical Union, pp. 87–99. https://doi.org/10.1029/GD030p0087

Storz, H., Storz, W., Jacobs, F., 2000. Electrical resistivity tomography to investigate geological structures of the earth's upper crust. Geophys. Prospect. 48, 455–471. https://doi.org/10.1046/j.1365-2478.2000.00196.x

Sukamto, R.A.B., Sumadirdja, H., Suptandar, T., Hardjoprawiro, S., Sudana, D., 1973. Reconnaissance Geological Map of the Palu Quadrangle, Sulawesi. Geological Research and Development Centre, Bandung.

Suzuki, K., Toda, S., Kusunoki, K., Fujimitsu, Y., Mogi, T., Jomori, A., 2000. Case studies of electrical and electromagnetic methods applied to mapping active faults beneath the thick quaternary. Dev. Geotech. Eng. 84, 29–45. https://doi.org/10.1016/S0165-1250(00)80005-X

Takagi, H., Pratama, M.B., Kurobe, S., Esteban, M., Aránguiz, R., Ke, B., 2019. Analysis of generation and arrival time of landslide tsunami to Palu City due to the 2018 Sulawesi earthquake. Landslides 16, 983–991. https://doi.org/10.1007/s10346-019-01166-y

Teas, P.A., Decker, J., Orange, D., Baillie, P., 2009. New Insight Into Structure and Tectonics of the Seram Trough From SeaSeep^{TM} High Resolution Bathymetry, in: Indonesian Petroleum Association, Thirty-Third Annual Convention & Exhibition, Jakarta.

Telford, William Murray, Telford, W M, Geldart, L.P., Sheriff, R.E., 1990. Applied geophysics. Cambridge university press.

Titu-Eki, A., Hall, R., 2020. The Significance of the Banda Sea: Tectonic Deformation Review in Eastern Sulawesi. Indones. J. Geosci. 7, 291–303. https://doi.org/10.17014/ijog.7.3.291-303

Tjia, H.D., 1978. Active Faults in Indonesia. Bull. Geol. Soc. Malaysia 10, 73–92.

Tjokrosapoetro, S., Achdan, A., Suwitodirdjo, K., Rusmana, E., Abidin, H.Z., 1993a. Geological map of the Masohi Quadrangle, Maluku. Geological Research and Development Centre, Bandung.

Tjokrosapoetro, S., Budhitrisna, T., Rusmana, E., 1993b. Geological map of the Buru quadrangle, Maluku. Geological Research and Development Centre, Bandung.

Tjokrosapoetro, S., Rusmana, E., Achdan, A., 1993c. Geological map of the Ambon sheet, Maluku. Geological Research and Development Centre, Bandung.

Toda, S., 2011. Paleoseismology BT - Encyclopedia of Solid Earth Geophysics, in: Gupta, H.K. (Ed.), . Springer Netherlands, Dordrecht, pp. 964–977. https://doi.org/10.1007/978-90-481-8702-7_9

Toda, S., Kaneda, H., Okada, S., Ishimura, D., Mildon, Z.K., 2016. Slip-partitioned surface ruptures for the Mw 7.0 16 April 2016 Kumamoto, Japan, earthquake. Earth, Planets Sp. 68, 188. https://doi.org/10.1186/s40623-016-0560-8

Tsutsumi, H., Perez, J.S., 2013. Large-scale active fault map of the Philippine fault based on aerial photograph interpretation. Act. Fault Res. 2013, 29–37. https://doi.org/10.11462/afr.2013.39_29

Tsutsumi, H., Sato, T., 2009. Tectonic geomorphology of the southernmost Sagaing fault and surface rupture associated with the may 1930 Pegu (Bago) earthquake, Myanmar. Bull. Seismol. Soc. Am. 99, 2155–2168. https://doi.org/10.1785/0120080113

Vigny, C., Perfettini, H., Walpersdorf, A., Lemoine, A., Simons, W., van Loon, D., Ambrosius, B., Stevens, C., McCaffrey, R., Morgan, P., Bock, Y., Subarya, C., Manurung, P., Kahar, J., Abidin, H.Z., Abu, S.H., 2002. Migration of seismicity and earthquake interactions monitored by GPS in SE Asia triple junction: Sulawesi, Indonesia. J. Geophys. Res. 107, ETG 7-1–ETG 7-11. https://doi.org/10.1029/2001jb000377

Villeneuve, M., Gunawan, W., Cornee, J.-J., Vidal, O., 2002. Geology of the central Sulawesi

belt (eastern Indonesia): constraints for geodynamic models. Int. J. Earth Sci. 91, 524–537. https://doi.org/10.1007/s005310100228

Walpersdorf, A., Vigny, C., Manurung, P., Subarya, C., Sutisna, S., 1998a. Determining the Sula block kinematics in the triple junction area in Indonesia by GPS. Geophys. J. Int. 135, 351–361. https://doi.org/10.1046/j.1365-246X.1998.00641.x

Walpersdorf, A., Vigny, C., Subarya, C., Manurung, P., 1998b. Monitoring of the Palu-Koro Fault (Sulawesi) by GPS. Geophys. Res. Lett. 25, 2313–2316. https://doi.org/10.1029/98GL01799

Watkinson, I.M., Hall, R., 2017. Fault systems of the eastern Indonesian triple junction: evaluation of Quaternary activity and implications for seismic hazards, in: Cummins, P.R., Meilano, I. (Eds.), Geohazards in Indonesia: Earth Science for Disaster Risk Reduction. Geological Society of London, London, pp. 71–120. https://doi.org/10.1144/SP441.8

Wells, D.L., Coppersmith, K.J., 1994. New Empirical Relationships among Magnitude, Rupture Length, Rupture Width, Rupture Area, and Surface Displacement. Bull. Seismol. Soc. Am. 84, 974–1002. https://doi.org/10.1785/BSSA0840040974

Wesnousky, S.G., 2008. Displacement and geometrical characteristics of earthquake surface ruptures: Issues and implications for seismic-hazard analysis and the process of earthquake rupture. Bull. Seismol. Soc. Am. 98, 1609–1632. https://doi.org/10.1785/0120070111

Wesnousky, S.G., 2006. Predicting the endpoints of earthquake ruptures. Nature 444, 358–360. https://doi.org/10.1038/nature05275

Wu, J.E., McClay, K., Whitehouse, P., Dooley, T., 2009. 4D analogue modelling of transtensional pull-apart basins. Mar. Pet. Geol. 26, 1608–1623. https://doi.org/10.1016/j.marpetgeo.2008.06.007

Yang, X., Singh, S.C., Deighton, I., 2021. The Margin-Oblique Kumawa Strike-Slip Fault in the Banda Forearc, East Indonesia: Structural Deformation, Tectonic Origin and Geohazard Implication. Tectonics 40, e2020TC006567.

https://doi.org/https://doi.org/10.1029/2020TC006567

Yeats, R.S., Sieh, K., Allen, C.R., 1997. The Geology of Earthquakes. Oxford University Press, New York.

Youd, T.L., Hoose, S.N., 1977. Liquefaction susceptibility and geologic setting, in: Proc., 6th World Conf. on Earthquake Engineering. Indian Society of Earthquake Technology Roorkee, India, pp. 37–42.

Zhang, P., Burchfiel, B.C., Chen, S., Deng, Q., Zhang, P., Burchfiel, B.C., Chen, S., 1989. Extinction of pull-apart basins Extinction of pull-apart basins. Geology 17, 814–817. https://doi.org/10.1130/0091-7613(1989)017<0814

Appendix A

1. Active fault map of the Larongsangi Basin
2. Field observations in Matano fault
3. Orthophotos of the Ululere paleoseismic trench

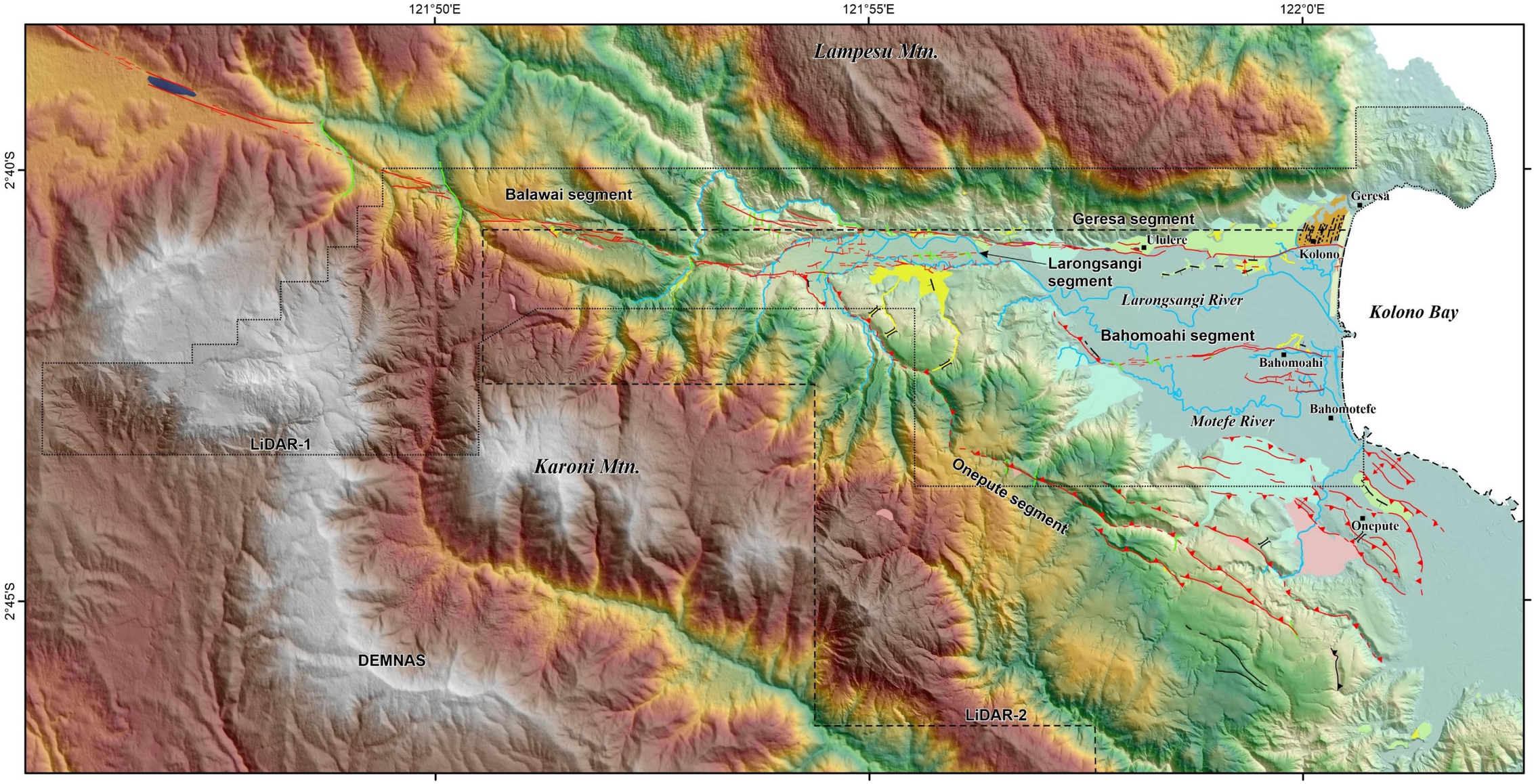

Active fault map of the Larongsangi basin
East Bungku Subdistrict, Morowali District, Central Sulawesi Province, Indonesia

Adi Patria, Danny Hilman Natawidjaja, Mudrik Rahmawan Daryono, Muhammad Hanif, Hiroyuki Tsutsumi

N

0 2 4 6 8 km

Projection: WGS 1984

Base map:
~1-3-m resolution LiDAR
~8.3-m resolution Indonesian DEM (DEMNAS)

Elevation (m)
1400
0

Legend

- Active fault
- Active fault (inferred)
- Potentially active fault
- Potentially active fault (inferred)
- Offset river
- Beach ridge axis
- Abandoned river
- Tilt
- Windgap
- Alluvial cone/fan
- Fluvial terrace 1
- Fluvial terrace 2
- Ponded alluvium
- Beach ridge
- Raised beach ridge
- Pressure ridge
- Shutter ridge
- Sag pond

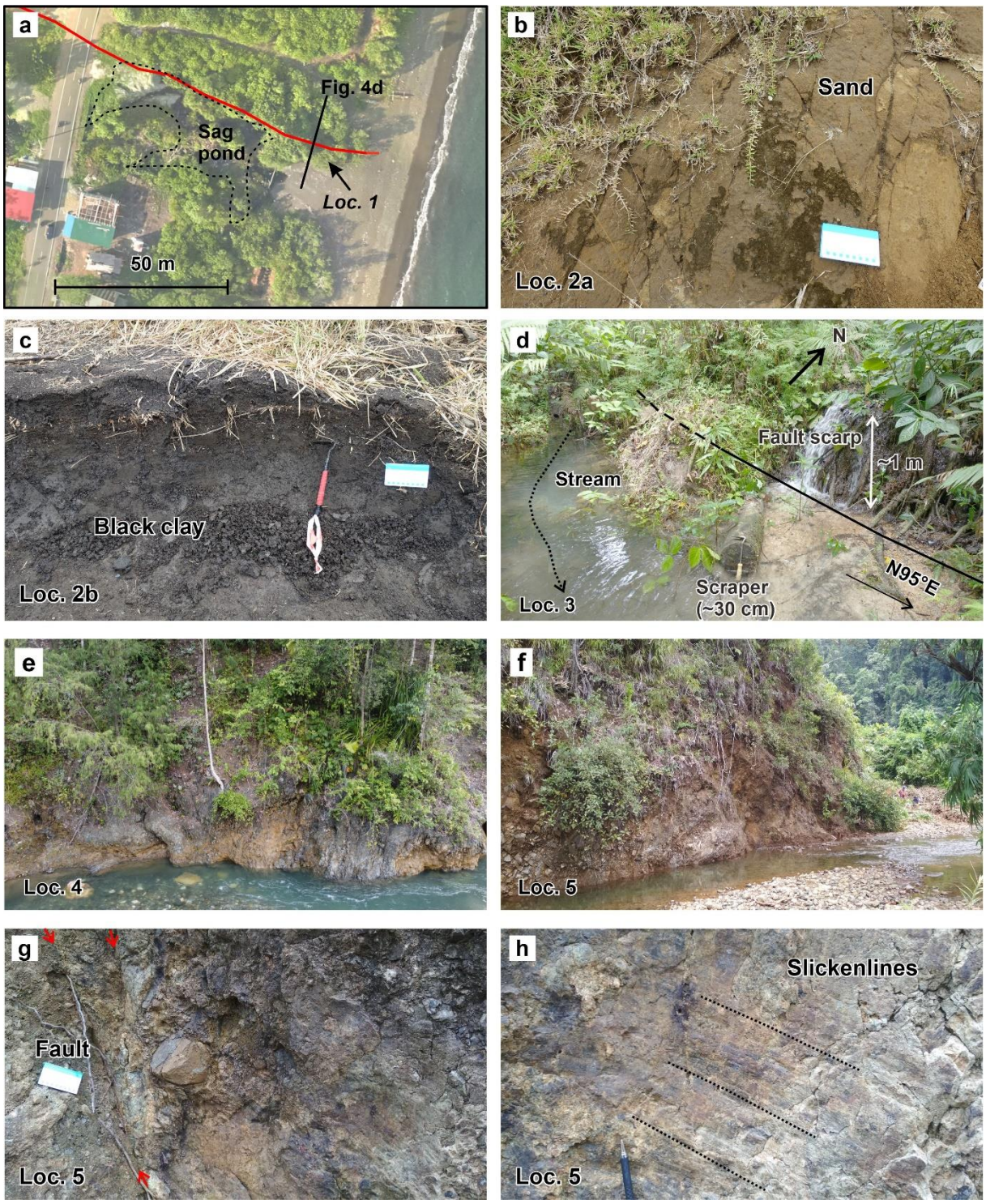

(a) Orthophoto of sag pond at Kolono Beach. (b) Exposure of sand at a ridge crest in Ululere at Loc. 2a. (c) Exposure of black clay at a ridge toe in Ululere at Loc. 2b. (d) Fault scarp at Loc. 3. (e) Outcrop of faulted serpentinite at Loc. 4. (f, g, and h) Serpentinite exposure, fault plane, and slicken lines at Loc. 5.


West wall
1 m
1 m

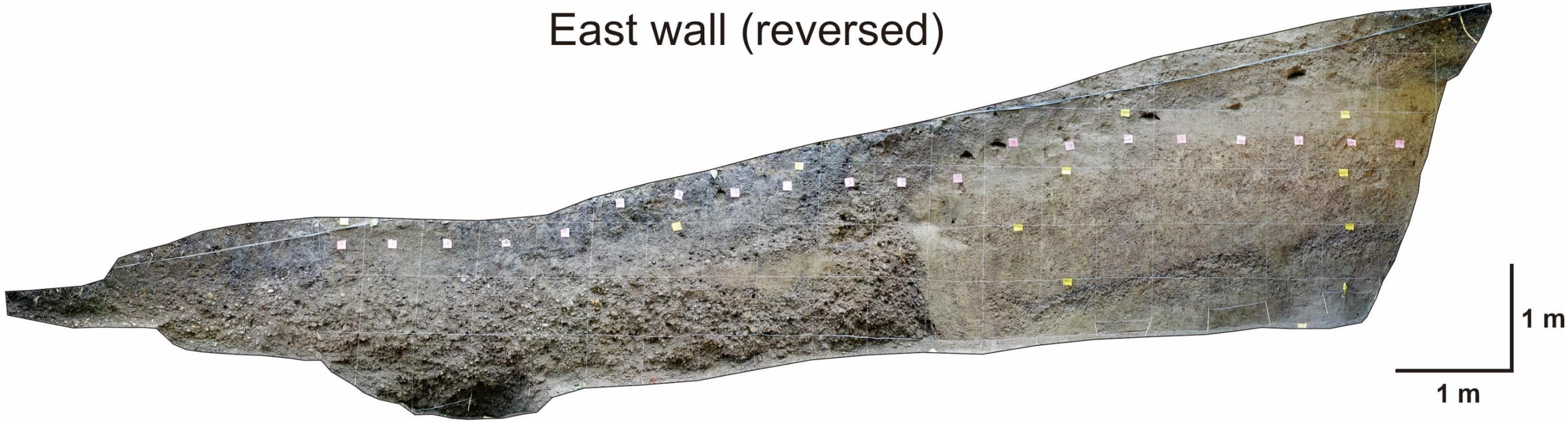
East wall (reversed)
1 m
1 m

Appendix B

Active fault map of the onshore northern Banda Arc

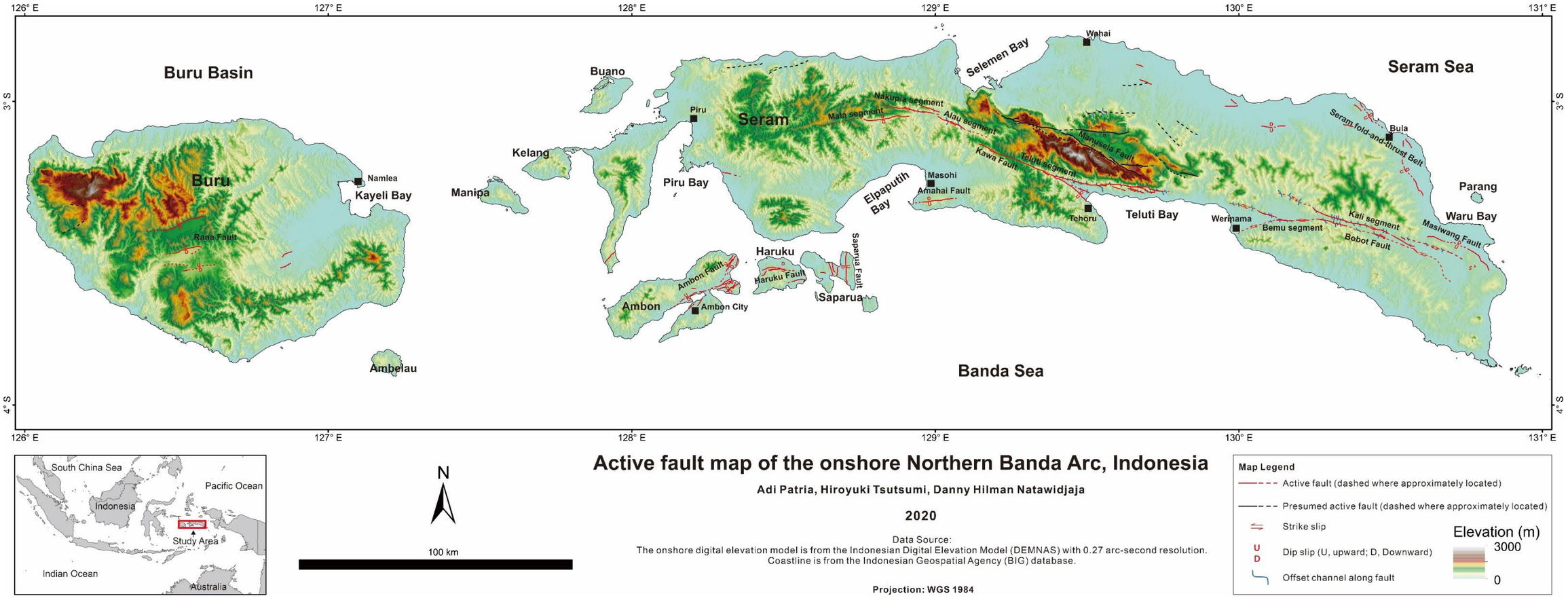
Active fault map of the onshore Northern Banda Arc, Indonesia
Adi Patria, Hiroyuki Tsutsumi, Danny Hilman Natawidjaja
2020
Data Source:
The onshore digital elevation model is from the Indonesian Digital Elevation Model (DEMNAS) with 0.27 arc-second resolution.
Coastline is from the Indonesian Geospatial Agency (BIG) database.
Projection: WGS 1984
Map Legend
Active fault (dashed where approximately located)
Presumed active fault (dashed where approximately located)
Strike slip
Dip slip (U, upward; D, Downward)
Offset channel along fault
Elevation (m)
3000
0
N
100 km
South China Sea
Pacific Ocean
Indonesia
Study Area
Indian Ocean
Australia
Buru Basin
Buru
Namlea
Kayeli Bay
Rana Fault
Ambelau
Manipa
Kelang
Buano
Piru
Piru Bay
Seram
Nakupia segment
Mala segment
Alau segment
Kawa Fault
Teluti segment
Manusela Fault
Selemen Bay
Wahai
Elpaputih Bay
Masohi
Amahai Fault
Tehoru
Teluti Bay
Haruku
Haruku Fault
Saparua Fault
Saparua
Ambon
Ambon Fault
Ambon City
Banda Sea
Seram Sea
Seram fold-and-thrust Belt
Bula
Parang
Waru Bay
Masiwang Fault
Wemama
Bemu segment
Kali segment
Bobot Fault
126° E
127° E
128° E
129° E
130° E
131° E
3° S
4° S